Kinetic Modeling of Magnetic Field Dynamics and Thermal Energy Transport in Inertial Fusion Energy Plasmas

by

Archis S. Joglekar

A dissertation submitted in partial fulfillment
of the requirements for the degree of
Doctor of Philosophy
(Nuclear Engineering and Radiological Sciences)
in the University of Michigan
2016

Doctoral Committee:

Professor Alexander G.R. Thomas, Chair
Professor R. Paul Drake
Professor James Holloway
Professor Karl Krushelnick

2016

DEDICATION

For my grandmother,
From Mahim to Michigan

ACKNOWLEDGMENTS

This work was not only enabled by, but would have been insurmountable without the help of my ever-available advisor, Alec Thomas. His patience, trust, and genius gave me confidence.

My family deserves great credit for being steady in their guidance and stable in their location. Having most of them an hour away has been something I took for granted. This not only includes my parents and sister, but also all my cousins and aunts and uncles. Thanks for being so supportive.

More than a little gratitude is due to my friends all over the world who helped me value time well spent outside of physics.

I would like to thank the Department of Nuclear Engineering and Radiological Sciences, especially Pam Derry and Peggy Gramer, for shepherding me through a decade.

I sincerely appreciate the effort put forth by my collaborators from Princeton and the UK. Without it, my work would not be as impactful. This is doubly so for Robert Kingham; Without his impetus, IMPACTA would never have been written and I would have never had access to such a powerful instrument.

This research was supported by the Department of Energy through Grant No. DE SC0010621 and in part through computational resources and services provided by Advanced Research Computing at the University of Michigan, Ann Arbor.

TABLE OF CONTENTS

LIST OF FIGURES

LIST OF APPENDICES

LIST OF ABBREVIATIONS

DLM Dum-Langdon-Matte

D-T deuterium-tritium

IB inverse Bremsstrahlung

ICF Inertial Confinement Fusion

LLE Laboratory for Laser Energetics

LLNL Lawrence Livermore National Laboratory

MHD magnetohydrodynamics

MIFEDS Magneto-Inertial Fusion Electric Discharge System

NIF National Ignition Facility

VFP Vlasov-Fokker-Planck

VFPM Vlasov-Fokker-Planck-Maxwell

ABSTRACT

In indirect-drive inertial-fusion experiments, a hohlraum converts laser energy into X-rays that heat an ablator material on a fuel capsule. The expansion of the ablator leads to implosion of the fuel capsule and fusion conditions in a hot spot, where alpha particles are produced and propagate a burn wave through the fuel. Accurate determination of the balance of energy fluxes in the hohlraum not only requires consideration of X-ray transport, but also needs careful treatment of electron transport, because laser energy is coupled primarily to the electrons in the plasma. The steep electron-thermal-energy gradients in this environment can lead to breakdown of diffusive heat-transport and introduce non-local effects. Additionally, the plasmas produced in such laser-plasma experiments are subject to the influence of self-generated magnetic fields. A kinetic formulation enables detailed calculations of thermal-energy transport and magnetic-field dynamics in these plasmas due to self-consistent inclusion of effects in electron transport that depend not only on details of the particle energy distribution but also on the electromagnetic fields in the plasma. The dissertation describes novel comparisons between Braginskii transport and kinetic modeling that quantify the importance of kinetic effects. In addition to the theoretical contributions and modeling results, the author was also responsible for the development of a ray-tracing module to model laser propagation.

Through kinetic modeling, the heat flow near the laser heating region retains non-local effects. In the case of an externally applied magnetic field, non-local contributions to the Nernst effect increase the rate of field transport by the Nernst mechanism. The Nernst effect leads to significantly faster transport of the magnetic field to the hohlraum axis in

comparison to field transport through plasma hydrodynamic motion only.

The self-generated magnetic fields are oppositely aligned with respect to each other and and are subject to reconnection. The magnetic reconnection mechanism is, in this case, governed by heat flow that transports the magnetic field. This mechanism is prevalent in plasmas where the thermal energy density is higher than the magnetic energy density. Such an environment is present in hohlraums near the critical surface, where reconnection results in redistribution of the thermal energy.

CHAPTER 1

Introduction

1.1 Thermonuclear Fusion

If fusion energy is to be realized on Earth, a likely nuclear reaction that can be exploited is

$$\mathrm{D} + \mathrm{T} \rightarrow \ ^4\mathrm{He}(3.5\ \mathrm{MeV}) + \mathrm{n}(14.1\ \mathrm{MeV}), \tag{1.1}$$

where n is a neutron and D and T are the heavier isotopes of hydrogen, deuterium ^{2}H and tritium ^{3}H, respectively. The energy in the brackets adjacent to each product is the imparted kinetic energy. The deuterium and tritium nuclei must overcome electrostatic repulsion in order for fusion to occur. Accelerating the nuclei to sufficient kinetic energies and colliding them may accomplish this, but it does not offer a viable solution for power production because of energy loss from the Coulomb force [1]. In a plasma, however, the kinetic energy does not have to be lost. In the scenario where an applied pressure is high enough to compete with the internal energy density of neutral molecules or atoms, the collection of particles behaves as an ionized medium. At higher pressures, the ionized medium becomes a plasma that roughly behaves as a system of ions and electrons that is subject to internal electromagnetic forces. In a plasma in thermal equilibrium, the ions may collide with one another but the Coulomb collisions no longer result in energy loss, rather, they redistribute

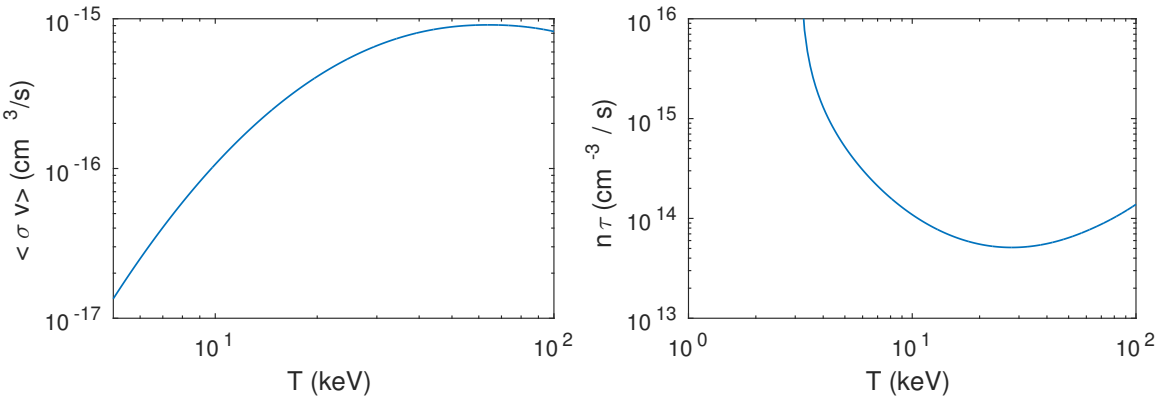

(a) (b)

Figure 1.1: (a) The reaction rate of D-T peaks at $\simeq 50$ keV. The dependency on temperature up to the peak is linear. (b) The Lawson criteria for the various reactions reaches a minimum. For D-T, $n\tau_E \geq 10^{20}$ when $k_B T \simeq 25$ keV. Reproduced with data from [1].

the kinetic energy of the plasma particles. In a sufficiently hot plasma, thermal motion may result in collisions that overcome the Coulomb barrier. In these conditions where the fusing nuclei are in thermal equilibrium as part of a plasma, *thermonuclear fusion* can take place.

For this to succeed, one requires confining a plasma of sufficient density and temperature together over an adequately long time-scale. The threshold in plasma density, temperature, and confinement time that is required to produce a net gain of energy can be found by requiring a balance between the internal energy per particle, $3k_B T$, that is confined within a specific time, τ_E, versus the energy produced from the nuclear reaction $3/20 Q_{\mathrm{DT}} \langle \sigma v \rangle$ minus the energy lost to radiation $C_b T^{1/2}$ in that same time. This threshold is called the Lawson criterion [2, 1] and given by

$$n\tau_E \equiv L \geq \frac{3k_B T}{\frac{3}{20} Q_{\mathrm{DT}} \langle \sigma v \rangle - C_b T^{1/2}}, \tag{1.2}$$

where $C_b = 5.34 \times 10^{24}$ erg cm^3 s^{-1} keV$^{-1/2}$, $Q_{\mathrm{DT}} = 2.86 \times 10^{-5}$ erg, and $k_B = 1.6022 \times 10^{-9}$ erg/keV. τ_E is the confinement time required for a plasma of density n.

The Lawson criterion, L, is a function of the temperature and is shown in Fig. 1.1b. For a deuterium-tritium (D-T) mixture, this reaches a minimum at a temperature of approxi-

mately 25 keV but more generally, the Lawson criterion requires fuel compression such that the product of the density and confinement time is above a certain threshold in order for the reaction to sustain itself on its own internal energy. Different methods of achieving this confinement have led to two mainstream fusion schemes: Inertial Confinement Fusion (ICF) and Magnetic Confinement Fusion (MCF). MCF requires the confinement of tenous plasmas by a magnetic field over time-scales on the order of seconds. Reducing this time-scale necessitates the use of high density plasmas. Based on the pioneering publication in 1972 by Nuckolls et al. [3], ICF accomplishes the minimum $n\tau_E$ by confining high density plasmas over time-scales on the order of 10s of picoseconds.

In ICF, the objective is to compress the fuel sufficiently and heat a so-called central hot-spot such that a small volume of fuel in the center of the compressed fuel capsule "ignites" and propagates a burn wave through the rest of the fuel. The mechanism for fuel compression is analogous to that which propels a rocket and is illustrated in Fig. 1.2. An ICF capsule may often be comprised of a D-T mixture in gas or liquid form. The fuel is encapsulated with a thin layer of low atomic number (low Z) material known as an *ablator*. If the ablator material were to "blowoff" much like rocket fuel, Newton's Third Law dictates that the ICF fuel pellet must feel a reaction force radially inwards to compensate for the rate of the momentum loss of the "blowoff", or ablated, material. For this purpose, the ablator is heated with a form of driving radiation that depends on the scheme. Sufficient compression of the fuel requires acceleration of the fuel to speeds of 300 km/s prior to the implosion. The ablative process also drives shocks into the fuel capsule that can create a hot-spot. The alpha particles created from the nuclear reactions in the hot-spot deposit their kinetic energy within the fuel and cause the propagation of a burn-wave through the remaining fuel during the implosion.

The two methods through which ICF are distinguished by the primary drivers of ablation; direct drive and indirect drive. In the sections that follow, the direct and indirect drive

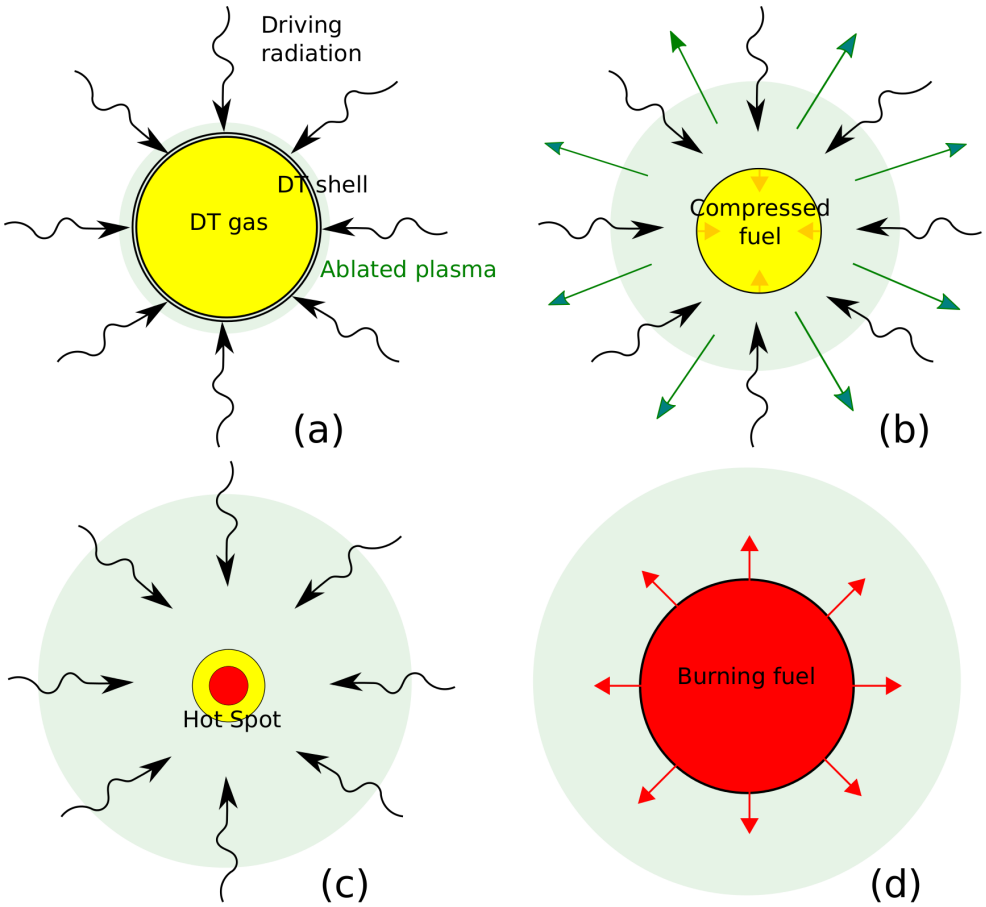

Figure 1.2: Different stages of ablative implosion of a fuel capsule. (a) The radiation heats the thin shell surrounding the fuel. (b) The expansion of the heated ablator sends shocks through the fuel capsule causing compression and heating. The expansion also accelerates the outer shell and begins the implosion. (c) The shell slows to a halt and maximum compression is reached. The fuel reaches hot-spot conditions. (d) The alpha particles generated from the fusion reactions propagate a burn-wave from the hot-spot as the fuel expands.

concepts and their shortcomings are described briefly and the motivation for this thesis in the context of these shortcomings is provided.

1.2 Direct Drive

Direct drive refers to the direct application of laser pulses to the fuel capsule to heat the ablator [4, 5, 6, 7]. Many laser beams rapidly heat the outside of a spherical fusion target.

The ablation of the laser-heated surface causes compression of the D-T fuel pellet to 1000 times solid density. The self-sustaining reaction proceeds when a central hot-spot reaches $\mathcal{O}(10)$ keV.

Direct-drive experiments are a topic of active research at the Laboratory for Laser Energetics (LLE) at the University of Rochester which houses the OMEGA laser. Experiments on OMEGA have shown the ability to reach high areal densities using pulse shaping [8]. Achieving ignition in direct-drive ICF requires central pressures larger than 100 Gigabar, which in turn requires more intense lasers than those that currently exist at LLE. However, smaller-scale experiments that are hydrodynamically equivalent to the ignition designs have been performed [9, 10].

Designing ignition-hydrodynamically-equivalent experiments requires attaining the same laser drive intensity, implosion velocity, the fuel adiabat, and the in-flight aspect ratio as the ignition design presented in refs. [8, 11]. Experiments have spanned a broad region of design space [9] and found that performance is limited at high implosion velocities due to instability growth. Hot-spot pressures of up to 40 Gbar have been demonstrated for moderate-adiabat experiments which show good agreement with modeling [10]. Low-adiabat experiments have not performed as well relative to predictions from codes because of instabilities during shell acceleration and their effects on hydrodynamic behavior during stagnation [10] and work has focused on improving implosions by the mitigation of these instabilities [12, 13, 14, 15], or better understanding of the laser absorption [16] and thermal transport [17] that is coupled to the implosion.

Direct-drive ignition-scale experiments are designed for the experimental capabilities offered by the National Ignition Facility (NIF). However, at the time of writing, NIF is primarily used for indirect-drive experiments.

1.3 Indirect Drive

1.3.1 Hohlraum

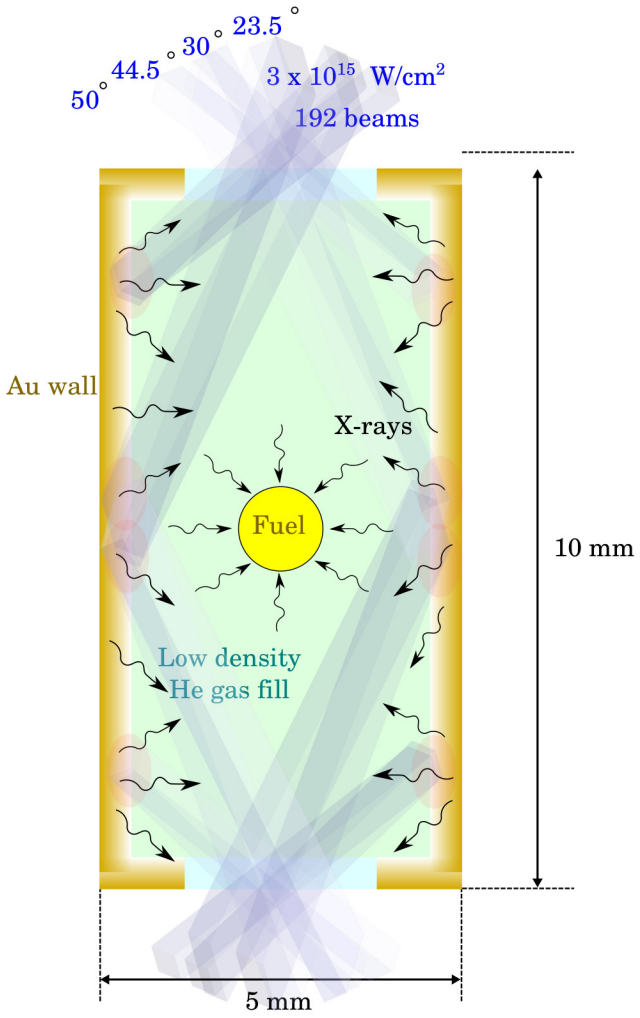

Figure 1.3: Example of an indirect-drive experiment. The laser energy is converted to X-rays by the gold plasma that heat the liner material on the fuel capsule, and thus, driving an implosion. The hohlraum is filled with a low Z gas to tamp hydrodynamic motion of the gold plasma.

In indirect drive experiments, the ablation pressure is a result of the deposition of energy from blackbody X-rays generated inside a *hohlraum*, shown in Fig. 1.3. Typically a hollow cylinder, the hohlraum is usually composed of a high atomic number (high Z) material.

The hohlraums used on the NOVA facility at Lawrence Livermore National Laboratory

(LLNL) were approximately $2-3$ mm in size [18, 19]. The NIF and the OMEGA laser at Laboratory for Laser Energetics (LLE) are the leading experimental facilities at the time of writing. NIF hohlraums are $4-6$ mm in diameter and $7-10$ mm in length [20, 21, 22] while the smaller scale hohlraums used at the OMEGA laser are $2-4$ mm in diameter and $4-6$ mm in length. Current hohlraum designs are optimized for the driving lasers of the NIF[1][2].

A NIF hohlraum is composed of a high Z material to efficiently absorb laser energy and produce a blackbody radiation spectrum of approximately 300 eV given appropriate laser parameters. The X-rays generated by the hohlraum heat the ablation material on the fuel capsule more uniformly than the heating from the finite number of laser spots in direct drive, theoretically improving the symmetry of the drive that compresses and heats the fuel to the desired conditions [23].

1.3.2 X-ray Drive Asymmetry

A relation for quantifying the symmetry requirement is given by Hauer et al. [24]. The compression ratio is the ratio of the initial to final fuel radius, $r_0/r_{\text{final}} = C_r$. Given $C_r = 10$, the variation in the radius, $\Delta r/r_{\text{final}}$, due to the variation in the implosion velocity $\Delta v/v$ is given by

$$\frac{\Delta r}{r_{\text{final}}} \cong \frac{r_0}{r_{\text{final}}}\frac{\Delta v}{v} = C_r\frac{\Delta v}{v}, \tag{1.3}$$

where $\Delta v/v \sim (\Delta T_r)^{1.5}$.

For a 2:1 distortion of the compression to take place, $\Delta r/r_{\text{final}} = 1$. Given a $C_r \sim 10$, $\Delta v/v \sim 0.1$. To attain less than 10% variation in the velocity, the variation in the radiation temperature must be less than 7%. Since the flux is proportional to T_r^4, the symmetry of the

[1] Located at LLNL, 192 beams of the NIF laser operate at a wavelength of 351 nm with a peak intensity of 3×10^{15} W/cm^2 in a spot size of $300-500$ μm. Over $\mathcal{O}(10)$ ns, NIF delivers 1.8 MJ.

[2] 351 nm corresponds to a critical density n_c where $n_c = 9 \times 10^{21}$ #/cm^{-3}. The laser cannot penetrate plasma densities higher than the critical density.

X-ray flux must be within 2%. In experiments and simulations conducted after the writing of ref. [24], the compression ratio is typically $20 - 40$. Such a high compression ratio requires X-ray drive symmetry of better than 1% [23, 21, 25].

Asymmetry may arise from non-uniformities in the generation of the X-rays from laser energy, and the transport of those X-rays. The electrons that gain energy from the laser by collisional heating excite transitions in Au that then produce soft X-rays.

A study on radiation temperatures in hohlraums [26] showed that the radiation temperature reaches its peak a few ns after the beginning of full pulse. Non-uniformities in the plasma temperature may arise during the rise time of the radiation drive and modify the symmetry of the drive. Recent experiments acquired X-ray images of a ViewFactor hohlraum [27]. While the results discussed the changing size of the laser entrance hole, the hard X-ray images from the open side of the hohlraum showed an eight-fold bubble pattern produced by the eight 50° quads, an adaptation of which is shown in Fig. 1.4. Results like these emphasize accurate modeling of thermal energy transport that is responsible for the heating the wall and generating the radiation. The understanding that electron transport may influence the symmetry of the X-ray drive provides one of the primary motivations of this thesis.

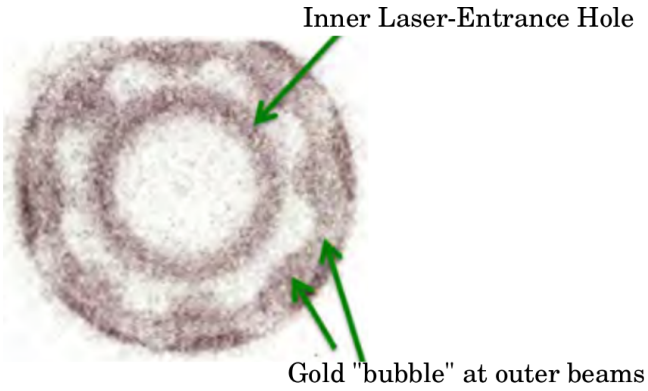

Figure 1.4: An experiment using Viewfactor hohlraums performed X-ray imaging of the hohlraum to determine the size of the laser-entrance holes. The gold ”bubble” shows a feature reflecting the incidence of the 8 outer beams showing increased emission from those regions. Figure adapted from ref. [27].

1.3.3 Electron Transport

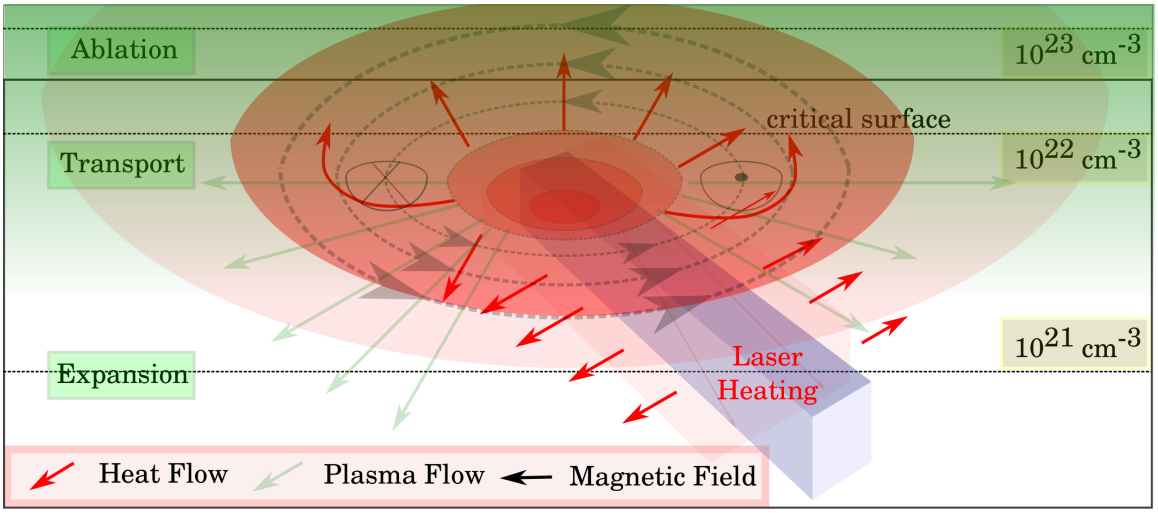

Figure 1.5: The important regions of an electron plasma profile with laser incidence. Note that absorption takes place in $0.1 - 1\ n_c$ and electron transport is important near the critical surface and into the overdense plasma. The presence of magnetic fields near the laser heating region deflects the heat flow.

The thermal energetics in a laser-heated plasma is governed by the significantly lighter electrons. Quantifying the electron temperature in a plasma, especially one that is not optically thick, requires careful consideration of energy transport in the region where plasma heating occurs. Figure 1.5, taken from ref. [25], helps illustrate the fact that the laser energy is absorbed in the underdense electron plasma and electron transport determines the thermal energy distribution in the nearby overdense and underdense plasma [28, 29]. One of the important quantities in electron transport and thermal energy dynamics is the heat flow.

The inhibition of heat flow has been observed in laser-produced exploding-foil plasmas. For example, an experiment by Montgomery et al. [30] involving the measurement of the X-ray emission from a 351 nm, 10^{15} W/cm^2 laser-foil interaction showed that the propagation velocity of the emission ring disagreed with that produced by simulations. Once the heat flow in the simulations was scaled down significantly, better agreement was found

between experiment and modeling. Two primary reasons behind the disagreement were proposed: *non-local* transport and magnetic fields.

A similar conclusion was reached in hohlraum experiments a few years later, where it was suggested that the physics implemented in existing electron transport codes was not sufficient. Glenzer et al. [31] presented Thomson scattering measurements of electron and ion temperatures in a hohlraum. The observed ion temperatures and plasma flows were consistent with modeling. However, quantities that strongly depend on electron transport, such as the electron temperature, were not modeled correctly. The deviations were attributed to inhibited electron transport due to non-local effects.

1.3.3.1 Non-local Transport

Non-local transport arises when the diffusive approximation to the heat flow breaks down[3]. Similar measurements of lower thermal conductivity have suggested the influence of non-local effects [32].

Hawreliak et al. [33] performed measurements of the heat flow using Thomson scattering . The obtained scattering spectrum showed good agreement with a spectrum reconstructed using a *kinetic* calculation of the heat flow using a code known as IMPACT. The spectrum constructed using Spitzer-Harm theory represented a consistently over-calculated heat flow and required the use of a flux-limiter.

The inclusion of a model by Froula et al. that captures some non-local effects is supported by experimental measurements in a hohlraum [34]. However, the results were inconclusive since some Thomson scattering data showed better agreement with flux-limited diffusion models. Experiments measuring X-ray emission from a gold sphere at OMEGA were best modeled using higher flux-limiters than previously assumed. The model developed by Schurtz et al. [35, 36, 37] was implemented along with an improved opacity model

[3]Non-local transport is discussed further in Section 2.2.3

[38] and showed better agreement with NIF data [39, 40].

In addition to non-local transport, it has been suggested that the presence of magnetic fields in the hohlraum plasma [41, 42] may be affecting the thermal transport dynamics.

1.3.3.2 Self-Generated Magnetic Fields

Stamper et al. discussed the existence of laser-generated magnetic fields[4] that arise due to thermoelectric currents in plasma [43]. Thermal energy transport has been shown to be affected by magnetic fields [44] as magnetic fields act to confine charged particles to a characteristic distance defined by the strength of the magnetic field, r_L, known as the Larmor radius. By this principle, magnetic fields have been shown to suppress non-local transport [45].

The previously mentioned experiments by Montgomery et al. [30] and Glenzer et al. [31] suggested the presence of magnetic fields. An experiment measuring heat wave propagation by Gizzi et al. [46] also suggested the presence of non-local transport and magnetic fields. The model developed by Schurtz et al. [35, 36, 37] that includes magnetic fields and non-local transport was implemented in a radiation-hydrodynamics code and proved to be essential in reproducing X-ray emission data from an experiment measuring heat flow propagation.

Similarly, new modeling including Mega Gauss (MG) strength magnetic fields was performed [41] to possibly provide an explanation for the disagreement in previously mentioned Thomson scattering measurements by Glenzer et al. [31]. The modeling with the inclusion of the MG fields gave better agreement with the experimental measurements of electron temperature and provided indirect evidence for the existence of magnetic fields [21]. Proton radiography of electromagnetic fields in laser-plasma experiments has provided direct evidence of MG strength self-generated magnetic fields in laser-foil geome-

[4] Self-generated fields are discussed further in Section 2.3

tries [47, 48], direct-drive capsules [49], hohlraum inner critical surfaces [50], and laser entrance holes [51].

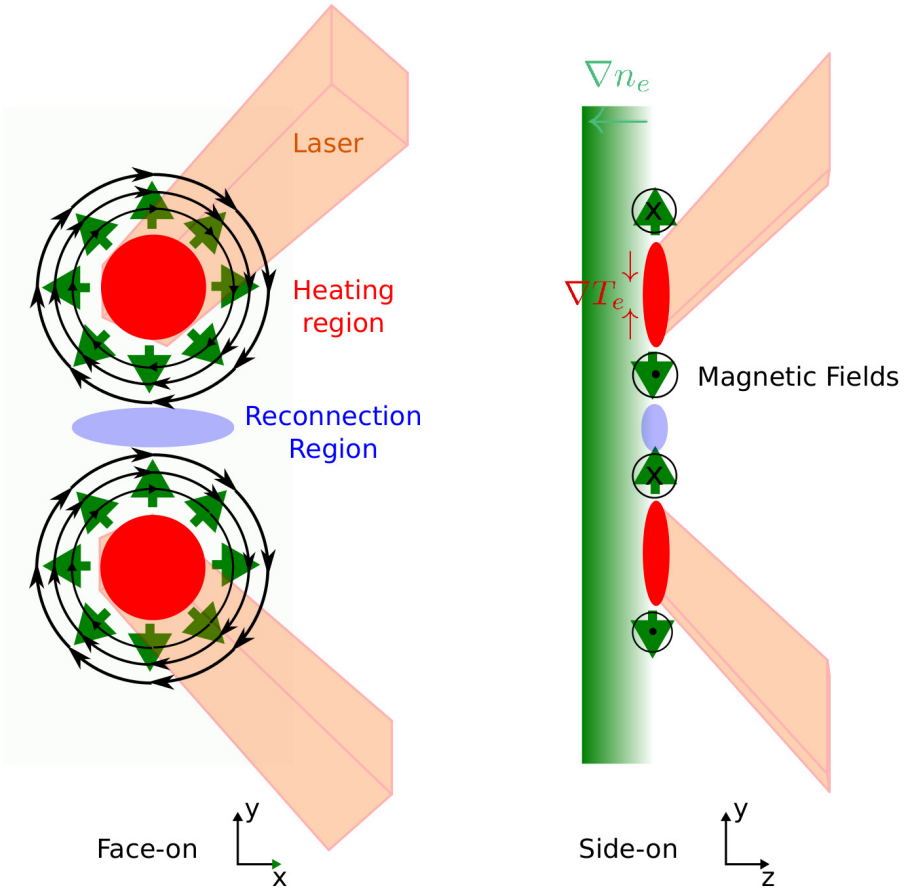

Figure 1.6: The magnetic fields formed around two nearby laser heated regions due to the crossed gradients in temperature and density result in a magnetic reconnection geometry.

Many of the two-spot laser-foil interaction geometries are aligned such that the self-generated magnetic fields from each spot are anti-parallel to one another. Such a geometry is shown in Fig. 1.6. In an experiment with two laser beams incident in close proximity on a planar solid target, Nilson et al. performed optical probing and proton grid deflectometry to measure out-flowing jets and MG strength magnetic fields at the focal spot edges [52, 53]. A similar effort was undertaken by Li et al. [47]. This platform has enabled unique experiments studying asymmetric reconnection relevant to astrophysical phenomena [54] where magnetic reconnection has been suggested to result in particle acceleration

[55]. Modeling [56, 57] and experiments [54] have suggested the importance of collisional effects. In the context of a hohlraum, the oppositely aligned magnetic fields may result in thermal transport inhibition. The reconnection of these field lines may alter the thermal transport dynamics by enabling the redistribution of thermal energy because of changes in magnetic topology.

Therefore, kinetic modeling of electron thermal transport that includes magnetic field effects may be of great relevance to hohlraum energetics. The motivation for this work is summarized in the following section, and the regime of applicability is discussed by comparing the effects of radiation transport to thermal transport.

1.4 Thermal vs. Radiation Transport

Furthering the understanding of the complex interplay between magnetic field dynamics and thermal energy transport produced in hohlraum-like conditions using kinetic modeling is the primary objective of this thesis. This is motivated by the need for better modeling of the electron transport dynamics in the plasma near the laser absorption region in a hohlraum.

Even in a device that is dominated by radiation, the relevance of electron transport can persist. ICF simulations (like those in refs. [58, 4, 23, 41, 21, 6, 22, 7]) have been performed using radiation-hydrodynamic modeling that is subject to some approximations regarding the influence of magnetic fields and detailed treatment of the electron thermal energetics with inclusion of effects such as non-local transport. The self-consistent modeling of non-local transport in magnetic fields, among other effects, is implemented here by using a kinetic formulation to describe the plasma, and discussed in Chapter 2. On the other hand, the kinetic modeling performed here does not include radiation transport effects. Quantifying these effects is necessary to examine their exclusion, and can be done

by comparing the amounts of energy associated with the emitted radiation and the incident radiation. The free-free emission in the form of Bremsstrahlung radiation either diffuses into the dense gold as a Marshak wave or is emitted towards the center of the hohlraum. The blackbody radiation field is the incident radiation. The heat flow from radiation diffusion into the gold is calculated first to determine whether it is significant in comparison to the incident laser intensity.

Radiation diffuses into the dense gold plasma because the X-ray mean-free-path is very short. From ref. [21], the X-ray mean-free-path, λ, in Au is given by

$$\lambda\ (\mu\text{m}) = 3.55 \times 10^{-2} \left[T_R\ (\text{eV})\right]^{1.5}. \tag{1.4}$$

A typical hohlraum wall is 25 μm thick [19]. For radiation temperatures of 300 eV, $\lambda \approx 0.2$ μm suggesting that the dense gold is optically thick with respect to the X-rays. The diffusive transport of radiation can be characterized by a Marshak wave [25]. An energy balance between the Marshak wave, laser (given the previous assumption that half of the energy is in the dense gold interaction), and an electron plasma of density n_e can be approximated by

$$\frac{d}{dt}(n_e k_B T_e x_M) = 0.5 I_L - \sigma T^4, \tag{1.5}$$

where x_M is the penetration depth of the Marshak wave, I_L is the energy from the laser, and σT^4 is the energy flux of the X-ray radiation from the dense plasma. An estimate for x_M by M. D. Rosen, given in refs. [23, 21], is

$$x_M = 0.53 T_o^{1.86} t_{ns}^{0.75}\ \mu\text{m}, \tag{1.6}$$

where T_o is the temperature of the material at the outer boundary of the gold at 1 ns in 100s of eV, and t is the time in nanoseconds. Assuming the hohlraum wall temperature is

approximately 200 eV, the thickness of the heated region is about 2 μm. The X-rays heat the dense material over very small length scales and the radiation is re-emitted.

The left side of Eq. (1.5) quantifies the heat transported by the Marshak wave. The speed of the wave is 1.4 μm/ns. Since the wave is too slow to respond to fast fluctuations in the electron density and temperature, those quantities are effectively in steady state. Using the approximate velocity calculated above along with $n_e \approx 10^{22}$ cm^{-3} and $T_e \approx 300$ eV, the heat flow in the Marshak wave is approximately 10^9 W/cm^2. The negligible amount of energy carried by the Marshak wave in comparison to the laser intensity of 3×10^{15} W/cm^2 suggests that the energy fluxes in the hohlraum are balanced by the energy in the plasma in the laser-absorption region, the energy in the blackbody radiation field, and the radiation emitted by the plasma. Calculating the energy density in the three systems enables the quantification of radiation effects on thermal transport.

The internal energy density of a plasma dominated by electron pressure is given by

$$e_{\text{e-plasma}} = \frac{3}{2} n_e k_B T_e.$$

For a near-critical, few keV plasma, this is approximately 500 kJ/cm^3. The energy density of blackbody radiation at a temperature T is

$$e_{\text{rad}} = 4 \frac{\sigma_{SB}}{c} T^4.$$

For 250 eV radiation, the energy density is approximately 50 kJ/cm^3. Furthermore, because the near-critical plasma where electron transport takes place has to be transparent to the radiation field since it is in between the fuel and the blackbody emitter, the local energy-density of blackbody radiation is calculated by multiplying the global radiation-energy-

density with the local Bremsstrahlung optical depth, τ, from ref. [59] given by

$$\tau = 5 \times 10^{-38} n_e n_i Z^2 \bar{g} L T^{-7/2},$$

where n_e and n_i are the electron and ion density in cm^{-3} and $\bar{g}$ is the Gaunt factor of order unity. L is the scale length of concern in cm and T is the radiation temperature in eV. For a sub-critical plasma density of 10^{21} cm^{-3}, this gives $\tau = 0.02$ showing that the plasma is optically thin to the blackbody radiation field. For the critical and overdense plasma, $\tau \lesssim 1$. Therefore, the local blackbody energy density is approximately $5 - 50$ kJ/cm^3, $1 - 10\%$ of the total internal energy density depending on the region of interest.

Much like in the consideration of Eq. (1.2), the plasma here is also susceptible to radiation losses in the form of Bremsstrahlung emission. The power per unit volume emitted in the laser-heating region is given by

$$P_{\text{Br}} = 1.69 \times 10^{32} n_e \sqrt{T_e} Z^2 n_i \, \frac{\text{W}}{\text{cm}^3},$$

from ref. [60]. Over the nanosecond time-scales considered here, this gives 50 kJ/cm^3, 10% of the plasma thermal energy density. Since radiation heating and cooling are both roughly 10% effects, their inclusion may alter thermal energy dynamics by $\pm 20\%$. However, the emitted radiation may balance the absorption from the blackbody radiation leading to a smaller net change in thermal energy. The overall conclusion is that the thermal energy dynamics in near-critical laser-plasmas are governed by electron transport, while radiation may affect the calculations by $\pm 10\%$.

1.5 Thesis Outline

The study of self-generated magnetic fields in hohlraums for this thesis is motivated by the observed MG strength magnetic fields that arise in laser-plasma experiments. These fields may alter the thermal energetics in a hohlraum and affect the uniformity of the X-ray production, or the behavior of laser-plasma interactions that take place in sub-critical plasmas [61, 62, 63]. Furthermore, the self-generated magnetic fields align in magnetic reconnection geometries that may influence the thermal energetics by confining or releasing electron thermal energy depending on the topology of the magnetic field.

The details of the affect of magnetic fields on thermal energy transport, and vice versa, will be elaborated upon in Chapter 2, along with a presentation of a kinetic formulation for electron transport. The code that is used to perform the calculations is described in Chapter 3. The author was responsible for the development of a ray-tracing module to model laser propagation, and the modeling and theoretical work in Chapters 4 to 6. Using this code, nanosecond time-scale simulations of a full-scale 2D Cartesian hohlraum were performed by the author. The first results of the inclusion of self-generated magnetic field with kinetic electron transport are presented in context of a full 2D hohlraum geometry and a reconnection geometry, in Chapters 4 and 6, respectively, and the kinetic effects in heat flow and magnetic-field-generation are discussed. Recent interest in the application of an external magnetic field on a hohlraum lends for an extension of the work in Chapter 4 and is presented in Chapter 5 where the first kinetic modeling of transport of an externally applied magnetic field in a hohlraum is presented and discussed.

Chapter 2 - Theoretical Background

The plasma parameters that are used to characterize different plasma regimes describe the context of the work. The description of a plasma using a kinetic approach, where the

distribution function information is preserved, eliminates the need for the approximations in the fluid approach. The effect of these approximations on Classical Transport theory shows that some modifications to the theory may be needed. Non-local transport arises in the presence of steep gradients and laser heating disturbs the distribution away from a Maxwell-Boltzmann distribution. The transport phenomena that arise in magnetized inertial fusion plasmas due to magnetic fields, laser heating, and non-local effects using kinetic theory can be compared against those produced from fluid modeling and Braginskii transport.

Chapter 3 - IMPACTA

The kinetic modeling used throughout the thesis is performed using IMPACTA, a MPI C++ code with a Vlasov-Fokker-Planck model for electrons with full electromagnetic fields and cold ion hydrodynamics. The dimensionless equations give the normalizations to the physical quantities. The finite differenced equations are provided. A section on the algorithm for the ray tracing package includes the finite differenced ray-tracing equations.

Chapter 4 - Magnetic Field Generation due to Laser Heating in Hohlraum

The implementation of ray-tracing to model laser propagation through the hohlraum plasma allows for nanosecond time-scale modeling of a hohlraum geometry plasma. The generation of 50 MG magnetic fields due to pressure gradients results in magnetized plasmas where thermal energy transport is affected due to the presence of magnetic fields. The introduction of the Righi-Leduc effect leads to different temperature profiles and heat flow and suppression of heat flux perpendicular to magnetic fields is observed. The presence of non-local transport is shown through heat flow comparisons. The signatures of non-local transport and inverse-Bremsstrahlung heating are also observed in plots of the distribution function.

Chapter 5 - Compression and Cavitation of Externally Applied Magnetic Field in Hohlraum

The effect of super-Gaussian distributions and non-local transport with 3D magnetic fields is discussed. Thermal gradients result in Nernst convection of the externally applied magnetic field away from the laser heated region. The kinetic Ohm's Law derived from the self-consistent equation set suggests that there could be a strong influence of non-local heat flow on the magnetic field dynamics. The magnetic field compresses due to heat flow towards the hohlraum wall. The magnetic field is also transported towards the hohlraum axis due to heat flow on time-scales much faster than that calculated through the "frozen-in-flux" mechanism. Non-locality contributes significantly to the magnetic field transport mechanism. Consideration of non-locality in the Nernst flow is required to accurately assess the state of the initially uniform magnetic field.

Chapter 6 - Heat Flux Mediated Magnetic Reconnection

The self-generated magnetic fields discussed in chapter 2 form distinct magnetic reconnection geometries where the plasma is magnetized and separated by magnetic fields aligned in opposing directions. The principles of magnetic reconnection state that the magnetic field requires a convection mechanism and a "field-breaking" mechanism. From the Ohm's Law from Chapter 2, heat flux convection of the magnetic field can provide for magnetic reconnection as well. Modeling of the reconnection of self-generated magnetic fields in an ICF regime plasma shows that reconnection occurs through advection of the magnetic field with the heat flux and results in redistribution of thermal energy.

CHAPTER 2

Theoretical Background

Choosing a suitable model is a necessary step in describing any phenomenon. This thesis is concerned with the dynamic interaction of laser-heated plasmas with magnetic fields for which one of the well-known models is the *Vlasov-Fokker-Planck* (VFP) model [64]. The following chapter discusses the electron VFP equation and its origins from the greater context of plasma kinetic theory. It shows the derivation of the electron fluid equations from the VFP equation given certain assumptions. The electron fluid equations provide a basis for classical transport theory [44] and modified classical transport that includes the effects of laser-heating [65] that enable comparison to kinetic theory. In particular, the modified or novel, thermal- and magnetic-phenomena that arise from kinetic transport show when the classical transport theories may be invalidated.

2.1 Describing A Plasma

The kinetic theory of gases where macroscopic phenomena are representative of the collective effects of large ensembles of particles can be extended to plasmas. In plasmas, the electromagnetic forces between the charged particles contribute to the dynamics; over short scales, the Coulomb collisions are influential and over large scales, the macroscopic fields and currents induced by charge separation dominate. A fully ionized plasma is a col-

lection of ions and electrons that is subject to electromagnetic forces arising from charge displacement as well as particle interactions in the form of Coulomb collisions. The electrons in the plasma are able to respond and neutralize charge displacements by virtue of their thermal energy. The range over which they can do so is given by the Debye length, $\lambda_D = (\epsilon k_B T_e / n e^2)^{1/2}$ where ϵ is the permittivity, k_B is Boltzmann's constant, T_e is the temperature of the electrons, n is the electron density, and e is the elementary charge. This phenomenon prevents the plasma from creating charge separation over distances exceeding the Debye length due to thermal fluctuations because the charged particles do not possess enough kinetic energy. The converse of this effect is also true. Imposed electromagnetic fields can only create charge separation on length scales longer than a Debye length because the field will be shielded over smaller volumes. Therefore, the Debye length is the minimum length over which electromagnetic fields set up by charge separation exist in a plasma and the maximum distance over which individual Coulomb interactions are influential.

In a fully ionized plasma, Coulomb collisions between the charged particles are the only relevant collisions and the process can be described by Rutherford scattering. For collisions between ions and electrons, the impact parameter b, collision speed u and collision angle θ are related by

$$\tan(\theta/2) = \frac{b_{90}}{b}, \text{ where } b_0(u) \approx \frac{Z^2 e^2}{4\pi\epsilon_0 m_e u^2} \tag{2.1}$$

is the impact parameter for 90° scattering [66]. Since b and θ are related, the number of collisions with impact parameter $[b, b + db]$ can be directly related to the number scattered into the solid angle $d\Omega = 2\pi \sin(\theta) d\theta$. The cross section $\sigma(\theta)$ is found by solving

$$\sigma(\theta) d\Omega = 2\pi b \, db \tag{2.2}$$

to give

$$\sigma(\theta) = \frac{b}{\sin\theta}\frac{db}{d\theta} \tag{2.3}$$

$$\approx \frac{Z^4 e^4}{(4\pi\epsilon)^2 m_e^2 u^4}\frac{1}{4\sin^4(\theta/2)}. \tag{2.4}$$

Since $\sigma \propto \sin^{-4}(\theta/2)$, collisions that result in small angle deflections are much more likely than those leading to large deflections and large angle deflections can be neglected. With this knowledge and the Debye length, the range for important impact parameters is narrowed down to $b_{90} < b < \lambda_D$. The logarithm of the ratio, λ_D/b_{90}, is an important parameter in collisional plasma physics and termed the *log Lambda*, or Coulomb Logarithm, of the plasma and is related to the particle number density within a Debye sphere by

$$\ln\left[\frac{\lambda_D}{b_{90}}\right] = \ln\left[\frac{9}{Z}\frac{4\pi}{3}n_e\lambda_D^3\right] = \ln\frac{9N_D}{Z} \equiv \ln\Lambda_{ei}. \tag{2.5}$$

The Coulomb Logarithm provides a measure for the relative importance of Coulomb collisions in the plasma to collisionless phenomena by relating the plasma frequency to the electron-ion collision frequency ν_{ei}. This relation, given in ref. [64], is

$$\frac{\omega_p}{\langle\nu_{ei}\rangle} = \sqrt{\frac{\pi}{2}}\frac{\Lambda_{ei}}{\ln\Lambda_{ei}}. \tag{2.6}$$

Using this formula, a relationship between the plasma conditions and the relative collisionallity of plasma is established.

Figure 2.1 shows the collisionallity for various man-made and natural plasmas. The top left of the chart corresponds to a negligibly small collision frequency in comparison to the plasma frequency. In this situation, the plasma can be considered effectively collisionless. The bottom right of this chart corresponds to dense and cold plasmas that are strongly coupled such that the strong binary forces invalidate Debye theory [68]. In the intermediate

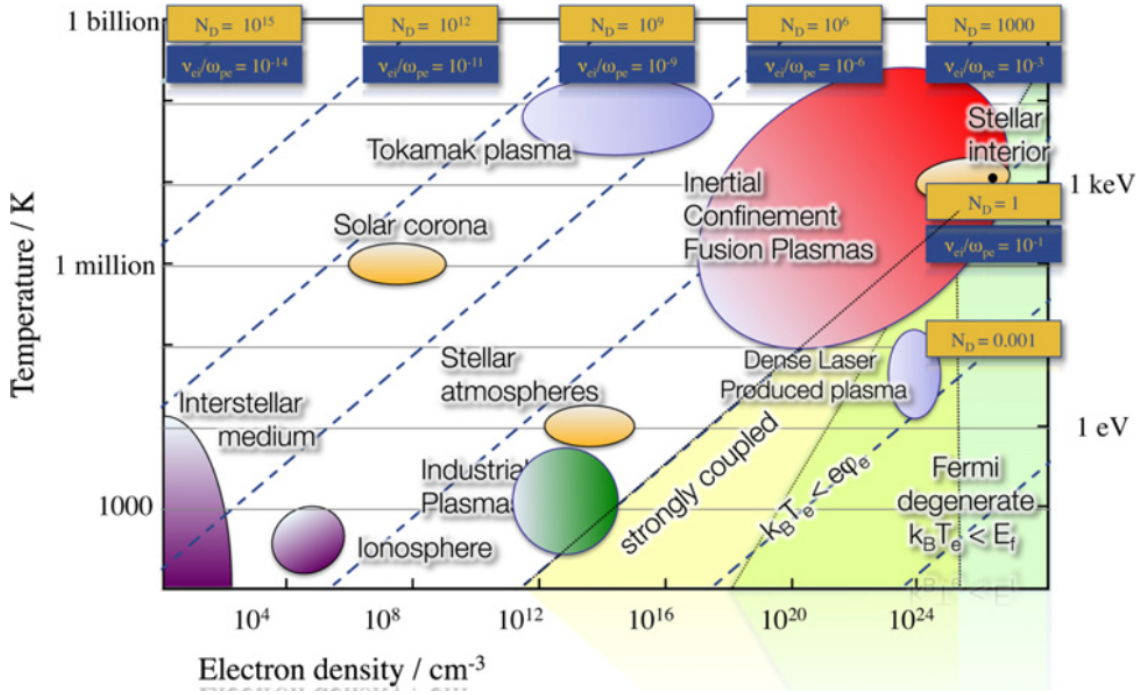

Figure 2.1: The relationship between relative collisionallity ν_{ei}/ω_p and number of particles in a Debye sphere on a density temperature phase-space for plasmas. Figure taken from ref. [67].

regime, the plasmas are semi-collisional where $\omega_p \sim (10 - 100) \times \nu_{ei}$. Laser heating from 351 nm fusion lasers typically occurs near plasma densities of 10^{21} #/cc creating plasmas with temperatures of 1 million Kelvin. In this regime, the Coulomb collisions cannot be neglected, while collective phenomena associated with the plasma frequency remain relevant.

In the rest of the thesis, the two most common methods of describing semi-collisional plasmas, the fluid and kinetic approach, are compared in the context of plasma conditions similar to those in, but not limited to, the laser heating regions in a hohlraum.

2.1.1 Particle Kinetics of a Plasma

Under the conditions studied in this thesis, a plasma is a system of charged particles that undergo long-range interactions through electromagnetic forces as well as short-range in-

teractions through Coulomb collisions. A mathematical foundation for a description of a plasma must include both of these effects. First the plasma needs to be quantified as a group of particles.

The distribution function f of a collection of particles of number d^6N in a spatial volume, d^3r and of a certain velocity within the volume d^3v of velocity space is defined by

$$d^6N \equiv f\ d^3r\ d^3v. \tag{2.7}$$

The number density per unit volume, n, can be calculated with an integral over all velocities and is given by

$$n = \int f d^3v. \tag{2.8}$$

This formulation suggests that the distribution function from Eq. (2.7) is the number density in a 6-dimensional phase space that encompasses real and velocity space such that a vector ζ [64] is given by

$$\boldsymbol{\zeta} = \mathbf{r} + \mathbf{v}. \tag{2.9}$$

The phase space velocity is given by

$$\frac{d\boldsymbol{\zeta}}{dt} = \frac{d\mathbf{r}}{dt} + \frac{d\mathbf{v}}{dt} = \mathbf{v} + \frac{d\mathbf{v}}{dt}. \tag{2.10}$$

An equation conserving the distribution function in phase space is given by

$$\frac{\partial f}{\partial t} + \nabla_\zeta \cdot \left(f \frac{\partial \zeta}{\partial t} \right) = \text{source terms} = \frac{\delta f}{\delta t}, \tag{2.11}$$

where

$$\nabla_{\boldsymbol{\zeta}} = \frac{\partial}{\partial r_i}\mathbf{i}_{r_i} + \frac{\partial}{\partial v_i}\mathbf{i}_{v_i} \tag{2.12}$$

is the gradient operator over $\boldsymbol{\zeta}$ space. The first term of Eq. (2.11) describes the change in distribution function over time while the second describes the change in the distribution function over $\boldsymbol{\zeta}$ space. These changes are balanced by the term on the right side. Expanding the gradient operator over configuration and velocity space gives

$$\frac{\partial f}{\partial t} + \nabla_{\mathbf{r}} \cdot (f\mathbf{v}) + \nabla_{\mathbf{v}} \cdot \left(f \frac{d\mathbf{v}}{dt} \right) = \frac{\delta f}{\delta t}, \tag{2.13}$$

where $\nabla_{\mathbf{r}} = \partial \mathbf{i}_{r_i} / \partial r_i$ and $\nabla_{\mathbf{v}} = \partial \mathbf{i}_{v_i} / \partial v_i$ are the gradients in space and velocity. Therefore, $\nabla_{\mathbf{r}} \cdot \mathbf{v} = 0$. The acceleration term can be expanded by using forces using the relation $d\mathbf{v}/dt = \mathbf{F}/m$ where $\mathbf{F}$ is the force. Because of the electromagnetic nature of the plasma, substituting for the Lorentz force gives

$$\frac{d\mathbf{v}}{dt} = \frac{e}{m_e} \left(\mathbf{E} + \mathbf{v} \times \mathbf{B} \right). \tag{2.14}$$

Since the electrostatic force is not dependent on velocity, $\nabla_{\mathbf{v}} \cdot \mathbf{E} = 0$. The velocity divergence of the $\mathbf{v} \times \mathbf{B}$ term can be expanded to

$$\nabla_{\mathbf{v}} \cdot (\mathbf{v} \times \mathbf{B}) = \mathbf{v} \cdot (\nabla_{\mathbf{v}} \times \mathbf{B}) + \mathbf{B} \cdot (\nabla_{\mathbf{v}} \times \mathbf{v}). \tag{2.15}$$

Since the magnetic field is not dependent on the velocity and $\nabla_{\mathbf{v}} \times \mathbf{v} = 0$, $\nabla_{\mathbf{v}} \cdot d\mathbf{v}/dt = 0$. Assuming that the acceleration is due to forces where $\nabla_{\mathbf{v}} \cdot d\mathbf{v}/dt$ results in a simplification of the divergence form of the position-velocity-space conservation equation, and Eq. (2.13) can be rewritten as

$$\frac{\partial f}{\partial t} + \mathbf{v} \cdot \nabla_{\mathbf{r}} f + \frac{d\mathbf{v}}{dt} \cdot \nabla_{\mathbf{v}} f = \frac{\delta f}{\delta t}. \tag{2.16}$$

When the right side of the above equation is the result of collisions, the relation is known as the Boltzmann equation. In a collisionless system, where the right-hand-side is

0, subject to the Lorentz force, the Boltzmann equation reduces to the Vlasov equation.

Calculating the effect of Coulomb collisions on particle distribution functions is a difficult problem because of the infinitely long range electro-static force. In plasmas, however, electron shielding of charge imbalances over scales longer than a Debye length provides a convenient cut-off for Coulomb collisions. The minimum distance of interaction is the impact parameter for large-angle scattering. Collisions with impact parameters, b, in between those two limits, i.e. $b_{90} < b < \lambda_D$, result in small-angle collisions rather than large-angle deflections. To treat changes to a distribution function from frequent collisions that result in small momentum changes of each particle, a Fokker-Planck operator may be used [69].

2.1.2 Vlasov-Fokker-Planck Equation

The collisional term can be described by using a series expansion for the statistically averaged deflection felt by each particle. Let $\Delta\mathbf{v}$ be the change in velocity induced by multiple, small-angle Coulomb collisions. If $\Psi(\mathbf{v}, \Delta\mathbf{v})$ is the probability that in a time Δt an electron will be deflected by $\Delta\mathbf{v}$ to a new velocity $\mathbf{v}$ from velocity $\mathbf{v} - \Delta\mathbf{v}$, then the relations that describe the deflections averaged over a velocity distribution function are

$$\langle \Delta\mathbf{v} \rangle = \int \Psi(\Delta\mathbf{v}) \Delta\mathbf{v} \; d(\Delta\mathbf{v}), \tag{2.17}$$

$$\langle \Delta\mathbf{v}\Delta\mathbf{v} \rangle = \int \Psi(\Delta\mathbf{v}) \Delta\mathbf{v}\Delta\mathbf{v} \; d(\Delta\mathbf{v}). \tag{2.18}$$

$\langle \Delta\mathbf{v} \rangle$ refers to the average change in velocity of a particle distribution function of velocity $\mathbf{v}$. Physically, this can be described as dynamical friction. $\langle \Delta\mathbf{v}\Delta\mathbf{v} \rangle$ refers to the average spread in the velocity of a particle traveling at velocity $\mathbf{v}$. Analogous to position space diffusion, this term can be described as diffusion in velocity space.

In these conditions, the Boltzmann equation reduces to the electron Vlasov-Fokker-

Planck (VFP) equation given by

$$\left[\frac{\partial}{\partial t} + \mathbf{v}\cdot\nabla_r - \frac{e}{m_e}(\mathbf{E}+\mathbf{v}\times\mathbf{B})\cdot\nabla_v\right] f(t,\mathbf{r},\mathbf{v}) =$$
$$-\nabla_v\cdot\left\{f(t,\mathbf{r},\mathbf{v})\frac{\langle\Delta\mathbf{v}\rangle}{\Delta t}\right\} + \frac{1}{2}\nabla_v\nabla_v : \left\{f(t,\mathbf{r},\mathbf{v})\frac{\langle\Delta\mathbf{v}\Delta\mathbf{v}\rangle}{\Delta t}\right\}. \tag{2.19}$$

Equation (2.19) solves for the evolution of the distribution in the presence of microscopic and macroscopic forces, represented by collisions and electromagnetic forces, respectively.

2.1.3 Relation to Macroscopic Quantities

The various macroscopic variables associated with a distribution function of a system of particles, such as density and temperature, are calculated by "taking velocity moments" of the distribution function, where the microscopic effects are averaged over a distribution function to provide a macroscopic quantity. For particles of number density, n, the m^{th} order velocity tensor is $\{\mathbf{v}^m\} = \mathbf{v}\mathbf{v}...\mathbf{v}$, the m^{th} order moment is defined by

$$n\langle\{\mathbf{v}^m\}\rangle \equiv \int \mathbf{v}\mathbf{v}...\mathbf{v} f(\mathbf{r},\mathbf{v},t)\, d^3\mathbf{v} = \overline{\mathbf{v}\mathbf{v}...\mathbf{v}}. \tag{2.20}$$

Thus, the m^{th} order moment is a measure of the expectation value of $\{\mathbf{v}^m\}$. Using this fact, common macroscopic electron plasma quantities are given below in their moment forms:

$$0^{\text{th}}\text{ moment: } n_e(\mathbf{r},t) = \int f(\mathbf{r},\mathbf{v},t)\, d^3\mathbf{v}, \tag{2.21}$$

$$1^{\text{st}}\text{ moment: } \bar{\mathbf{v}}(\mathbf{r},t) = \frac{1}{n_e}\int \mathbf{v} f(\mathbf{r},\mathbf{v},t)\, d^3\mathbf{v}, \tag{2.22}$$

$$2^{\text{nd}}\text{ moment: } \underline{\underline{\mathbf{P}}}(\mathbf{r},t) = m_e\int \mathbf{v}\mathbf{v} f(\mathbf{r},\mathbf{v},t)\, d^3\mathbf{v}, \tag{2.23}$$

$$\text{Heat Flow: } \mathbf{q}(\mathbf{r},t) = \frac{1}{2}m_e\int v^2\mathbf{v} f(\mathbf{r},\mathbf{v},t)\, d^3v, \tag{2.24}$$

where n_e is the electron density, the mean velocity, $\bar{\mathbf{v}}$, is associated with the current density because $\mathbf{j} = -en_e\bar{\mathbf{v}}$. $\mathbf{q}$ is the heat flow and $\underline{\underline{\mathbf{P}}}$ is the pressure tensor given by

$$\underline{\underline{\mathbf{P}}} = P\underline{\underline{\mathbb{I}}} + \underline{\underline{\mathbf{\Pi}}}, \tag{2.25}$$

where P is the scalar pressure and $\underline{\underline{\mathbb{I}}}$ is the identity tensor. $\underline{\underline{\mathbf{\Pi}}}$ represents the off-diagonal contributions to the pressure.

2.1.4 Electron Fluid Equations

The electron fluid equations describe the relationship between the macroscopic quantities, and therefore, can be derived by using the VFP equation. Calculating the m^{th} moment of Eq. (2.19) may be written as

$$\frac{\partial}{\partial t}(n_e\langle\mathbf{v}^m\rangle) + \nabla_{\mathbf{r}}\cdot(n_e\langle\mathbf{v}^{m+1}\rangle) - \langle n_e(\mathbf{E}+\mathbf{v}\times\omega)\cdot\nabla_{\mathbf{v}}\mathbf{v}^m\rangle = \langle n_e C(f)\mathbf{v}^m\rangle, \tag{2.26}$$

with the Fokker-Planck terms abbreviated to $C(f)$. Equation (2.26) consists of a set of infinitely coupled equations due to the presence of both $\langle\mathbf{v}^m\rangle$ and $\langle\mathbf{v}^{m+1}\rangle$ moments.

The fluid equations are a set of equations describing the conservation of density, momentum, and energy. These refer to the $m = 0, 1, 2$ moments of Eq. (2.26) which are

$$\frac{\partial n_e}{\partial t} + \nabla\cdot(n_e\langle\mathbf{v}\rangle) = 0, \tag{2.27}$$

$$m_e\left(\frac{\partial}{\partial t}(n_e\langle\mathbf{v}\rangle) + \nabla\cdot(n_e\langle\mathbf{v}\rangle\langle\mathbf{v}\rangle)\right) + \nabla\cdot\underline{\underline{\mathbf{P}}} + en_e(\mathbf{E}+\langle\mathbf{v}\rangle\times\mathbf{B}) = \Delta\mathbf{p}_{ei}, \tag{2.28}$$

$$\frac{3}{2}\frac{\partial P}{\partial t} + \frac{\partial}{\partial t}\left(\frac{1}{2}m_e\langle\mathbf{v}\rangle\cdot\langle\mathbf{v}\rangle\right) + \nabla\cdot\mathbf{q} + en_e\langle\mathbf{v}\rangle\cdot\mathbf{E} = 0. \tag{2.29}$$

In this case, the extra variable in the coupled set of equations is the heat flow, $\mathbf{q}$. The momentum exchange between electrons and ions,$\Delta\mathbf{p}_{ei}$ due to collisions needs quantification

and is given by *Ohm's law*.

Provision of the two equations describing the heat flow and Ohm's law give the relations for a tractable set of equations describing the electron fluid and great efforts have been taken for precise calculation of the coefficients used in the transport equations [44, 70], often referred to as Braginskii transport. To obtain the Braginskii transport equations, the authors of refs. [44, 70] exploited an expansion of the Vlasov-Fokker-Planck equation. The modeling of plasma using this expansion and the relation to Braginskii transport is discussed in the following section.

2.1.5 Expansion of Distribution Function

Making Eq. (2.19) computationally feasible requires simplifying the distribution function further in order to reduce the dimensionality of the problem. Since the distribution function is spherical in velocity space, an angular expansion can reduce the number of dimensions of the distribution function by expanding in the orthogonal velocity directions. Moreover, the dominance of electron-ion collisions results in only directional changes in velocity space, rather than magnitude. Using orthogonal, spherical basis functions such as those in the spherical harmonics expansion, the distribution function is expanded as

$$f(v,\theta,\phi) = \sum_{l=0}^{\infty}\sum_{m=0}^{l}\sum_{s=0}^{1} f_{lms}(v)Y_{lms}(\theta,\phi). \tag{2.30}$$

The function describing the spherical harmonics is

$$Y_{lms}(\theta,\phi) = \sqrt{\frac{2l+1}{4\pi}\frac{(l-m)!}{(l+m)!}}\, P_l^m(\cos\theta)(\delta_{0s}\cos(m\phi) + \delta_{1s}\sin(m\phi)), \tag{2.31}$$

where $P_l^m(x)$ is the associated Legendre polynomial and δ_{ij} is the Kronecker Delta function. For $l = 0$ and $l = 1$, $Y_{000} = 1, Y_{100} = \cos\theta = \cos\theta_z, Y_{110} = \sin\theta\cos\phi =$

$\cos\theta_x, Y_{111} = \sin\theta\sin\phi = \cos\theta_y$ give the relations for the direction cosines. Using the summation notation in the expansion gives

$$f = f_{lms}Y_{lms} = f_{000} + f_{100}\cos\theta + f_{100}\cos\theta_z + f_{110}\cos\theta_x + f_{111}\cos\theta_y + ..., \quad (2.32)$$

where the f_{lms} terms are functions of time, position, and *speed* only. The spherical harmonics in the 1st order expansion are the direction cosines of a unit velocity vector, $\hat{v} = \mathbf{v}/v$, and the distribution function can be recast in vector form,

$$f = f_0 + \mathbf{f}_1 \cdot \frac{\mathbf{v}}{v} + ..., \quad (2.33)$$

where $f_{1x} = f_{110}, f_{1y} = f_{111}, f_{1z} = f_{100}$, and $f_0 = f_{000}$ provide the direct relation between the vector and spherical harmonic expansion.

This formalism can be substituted into the VFP equation and rearranged such that the only angular terms are linear combinations of spherical harmonics resulting in a set of $(l+1)^2$ independent equations to solve for the $(l+1)^2$ unknown f_{lms} distributions. The difficulty in using Eq. (2.30) comes from calculation of the non-linear terms $\cos\theta[\partial P_{lm}(\cos\theta)/\partial\theta]$ for which no simple recursion relations have been found [71]. Equation (2.33) says that the spherical harmonics expansion is equivalent to the 1st order tensor expansion. In ref. [71], it is shown that an expansion using what are known as Cartesian tensors is equivalent to the spherical harmonics expansion such that each l^{th} order Cartesian tensor is equivalent to the l^{th} order spherical harmonic.

2.1.6 Cartesian Tensor Expansion

Using this expansion, the distribution function can be formulated as the sum of orthogonal functions based on the three spatial dimensions [71, 72]. The expanded distribution

function is

$$\mathbf{f}(\mathbf{r},\mathbf{v},t)=\sum_{l}\frac{\{\mathbf{f}_l\}\vdots_l\{\mathbf{v}^l\}}{v^l}. \tag{2.34}$$

where $\{\mathbf{f}_l\}$ is a symmetric l^{th} order Cartesian tensor, and

$$\{\mathbf{v}^l\}=\mathbf{v}^i\mathbf{v}^j...\mathbf{v}^k,\ (l\text{ terms}) \tag{2.35}$$

is the l^{th} order Cartesian tensor formed by the Cartesian components $\mathbf{v}^i$ of $\mathbf{v}$ along the 3 axes. Using this, Eq. (2.34) can be rewritten as

$$\begin{aligned}\{\mathbf{f}_l\}\vdots_l\{\mathbf{v}^l\}&=\sum_{ijk}f_{(l)...kji}\frac{v^i}{v}\frac{v^j}{v}\frac{v^k}{v}...\\&=\sum f_{(l)...kji}\cos\theta_i\cos\theta_j...,\end{aligned} \tag{2.36}$$

where $\hat{\mathbf{v}}=v\cos\theta_i\hat{\mathbf{i}}+v\cos\theta_j\hat{\mathbf{j}}+v\cos\theta_k\hat{\mathbf{k}}$ is the unit velocity vector.

The 2^{nd} order expansion of Eq. (2.34) is

$$\mathbf{f}(\mathbf{r},\mathbf{v},t)=f_0(\mathbf{r},v,t)+\mathbf{f}_1(\mathbf{r},v,t)\cdot\mathbf{v}+\underline{\underline{\mathbf{f}}}_2(\mathbf{r},v,t):\frac{\mathbf{vv}}{v^2}+...\ . \tag{2.37}$$

In terms of the direction cosines, it is given by

$$\mathbf{f}(\mathbf{r},\mathbf{v},t)=f_0+f_{1i}\cos\theta_i+f_{2ij}\cos\theta_j\cos\theta_i+..., \tag{2.38}$$

where the Einstein summing convention, $A_iA_i=\sum_i A_iA_i$ and $A_{ij}A_{ik}=\sum_i A_{ij}A_{ik}$, is used.

While the number of terms that describe the distribution function is increased to 9 from 1, this formulation reduces the 7D distribution function to a 5D. $f_0,\mathbf{f}_1,\underline{\underline{\mathbf{f}}}_2$ are only functions of the 3 spatial dimensions, speed, and time.

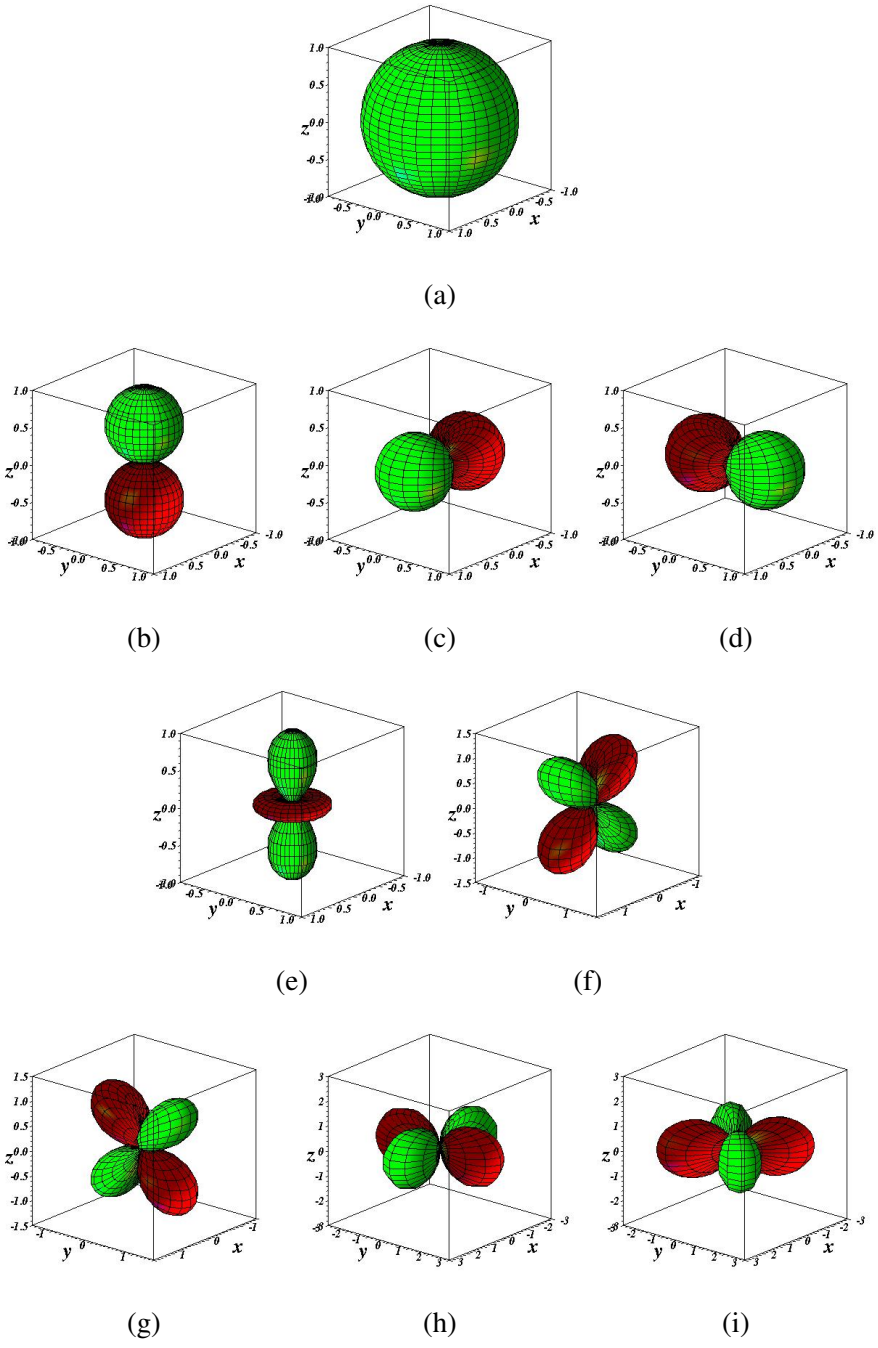

(a)

(b) (c) (d)

(e) (f)

(g) (h) (i)

Figure 2.2: Visualization of the Cartesian Tensor expansion of f. Displayed are $f_0, \mathbf{f}_1,$, and $\underline{\underline{\mathbf{f}}}_2$. Plotted from relations from ref. [64].

The f_0 term in Eq. (2.37) does not include a velocity vector because f_0 represents the isotropic part of the distribution function. The first order term proportional to $\mathbf{v}$ is $\mathbf{f}_1$, and is associated with the net flows of the system. The second order term is responsible for the

tensor quantites such as anisotropic pressure. These expansions are illustrated in Fig. 2.2.

While the dimensionality of the distribution function is reduced, the number of equations increases to 10 with 1 for the scalar component, 3 for the vector component, and 6 for the tensor component, as shown by the notation in Eq. (2.38).

The truncation of the distribution to the second order is designed to include anisotropic pressure effects but is fairly arbitrary. In fact, the error introduced by the truncation can be approximated and is further elaborated upon in Section 2.2.3. Here, the expansion of the Vlasov equation is presented.

2.1.7 Expanded Vlasov Equation

The 4 terms in the Vlasov equation, i.e. left side of Eq. (2.19), are

$$\text{(i)}\frac{\partial \mathbf{f}}{\partial t} \qquad \text{(ii)} \ +\mathbf{v}\cdot\nabla_{\mathbf{r}}\mathbf{f} \qquad \text{(iii)} \ +\mathbf{a}\cdot\nabla_{\mathbf{v}}\mathbf{f} \qquad \text{(iv)} \ +\mathbf{v}\times\boldsymbol{\omega}\cdot\nabla_{\mathbf{v}}\mathbf{f} \tag{2.39}$$

where $\mathbf{a} = e\mathbf{E}/m_e$ and $\boldsymbol{\omega} = e\mathbf{B}/m_e$ are the acceleration due to the electric field and the cyclotron frequency due to the magnetic field, respectively.

Plugging Eq. (2.48) into the Vlasov equation from Eq. (2.39) yields

(i)

$$\frac{\partial \mathbf{f}}{\partial t} = \frac{\partial f_0}{\partial t} + \frac{\partial}{\partial t} f_{1i}\cos\theta_i + \frac{\partial}{\partial t} f_{2ij}\cos\theta_i\cos\theta_j, \tag{2.40}$$

(ii)

$$\mathbf{v}\cdot\nabla_{\mathbf{r}}\mathbf{f} = v\cos\theta_i\left[\frac{\partial f_0}{\partial r_i} + \frac{\partial f_{1i}}{\partial r_i}\cos\theta_i + \frac{\partial f_{2ij}}{\partial r_i}\cos\theta_i\cos\theta_j\right], \tag{2.41}$$

(iii)

$$\mathbf{a} \cdot \nabla_{\mathbf{v}} \mathbf{f} = a_i \cos\theta_i \frac{\partial f_0}{\partial v} + \frac{a_i f_{1i}}{v} + \frac{f_{2ij}}{v}\left(a_i \cos\theta_j + a_j \cos\theta_i\right) + v\left[a_i \cos^2\theta_i \frac{\partial}{\partial v}\left(\frac{f_{1i}}{v}\right)\right] + v^2\left[a_i \cos^2\theta_i \cos\theta_j \frac{\partial}{\partial v}\left(\frac{f_{2ij}}{v^2}\right)\right], \tag{2.42}$$

(iv)

$$\mathbf{v} \times \boldsymbol{\omega} \cdot \nabla_{\mathbf{v}} \mathbf{f} = f_{1k} \frac{\epsilon_{ijk} \{\boldsymbol{\omega}\}_j \cos^2\theta_i}{\cos\theta_k}, \tag{2.43}$$

where

$$\epsilon_{ijk} = \begin{cases} 1 & \text{, if } i,j,k \text{ are all different and } ijk \text{ is an even permutation,} \\ -1 & \text{, if } i,j,k \text{ are all different and } ijk \text{ is an odd permutation,} \\ 0 & \text{, if } i,j,k \text{ are not all different,} \end{cases}$$

is the Cevi-Levita tensor. The time evolution of the various components of $\mathbf{f}$ can be found by integrating over the solid angle, $d^2\Omega$. For all even integers p, q, r, the integral over the solid angle becomes

$$\int \cos^p\theta_i \cos^q\theta_j \cos^r\theta_k d^2\Omega = 4\pi \frac{1\cdot 3\cdot \ldots \cdot (p-1)\cdot 1\cdot 3\cdot \ldots \cdot (q-1)\cdot 1\cdot 3\cdot \ldots \cdot (r-1)}{1\cdot 3\cdot 5\cdot \ldots \cdot (p+q+r+1)}. \tag{2.44}$$

The integral is 0 if any of p, q, r are odd. The m^{th} moment of the VFP equation (Eq. (2.19)) in velocity unit vectors $\{\hat{\mathbf{v}}^m\}$ is given by

$$\int d\Omega \, \{\hat{\mathbf{v}}^m\} \left(\left[\frac{\partial}{\partial t} + \mathbf{v} \cdot \nabla_r - \frac{e}{m_e}(\mathbf{E} + \mathbf{v} \times \mathbf{B}) \cdot \nabla_v \right] f(t, \mathbf{r}, \mathbf{v}) = \frac{\delta \mathbf{f}_c}{\delta t} \right), \tag{2.45}$$

and the $m = 0, 1, 2$ moments are

m=0

$$4\pi \left[\frac{\partial f_0}{\partial t} + \frac{v}{3}\frac{\partial f_{1i}}{\partial r_i} + \frac{a_i f_{1i}}{v} + \frac{v}{3} a_i \frac{\partial}{\partial v}\frac{f_{1i}}{v} = C_0 \right], \tag{2.46}$$

m=1

$$\frac{4\pi}{3}\left[\frac{\partial f_{1i}}{\partial t} + v\frac{\partial f_0}{\partial r_i} + v\frac{\partial f_{2ij}}{\partial r_j} + a_i \frac{\partial f_0}{\partial v} + \frac{2 f_{2ij} a_j}{v} + \frac{2}{5} a_j v^2 \frac{\partial}{\partial v}\left(\frac{f_{2ij}}{v^2}\right) + \epsilon_{ijk}\{\omega\} f_{1k} = C_{1i} \right], \tag{2.47}$$

m=2

$$\begin{aligned} \frac{8\pi}{15}\Bigg[& \frac{\partial f_{2ij}}{\partial t} + \frac{5}{2}\delta_{ij}\frac{\partial f_0}{\partial t} + \frac{v}{2}\frac{\partial f_{1k}}{\partial r_k}\delta_{ij} + \frac{v}{2}\left(\frac{\partial f_{1i}}{\partial r_j} + \frac{\partial f_{1j}}{\partial r_i}\right) + a_i \frac{\partial f_{1j}}{\partial v} + \frac{5}{2}\delta_{ij}\frac{f_{1k} a_k}{v} \\ & + \frac{v}{2}\left[a_k \frac{\partial}{\partial v}\left(\frac{f_{1k}}{v}\right)\delta_{ij} + a_i \frac{\partial}{\partial v}\left(\frac{f_{1j}}{v}\right) + a_j \frac{\partial}{\partial v}\left(\frac{f_{1i}}{v}\right)\right] \\ & + \frac{\{\omega\}_k}{2}\left[\epsilon_{ikn}\left(f_{2nj} + f_{2jn}\right) + \epsilon_{jkn}\left(f_{2ni} + f_{2in}\right)\right] \Bigg] = C_{2ij} + \frac{5}{2}\delta_{ij} C_0. \end{aligned} \tag{2.48}$$

Henceforth, Eqs. (2.46) to (2.48) will be known as the f_0, f_1 and f_2 equation, respectively. These 10 equations govern the time evolution of the expanded distribution function.

2.2 Transport Processes

Equations (2.46) and (2.47) in vector form are

$$\frac{\partial f_0}{\partial t} + \frac{v}{3}\frac{\partial}{\partial \mathbf{x}} \cdot \mathbf{f}_1 + \frac{1}{3v^2}\frac{\partial}{\partial v}(v^2 \mathbf{a} \cdot \mathbf{f}_1) = C_0, \tag{2.49}$$

$$\frac{\partial \mathbf{f}_1}{\partial t} + v\nabla f_0 + \mathbf{a}\frac{\partial f_0}{\partial v} + \boldsymbol{\omega} \times \mathbf{f}_1 + \frac{2}{5} v \, \nabla \cdot \underline{\underline{\mathbf{f}}}_2 + \frac{2}{5v^3}\frac{\partial}{\partial v}\left(v^3 \mathbf{a} \cdot \underline{\underline{\mathbf{f}}}_2\right) = \mathbf{C}_1. \tag{2.50}$$

These can be used to derive the fluid equations instead of the full VFP equation from Eq. (2.19). The velocity moment integrals for $f_0, \mathbf{f}_1$, and $\underline{\underline{\mathbf{f}}}_2$ are

$$\langle v^m \rangle = \frac{4\pi}{n_e} \int_0^\infty v^{2+m} \, f_0 \, dv, \tag{2.51}$$

$$\langle \mathbf{v} v^m \rangle = \frac{4\pi}{3n_e} \int_0^\infty v^{2+m} \, \mathbf{v}\mathbf{f}_1 \, dv, \tag{2.52}$$

$$\langle \mathbf{v}\mathbf{v} v^m \rangle = \frac{8\pi}{15n_e} \int_0^\infty v^{2+m} \, \mathbf{v}\mathbf{v}\underline{\underline{\mathbf{f}}}_2 \, dv, \tag{2.53}$$

Using these, the macroscopic quantities from the expanded distribution function are

$$n_e = n_e \langle v^0 \rangle = 4\pi \int_0^\infty v^2 f_0 \, dv, , \tag{2.54}$$

$$U_e = \frac{1}{2} n_e m_e \langle v^2 \rangle = 4\pi \int_0^\infty \frac{1}{2} m_e v^2 \, v^2 f_0 \, dv, \tag{2.55}$$

$$k_B T_e = \frac{2}{3} \frac{U_e}{n_e} = \frac{m_e \langle v^2 \rangle}{3 \langle v^0 \rangle}, \tag{2.56}$$

$$\mathbf{j} = -e n_e \langle \mathbf{v} v^0 \rangle = -\frac{4\pi e}{3} \int_0^\infty v^2 \mathbf{v}\mathbf{f}_1 \, dv, \tag{2.57}$$

$$\mathbf{q} = \frac{1}{2} n_e m_e \langle \mathbf{v} v^2 \rangle = \frac{4\pi}{3} \int_0^\infty \frac{1}{2} m_e v^2 \, v^2 \mathbf{v}\mathbf{f}_1 \, dv, \tag{2.58}$$

$$\underline{\underline{\mathbf{P}}} = n_e m_e \langle \mathbf{v}\mathbf{v} v^0 \rangle = \frac{8\pi}{15} \int_0^\infty v^2 \mathbf{v}\mathbf{v}\underline{\underline{\mathbf{f}}}_2 \, dv. \tag{2.59}$$

The $m = 0, 2$ moments of the f_0 equation are

$$\frac{\partial n_e}{\partial t} + \nabla \cdot \frac{\mathbf{j}}{e} = 0, \tag{2.60}$$

$$\frac{\partial U_e}{\partial t} + \nabla \cdot \mathbf{q} + \mathbf{j} \cdot \mathbf{E} = 0, \tag{2.61}$$

and provide the relations for conservation of density and energy, respectively.

Relations for $\mathbf{q}$, the heat flow, and $\mathbf{E}$, the electric field, can be derived from the f_1 equation. The heat flow equation comes from the $m = 3$ moment of the distribution function. The relation for $\mathbf{E}$ is called Ohm's law, and is a form of the momentum equation

for the electrons. It is obtained from the $m = 1$ moment of the f_1 equation. Obtaining Ohm's law requires a definition for the collision frequency between electrons and ions, ν_{ei}. The collision frequency must be carefully considered as this sets the relative difference in collisionality for the electrons that comprise a distribution function and determines the *kinetic* behavior of the collisional plasma.

2.2.1 Braginskii Transport

The actual electron-ion collision frequency from a Fokker-Planck expansion is $\nu_{ei} = Y n_i Z^2 / v^3$ [64]. The pair of equations for $\mathbf{E}$ and $\mathbf{q}$ obtained using this are

$$\mathbf{E} + \mathbf{C} \times \mathbf{B} = -\frac{\nabla P_e}{e n_e} + \frac{\mathbf{j}}{e n_e} \times \mathbf{B} + \underline{\underline{\alpha}} \cdot \frac{\mathbf{j}}{e^2 n_e^2} - \underline{\underline{\beta}} \cdot \frac{\nabla T_e}{e} \quad \text{and} \tag{2.62}$$

$$\mathbf{q} = -\underline{\underline{\kappa}} \cdot \nabla T_e - \frac{T_e}{e} \underline{\underline{\beta}} \cdot \mathbf{j}. \tag{2.63}$$

Equations (2.62) and (2.63) are called the transport equations and α, β, and κ are called the transport coefficients that represent resistivity, thermoelectric effect, and the thermal conductivity respectively. $\mathbf{C}$ is the ion flow velocity vector that translates the electric field by a term equal to $\mathbf{C} \times \mathbf{B}$. The transport equations have been calculated in various forms, but those discussed here reference the equations given in Braginskii [44] (hence "Braginksii transport"), and Epperlein & Haines [70]. In these equations, $\tau_B = \tau_{ei} \ 3\sqrt{\pi}/4$.

The transport coefficients are functions of the Hall parameter, $\omega\tau$, and the atomic number, Z. Spitzer and Härm [73] performed one of the earliest and most accurate calculations of the transport coefficients by solving the f_1 equation using a finite difference approach for unmagnetized plasmas (i.e. $\omega\tau = 0$) of varying Z.

Despite the existence of many subsequent sets of transport coefficents, the most popular version remains that of Braginskii [44] because of his two-fluid description of the plasma

and convenient notation, as that in Eqs. (2.62) and (2.63).

It was shown that Braginskii's version was inaccurate over wide ranges of $\omega\tau$ due to the truncation of the expansion of f_1. Seeking to improve upon that calculation, Epperlein and Haines [70] developed a more accurate set of transport coefficients for arbitrary Z and finite $\omega\tau$.

2.2.2 Transport in the Presence of Inverse Bremsstrahlung Heating

Calculating the transport coefficients requires an approximation for the distribution function. Previous transport coefficients in refs. [44, 70] have been calculated with the assumption that f_0 is a Maxwell-Boltzmann distribution of a certain density and thermal velocity, n_e and v_{th}, respectively i.e. $f_0(v) = \pi^{-3/2} n_e v_{\text{th}}^{-3} \exp(-v^2/v_{\text{th}}^2)$.

While this approximation is an excellent one for plasmas near thermal equilibrium, an ICF plasma often involves laser heating and has been shown to result in modifications to the distribution function [74] that may affect thermal energy transport [29].

Laser heating of a plasma at the intensities discussed here occurs by the inverse Bremsstrahlung process. A laser incident upon a plasma creates oscillations in the electrons within the plasma due to the oscillating electric field of the laser. These electrons collide with ions, losing some of their energy and thermalizing. Over time, this results in energy transfer from laser to plasma, and *inverse Bremsstrahlung heating* of the plasma occurs.

Langdon [74] showed that f_0 approaches a characteristic non-Maxwellian distribution in the absence of collisions while significant electron-electron collisions relax the distribution towards a Maxwellian shape. The shape of the distribution between the two limits can be described by a more general Dum-Langdon-Matte (DLM) profile given by

$$f_{\text{sG}}(m) = C(m) \frac{n_e}{v_{\text{th}}^3} \exp\left[-\left(\frac{v}{\alpha_e v_{\text{th}}} \right)^m \right], \tag{2.64}$$

where $\alpha_e = [3\Gamma(3/m)/2\Gamma(5/m)]^{1/2}$ and $C(m) = m/4\pi\alpha_e^3\Gamma(3/m)$ are constants and $\Gamma(Z) = (Z-1)!$ is the gamma function. Setting $m = 2$ retains the Maxwellian distribution while $m = 5$ refers to the limit in case of strong IB heating. These distributions are shown in Fig. 2.3.

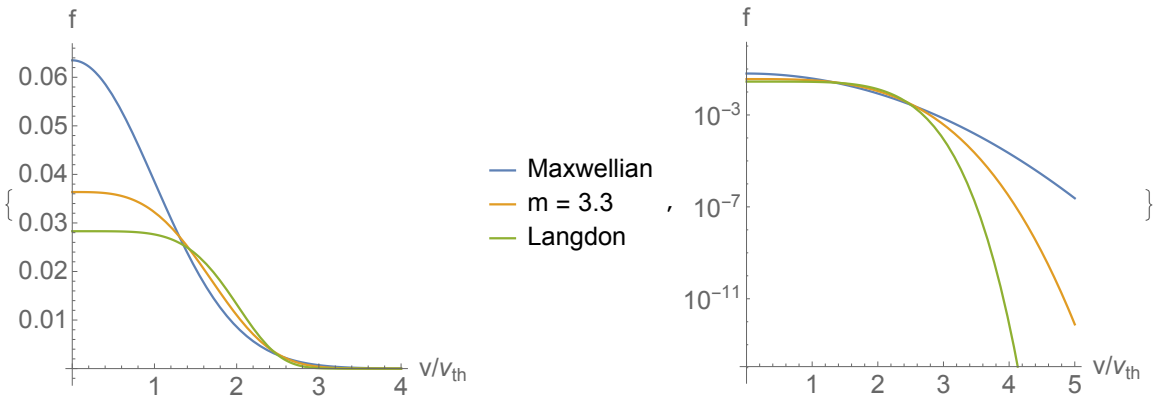

Figure 2.3: The difference between Maxwellian (m=2) and Langdon (m=5) distributions is illustrated. A realistic case of $m = 3.3$ is considered since electron-electron collisions are difficult to ignore over long pulse time-scales.

The relation provided by Matte et al. [29] for approximating m from laser intensity, a function of v_{osc}, is

$$m = 2 + \frac{3}{1 + 1.66/\alpha_M^{0.721}}, \qquad \text{where } \alpha_M = Z\left(\frac{v_{\text{osc}}}{v_{\text{th}}}\right)^2. \tag{2.65}$$

Measurements of the relaxation of the heat flow performed using Langmuir probes allowed computation of the velocity distribution function that showed these features [75, 76]. An improved set of transport coefficients that includes the effects of these distorted distribution functions has been published, but only for a Lorentz plasma [65, 77] and the effects of the modified transport coefficients are described in ref. [78]. They are a function of $\omega\tau$ and m but not Z since they were computed in the Lorentz limit ($Z \to \infty$). The new transport

equations are

$$\mathbf{E} + \mathbf{C} \times \mathbf{B} = -\underline{\underline{\gamma}} \cdot \frac{\nabla P_e}{e n_e} + \frac{\mathbf{j}}{e n_e} \times \mathbf{B} + \underline{\underline{\alpha}} \cdot \frac{\mathbf{j}}{e^2 n_e^2} - \underline{\underline{\psi}} \cdot \frac{\nabla T_e}{e} \tag{2.66}$$

$$\text{and } \mathbf{q} = -\underline{\underline{\kappa}} \cdot \nabla T_e - \frac{T_e}{e} \underline{\underline{\psi}}' \cdot \mathbf{j} - \underline{\underline{\phi}} \cdot \nabla P_e, \tag{2.67}$$

where $\underline{\underline{\psi}}' = \underline{\underline{\psi}} + 5/2\underline{\underline{\mathbb{I}}}$ and $\mathbf{C}$ is the ion flow velocity.

These transport coefficients have been implemented in fluid modeling [79] relevant to hohlraums and comparisons showed that the modified transport coefficients compared well with the simulations performed without the use of a flux-limiter for the heat flow. The use of a flux-limiter was proposed for those simulations because of the suppressed heat flow from the DLM distributions [80] discussed here. While flux-limited heat flow can be relevant to non-Maxwellian distributions such as those caused by laser heating, it is mainly used in the context of non-local heat flow.

2.2.3 Non-Local Transport

Equation (2.63) describes a method to calculate the thermal energy flow in a plasma from temperature gradients and electron currents. Quantifying the heat flow closes the electron energy conservation equation because $\nabla \cdot \mathbf{q}$ describes the net thermal energy added. The first term of Eq. (2.63) gives $\mathbf{q} = \kappa \nabla T_e$. The evolution of the temperature due to the heat flow is then given by

$$\begin{aligned} \frac{\partial T_e}{\partial t} &= \nabla \cdot \mathbf{q} \\ &= \nabla \cdot (-\kappa \nabla T_e) \\ &= -\kappa \nabla^2 T_e, \end{aligned} \tag{2.68}$$

where κ represents a coefficient for direct proportionality between $\mathbf{q}$ and ∇T_e. The above shows that the heat flow in Braginskii transport incorporates the diffusive approximation.

The assumption that the heat flow can be described by diffusive transport is subject to breakdown. Arising as a consequence of the random walk problem, diffusion inherently requires many opportunities for the particles to change direction while they travel down the gradient. Therefore, diffusive transport is *local* such that the heat flow is described by a local gradient in temperature. In collisional transport, the direction changes occur due to collisions and *non-local transport* in this context refers to the case where the particles that do not collide as frequently as others travel to regions farther downstream from the gradient and deposit energy non-locally.

For collisional diffusion to remain valid, the collisional mean-free-path, λ_{ei}, has to be significantly smaller than the scale length of the gradient, L. Heat flow is carried by electrons with speeds of approximately three to four times the thermal velocity [80] and therefore having 81 to 256 times the mean-free-path. Let

$$L_T = \left| \frac{T_e}{\nabla T_e} \right| \tag{2.69}$$

be the temperature scale length. Since those electrons responsible for the heat flow will travel farther by a factor of nearly 200 than those at the thermal velocity, plasmas with $L_T \approx 200\lambda_{ei}$ will have some electrons that travel past the gradient and invalidate the diffusion approximation. While the plasma remains quasi-neutral due to an equal exchange of charge, the difference in energy exchanged results in increased heat flow farther away and decreased heat flow near the gradient [81, 82]. Non-local heat flow has been shown to exist in situations where $L_T \sim 100\lambda_{ei}$ [32, 83] while theory predicts the influence of non-local heat flow to occur when $L_T \lesssim (Z+1)^{1/2}\ 10^3\ \lambda_{ei}$ [84].

Figure 2.4 provides a convenient illustration of this effect in an implosion environment

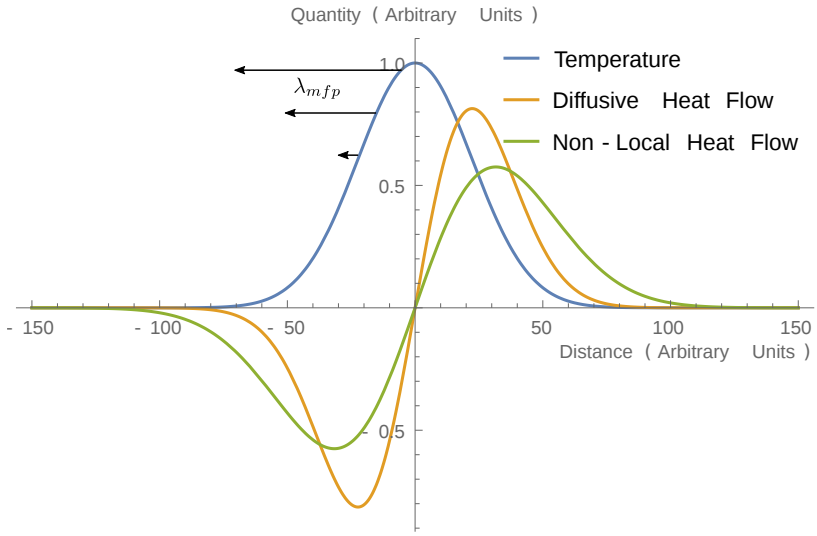

Figure 2.4: An arbitrary temperature profile that is subject to non-local effects is plotted. The diffusive heat flux is computed by calculating the gradient of the temperature. The non-local heat flow, due to its nature, is wider but smaller in peak amplitude. The arrows represent the mean free path of the heat flow carrying electrons. The electrons from the hotter region travel farther and result in a more spread out heat flow. (Note: Non-local heat flow has been approximated and is not self-consistent in this image).

[85]. The diffusive heat flux would require the presence of a temperature gradient. In the case of very steep gradients (i.e. very small L), the higher velocity electrons from the hot part of the gradient travel farther than the extent of the gradient, and therefore, carry thermal energy to a non-local region. Since they no longer deposit energy near the gradient, there is local heat flow inhibition.

This effect has received a variety of treatments for inclusion in modeling. The most rudimentary of these is the use of a flux limiter that is a fraction of the free streaming heat flux $q_{FS} = n_e k_B T_e v_{th}$. So a flux limited heat flow is

$$q_f = f n_e k_B T_e v_{th}, \tag{2.70}$$

where f is an empirical constant that varies from $0.03 - 0.15$ for different experiments [32, 30, 23, 31, 34, 39, 40]. In the simplest flux limited implementations, the heat flow is set to the maximum of the diffusive heat flow and q_f while others may employ reciprocal

weighting or similar techniques.

A more sophisticated approach was pioneered by Luciani, Mora, and Virmont (LMV) [86] and has since been discussed in detail [84], and expanded to 2D [35] and magnetized plasmas [36]. The Schurtz-Nicolai-Busquet (SNB) model [35, 36] is widely used at the present time and has been implemented for modeling of experiments in refs. [34, 37, 87, 7], to name a few. In the LMV method, the heat flux is described by

$$q(x) = \int q_{SH}(x')w(x,x')dx', \tag{2.71}$$

where q_{SH} is the Spitzer-Harm heat flow [73] and $w(x,x')$ is a delocalization kernel given by

$$w(x,x') = \frac{1}{2\lambda(x')} \exp\left(-\frac{X}{\lambda(x')}\right), \tag{2.72}$$

where, X, a quantity analogous to optical depth, is

$$X = \frac{1}{n_e(x')} \left| \int_x^{x'} dx'' n_e(x'') \right|, \tag{2.73}$$

and $\lambda(x')$ is an effective range for electrons of temperature $T_e(x')$. $\lambda(x')$ can be given in terms of the mean-free-path λ_{mfp} by

$$\lambda(x') \approx 30\sqrt{Z+1} \quad \lambda_{\text{mfp}}(x'). \tag{2.74}$$

This method retrieves the Spitzer-Harm heat flow in the presence of gentle gradients. For situations where the mean free path of is comparable to the temperature gradient, the heat flow calculated by direct integration of Eq. (2.71) is $0.1 - 0.2\ q_{FS}$. Additionally, since the heat flux predicted at position x depends on a surrounding region of size approximately 2λ, which, from Eq. (2.74), is much larger than the collisional mean-free-path, some non-local

effects are included by definition.

In the previous sections on the transport equations given by Braginskii as well as those by Ridgers et al., the assumption regarding the shape of the distribution function has persisted. In the discussion on non-local transport, it was determined that the diffusive approximation can be invalid in certain settings and analytical models to treat non-local heat flow use a Maxwell-Boltzmann distribution function. In order to circumvent both issues, Ohm's law and the heat flow relation can be rewritten as functions of the moments of an arbitrarily shaped distribution function.

2.2.4 Generalized Ohm's law

The VFP equation for $\mathbf{f}_1$, Eq. (2.50), with the Lorentz approximation for the collision frequency is

$$\frac{\partial \mathbf{f}_1}{\partial t} + v\nabla f_0 + \mathbf{a}\frac{\partial f_0}{\partial v} + \boldsymbol{\omega} \times \mathbf{f}_1 + \frac{2}{5} v \, \nabla \cdot \underline{\underline{\mathbf{f}}}_2 + \frac{2}{5v^3}\frac{\partial}{\partial v}\left(v^3 \mathbf{a} \cdot \underline{\underline{\mathbf{f}}}_2\right) = -\frac{Z^2 n_i}{v^3}\mathbf{f}_1. \quad (2.75)$$

Obtaining a generalized version of Ohm's law that applies to an arbitrary distribution function requires a relation for a term that reduces to the Spitzer resistivity in the form $\eta\mathbf{j}$. Because of the v^{-3} dependence, the appropriate moment of the Eq. (2.50) is

$$\frac{4\pi}{3n_e} e \int_0^\infty v^6 dv \left(\frac{\partial \mathbf{f}_1}{\partial t} + v\nabla f_0 - \mathbf{a}\frac{\partial f_0}{\partial v} - \boldsymbol{\omega} \times \mathbf{f}_1 + \frac{2}{5} v \nabla \cdot \underline{\underline{\mathbf{f}}}_2 = \frac{Y n_i Z^2}{v^3}\mathbf{f}_1\right), \quad (2.76)$$

and solving for the electric field yields the generalized Ohm's law given by

$$\mathbf{E} = -\frac{\nabla\left(n_e m_e \langle v^5 \rangle\right)}{6 e n_e \langle v^3 \rangle} - \frac{\nabla \cdot \left(n_e m_e \langle \mathbf{v}\mathbf{v} v^3 \rangle\right)}{2 e n_e \langle v^3 \rangle} + \boldsymbol{\omega} \times \frac{\langle \mathbf{v} v^3 \rangle}{2 e n_e \langle v^3 \rangle} + \overline{\eta}\mathbf{j} + \frac{\partial \langle \mathbf{v} v^3 \rangle}{\partial t}, \quad (2.77)$$

where $\bar{\eta}$ is the effective resistivity given by

$$\bar{\eta} = \frac{2\pi Z e^2 \ln \Lambda_e i}{(4\pi\epsilon_0)^2 m_e \langle v^3 \rangle}. \tag{2.78}$$

The first two terms in Eq. (2.77) are representative of the pressure tensor. The third term governs the relationship between the flow of charged particles and the magnetic field. The fourth term represents resistive effects and the last is the inertial term.

The three relevant transport theories in this thesis have been presented. The heat flow in the generalized theory is simply calculated using Eq. (2.58) and the main differences induced by this calculation are discussed in Section 2.2.3. In what follows, the magnetic field and heat flow phenomena that arise from classical and super-Gaussian transport are compared with the transport from generalized theory by analysis of the different terms in the three Ohm's laws.

2.3 Magnetic Field Phenomenon

The transport coefficients are tensor quantities that depend on the direction with respect to the magnetic field. The direction of the magnetic field provides an axis of orientation as well as an independent direction of transport since electron behavior parallel to a magnetic field is unaffected. The transport coefficient tensors obey

$$\underline{\underline{\mathbf{\Psi}}} \cdot \mathbf{s} = \Psi_{\parallel}\, \mathbf{b}(\mathbf{b} \cdot \mathbf{s}) + \Psi_{\perp}\, \mathbf{b} \times \mathbf{s} \times \mathbf{b} + \Psi_{\wedge}\, \mathbf{b} \times \mathbf{s}, \tag{2.79}$$

where $\mathbf{s}$ is the force in question, and ψ is an arbitrary tensor quantity. These directions are illustrated in Fig. 2.5.

Applying Faraday's law to Ohm's law gives an equation governing the evolution of the macroscopic magnetic field. The following subsections discuss how each term contributes

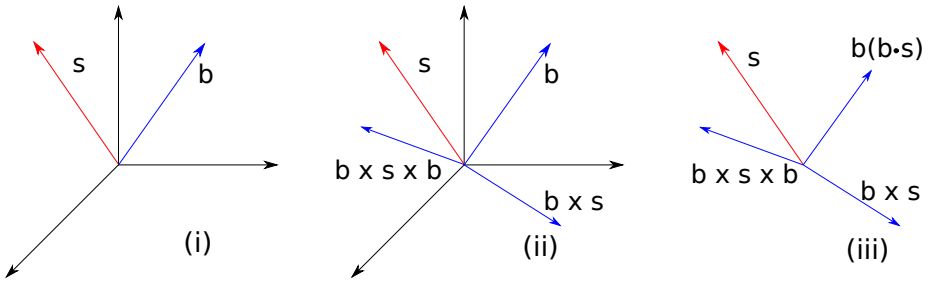

Figure 2.5: The different directions of the transport coefficients in Cartesian Coordinates can be understood by the three diagrams. (i) $\mathbf{s}$ is the driving force and $\mathbf{b}$ is the magnetic field direction. (ii) The two directions orthogonal to $\mathbf{b}$ are $\mathbf{b} \times \mathbf{s}$ and $\mathbf{b} \times \mathbf{s} \times \mathbf{b}$. (iii) The vector in the $\mathbf{b}$ direction is rescaled to $\mathbf{b}(\mathbf{b} \cdot \mathbf{s})$.

to magnetic field evolution and highlights the differences between the three formulations of Ohm's law provided above.

2.3.1 Frozen-in-Flow

Applying Faraday's law to the electric field supported by the moving ion fluid yields

$$\left[\frac{\partial \mathbf{B}}{\partial t}\right]_{\mathbf{C}} = \nabla \times (\mathbf{C} \times \mathbf{B}) \,. \tag{2.80}$$

Using vector identities, this part of the induction equation becomes

$$\frac{\partial \mathbf{B}}{\partial t} = -\mathbf{B}(\nabla \cdot \mathbf{C}) + (\mathbf{B} \cdot \nabla)\mathbf{C} - (\mathbf{C} \cdot \nabla)\mathbf{B} \tag{2.81}$$

and indicates two physical effects. The first term on the right side indicates the change in magnetic field induced by the compression and rarefaction of the ions due to gradients in their velocity. The next two terms indicate the convection of the magnetic field with the bulk flow. For this reason, the $\mathbf{C} \times \mathbf{B}$ term describes the magnetic field in situations of "frozen-in-flow" because the magnetic field is effectively "frozen" to the bulk plasma flow.

2.3.2 Magnetic Field Generation

The term in Ohm's law that is proportional to the gradient in electron pressure describes the electric field that arises as a result of charge separation induced by the difference in electron pressures at a certain point. The magnetic fields that can be self-generated in a plasma arise from the mechanism described by this term in Ohm's law. Called the Biermann battery effect [88], this mechanism is described by

$$\left[\frac{\partial \mathbf{B}}{\partial t}\right]_{\text{BB}} = -\nabla \times \frac{\nabla P_e}{e n_e} = -\frac{\nabla T_e \times \nabla n_e}{e n_e}, \tag{2.82}$$

Note that this term does not arise from a collisional dependence as it is present in a collisionless Ohm's law as well [25]. Therefore, this mechanism is not only applicable in semi-collisional plasmas as discussed here but also in astrophysical settings where mean-free-paths are very long and the plasmas are effectively collisionless. The Biermann battery effect has been proposed as magnetic field generation mechanism for seed magnetic fields that are amplified by turbulent mechanisms [89].

While Braginskii's version of Ohm's law does not carry a coefficient modifying the pressure gradient, Ridgers et al. show that this term is modified by a new transport coefficient, γ, that decreases as the distribution function is further distorted meaning that the field generation rate decreases for DLM distributions of increasing magnitude. In the generalized Ohm's law, the pressure gradient comes from the term with the gradient of the 5$^{\text{th}}$ moment of f_0 in Eq. (2.77). Applying Faraday's law yields

$$\left[\frac{\partial \mathbf{B}}{\partial t}\right]_{\text{G-O}} = -\nabla \times \frac{\nabla n_e m_e \langle v^5 \rangle}{6 e n_e \langle v^3 \rangle} = \frac{\nabla (n_e \langle v^5 \rangle) \times \nabla (n_e \langle v^3 \rangle)}{6 (n_e \langle v^3 \rangle)^2}. \tag{2.83}$$

The moment formulation captures the modifications to the distribution function and self-consistently includes the induced changes in the field generation rate. Due to the depen-

dence on a higher order moment of the distribution function than the pressure moment, the generalized Ohm's law allows field generation through non-local effects where no density gradients are present [90].

Note that since the derivation for classical transport sets $\underline{\underline{\mathbf{f}}}_2 = 0$, there is no anisotropic contribution to the pressure gradient. However, the electric field that supported by the off-diagonal terms in the pressure tensor have been shown to be important in collisionless settings where magnetic reconnection may occur [91, 55]. In that case, the electric field in the diffusion region where the flows diverge is described by the divergence of the pressure tensor $\nabla \cdot \underline{\underline{\mathbf{P}}}$. In Chapter 6, the application of electric field that comes from the anisotropic pressure term is extended to semi-collisional plasmas. It has also been shown that the the off-diagonal terms can lead to magnetic field generation near laser speckles [92].

2.3.3 Hall Effect

The second term,

$$\mathbf{E}_{\text{Hall}} = \frac{\mathbf{j}}{en_e} \times \mathbf{B} \tag{2.84}$$

is called the Hall term and represents the force felt by the moving charged particles from a magnetic field. This term is identical in all three versions of Ohm's law. It can be obtained from Eq. (2.77) by letting the velocity $\langle \mathbf{v}v^3 \rangle / 2en_e \langle v^3 \rangle = \mathbf{v}_N + \mathbf{j}/en_e$ and consequently, creating a new term proportional to $\mathbf{v}_N \times \mathbf{B}$ that will be discussed in Section 2.3.5.

The Hall term has the same form as that of the frozen-in-flow term and therefore, the magnetic field may also transported by the Hall term. On length scales smaller than the ion skin depth, $\delta_i = c/\omega_{pi}$, the electrons and ions decouple and the electron fluid needs to be treated as a separate species. Over such small scales, the Hall term becomes prevalent in comparison to $\mathbf{C} \times \mathbf{B}$ and results in transport of magnetic field due to the flow of electrons. Much like the collisionless pressure tensor, the Hall term is also a part of the collisionless

Ohm's law. In fact, Hall transport of magnetic field is a significant effect in astrophysical magnetic reconnection scenarios [93, 94, 95, 96, 91, 55].

2.3.4 Resistive Diffusion

The influence of the resistivity term, $1/e^2 n_e^2 \ \underline{\underline{\alpha}} \cdot \mathbf{j}$, on the magnetic field evolution can be shown by considering the matrix form of the resistivity in the case of a magnetic field in the $\hat{z}$ direction.

$$\nabla \times \left(\underline{\underline{\alpha}} \cdot \mathbf{j}\right) = \nabla \times \begin{bmatrix} \alpha_\perp & -\alpha_\wedge & 0 \\ \alpha_\wedge & \alpha_\perp & 0 \\ 0 & 0 & \alpha_\parallel \end{bmatrix} \begin{bmatrix} j_x \\ j_y \\ j_z \end{bmatrix} = \nabla \times \begin{bmatrix} \alpha_\perp j_x - \alpha_\wedge j_y \\ -\alpha_\perp j_y + \alpha_\wedge j_x \\ \alpha_\parallel j_z \end{bmatrix} \tag{2.85}$$

$$= \left(\nabla \cdot \frac{\alpha_\perp}{\mu_0} \nabla \mathbf{B} + \alpha_\wedge \nabla \times \mathbf{j} \times \mathbf{B} \right) \tag{2.86}$$

where Ampere's Law, $\nabla \times \mathbf{B} = \mu_0 \mathbf{j}$, is used. The first term in Eq. (2.86) describes resistive diffusion of the magnetic field due to flow in the $\mathbf{b} \times \mathbf{s} \times \mathbf{b}$ direction. The second term results in a correction to the Hall effect proportional to $\alpha_\wedge$.

2.3.5 Nernst Effect

A similar procedure for the thermoelectric coefficient produces

$$\nabla \times \frac{1}{e} (\underline{\underline{\beta}} \cdot \nabla T_e) = \left(\nabla \times \mathbf{v}_\beta \times \mathbf{B} \right), \tag{2.87}$$

where $\mathbf{v}_\beta = \beta_\wedge \nabla T_e / e$ is a characteristic velocity associated with this effect. The influence of $\beta_\perp$ is removed because the curl of the temperature gradient is 0. The result is a field advection equation, much like frozen-in-flux, but one where the magnetic field is carried by a characteristic electron velocity $\mathbf{v}_\beta$ that depends on the temperature gradient. After

performing a procedure similar to that required to obtain Eq. (2.77), but for a collisional dependence of v^{-2}, Haines showed that $\mathbf{v}_\beta$ is related to the Nernst velocity by

$$\mathbf{v}_N \approx \mathbf{v}_\beta \approx \frac{\mathbf{q}_e}{5/2 P_e}. \tag{2.88}$$

and applied it in different contexts [97]. Modeling has shown magnetic field compression in implosion plasmas [98, 99] along with convection in overdense plasmas [99, 100] and underdense gas jets [101]. Fast magnetic field convection of self-generated fields into overdense plasma [102, 87] has been experimentally demonstrated and attributed to the Nernst effect. The Nernst effect has also been included in modeling ICF experiments relevant to Thomson scattering in hohlraums [41], Rayleigh-Taylor instability in direct-drive [103], and MagLIF [104].

It is easy to see from Eq. (2.88) that the breakdown of diffusive transport that affects heat flow will also be relevant for the Nernst flow [105], and that the Nernst velocity may require the use of techniques discussed in Section 2.2.3. The modified transport coefficients presented by Ridgers et al. include an additional coefficient γ for the thermoelectric term that is then shown to suppress the Nernst velocity [78].

Non-local and super-Gaussian effects for the Nernst velocity are self-consistently included in the corresponding term in generalized Ohm's law given by

$$\mathbf{v}_N = \frac{\langle \mathbf{v} v^3 \rangle}{2 e n_e \langle v^3 \rangle} - \frac{\mathbf{j}}{e n_e}. \tag{2.89}$$

The approximation in Eq. (2.88) suggests that the Nernst effect represents magnetic field transport by the heat flow carrying electron population. The exact formulation in Eq. (2.89) confirms this interpretation and suggests that there is a slightly larger influence of the higher velocity electrons because of the higher order velocity moment that is required.

The Nernst effect in plasma can be qualitatively described by the following; since the faster, "hot", population of electrons are essentially collisionless, the magnetic field is "frozen" to them, whereas the slower and more collisional portion of the distribution function is able to diffuse across field lines. Hence, magnetic fields can be advected with close to zero net current by "hot" electrons.

Dimensionless numbers that compare the ratio of the magnitudes of the Nernst term in Ohm's law to the bulk plasma flow, $R_N \gg 1$ [101], and to the Hall term[1], $H_N \gg 1$ [106], suggest that Nernst convection may be the dominant mechanism for magnetic field transport in a hohlraum.

The kinetic formulation that is required to have a self-consistent treatment of the various effects in Ohm's law and heat flow has been described in Section 2.1. This is implemented in a code known as IMPACTA and is described in the following chapter.

[1]The scaling for H_N is obtained and discussed in Chapter 6

CHAPTER 3

IMPACTA

To best model these nanosecond, small gradient scale length, hot plasmas, the code IMPACTA has been developed. The code solves the Cartesian expanded VFP equation for the electrons using an implicit scheme, with non-linear terms such as $\mathbf{E}f_0$ treated by iteration of the matrix solution. The algorithm used for solving the matrix equation is a routine from the *Portable, Extensible Toolkit for Scientific Computation* (PETSc) [107, 108, 109]. It is an evolution of the code IMPACT [110], with a number of additions to the model. Most notably, the expansion of the distribution, which in IMPACT is truncated after first order, has been expanded to include second order ($\underline{\underline{\mathbf{f}}}_2$) terms and magnetic fields in the plane have been added. The code is Eulerian with 2D Cartesian spatial geometry. It uses an implicit finite difference algorithm to solve the components of the expanded VFP equation, in addition to the Faraday and the Ampère-Maxwell equations for the fields. Note that this is another slight difference compared with IMPACT, where the magnetic field is calculated explicitly. IMPACTA currently uses the Lorentz approximation (valid for high Z), whereby electron-electron (e-e) collisions are neglected in the equation for f_1. A scaling law proposed by Epperlein and Short [111] is used to scale the e-i collision frequency such that it replicates the contribution to the momentum transport from e-e collisions when low Z plasmas are modeled[1]. The term for electron-ion (e-i) scattering is retained in all equations

[1]This is further described in Appendix A

in the reduced form where it is $\propto 1/v^3$. The neutralizing ion background is mobile, via the hydrodynamic model introduced in [101], and includes the effect of the full pressure tensor in updating the ion velocity. The laser-heating is performed with an inverse bremsstrahlung heating model based on Langdon's operator.

IMPACTA has been shown to reproduce classical transport in the appropriate limits i.e. when the distribution function is a Maxwellian in the presence of very long length scale plasmas with respect to the collisional mean free path [110]. It has also been used to discover kinetic effects such as non-local magnetic field generation [90] or anisotropic pressure driven field generation [92]. The use of IMPACTA here is dictated by the ability to study generalized transport theory for nanosecond time-scale, magnetized, collisional, and hot plasmas, especially in the context of hohlraums. The dynamic heating profile created by the 192 beams involved in a NIF hohlraum shot is replicated here by calculating the propagation of different beams by use of the ray tracing equations.

3.1 Normalization and Equations

The particles in IMPACTA are described by finite differenced distribution of electrons coupled to a cold ion fluid at each point on a 2D grid. Each term in the Cartesian tensor expansion of the electron distribution function [71, 72] is a function of speed and $\hat{v} = \hat{x}\sin\theta\cos\phi + \hat{y}\sin\theta\sin\phi + \hat{z}\cos\theta$ is the velocity unit vector, expressed relative to the ion fluid velocity $\mathbf{C}$, so that the laboratory frame velocity $\mathbf{v}_{\rm lab} = \mathbf{v} + \mathbf{C}$.

The normalization scheme is dictated by normalizing quantities with respect to characteristic values for a 'reference material' with electron temperature T_{e0}, ion number density n_{i0}, ionization number Z_0 and electron number density $n_{e0} = Z_0 n_{i0}$. Velocity is normalized to the electron thermal speed corresponding to T_{e0} defined as $v_n = \sqrt{2k_B T_{e0}/m_e}$, time is normalized to the electron-ion 90^o scattering time $\tau_n = v_n^3/(Y\, Z_0^2 n_{i0} \ln\lambda_{ei0})$ for a thermal

electron moving through the reference material and length is normalized to the thermal e–i mean-free-path which is $\lambda_n = v_n\,\tau_n$. The collisionless skin depth δ_c appearing in Ampère-Maxwells' equation is that for a plasma density of n_{e0}. The full set of normalizations is $\tilde{v} = v/v_n$, $\tilde{t} = t/\tau_n$, $\tilde{x} = x/\lambda_n$, $\tilde{\nabla} = \lambda_n\,\nabla$, etc., $\tilde{f}_p = f_p/(n_{eo}\,v_n^3)$, $\tilde{E} = (eE/m_e)/(\lambda_n\tau_n^{-2})$, $\tilde{\omega} = (e\,B/m_e)\tau_n$, $\tilde{Z} = Z/Z_0$, and $\tilde{n}_e = n_e/n_{eo}$. For the other macroscopic quantities one gets $\tilde{j} = j/(e\,n_{e0}\,v_n)$, $\tilde{q} = q/(m_e v_n^3\,n_{e0})$, $\tilde{U} = U_e/(m_e v_n^2\,n_{e0})$, and $\tilde{T} = T_e/T_{e0}$. Note that the normalization in IMPACTA differs from IMPACT [110], where temperature is normalized to $2T_{e0}$. The *local*, Maxwellian-distribution averaged *e-i* collision time $\overline{\tau}$ is frequently used in the literature (e.g. [44, 70]). This is related to the 'global' normalizing collision time τ_n by the relation $\overline{\tau} = (3\sqrt{\pi}/4)\tau_n\tilde{v}_T^3/(\tilde{Z}^2\tilde{n}_i \ln\Lambda_{ei}/\ln\Lambda_{ei0})$ where $\tilde{v}_T = \sqrt{T_e/T_{e0}}$ is the local, thermal velocity. So $\overline{\tau}$ is adjusted to the local plasma conditions.

In the normalized form of the equations used in the code, the first three of these coupled equations and Maxwell's equations are

$$\frac{D\tilde{f}_0}{D\tilde{t}} + \frac{\tilde{v}}{3}\tilde{\nabla}\cdot\tilde{\mathbf{f}}_1 - \frac{1}{3\tilde{v}^2}\frac{\partial}{\partial v}\tilde{v}\left(\tilde{v}^2\tilde{\mathbf{A}}\cdot\tilde{\mathbf{f}}_1\right) = \frac{1}{Z_0\tilde{v}^2}\,\frac{\partial}{\partial v}\tilde{v}\left[\tilde{C}(\tilde{f}_0)\tilde{f}_0 + \tilde{D}(\tilde{f}_0)\frac{\partial\tilde{f}_0}{\partial\tilde{v}}\right] + \left(\frac{\partial\tilde{f}_0}{\partial t}\right)_{\text{IB}}\,, \tag{3.1}$$

$$\frac{D\tilde{\mathbf{f}}_1}{D\tilde{t}} + \tilde{v}\tilde{\nabla}\tilde{f}_0 - \tilde{\mathbf{A}}\frac{\partial\tilde{f}_0}{\partial\tilde{v}} - \tilde{\boldsymbol{\omega}}\times\tilde{\mathbf{f}}_1 + \left[\frac{2}{5}\tilde{v}\,\tilde{\nabla}\cdot\underline{\underline{\tilde{\mathbf{f}}}}_2 - \frac{2}{5\tilde{v}^3}\,\frac{\partial}{\partial v}\tilde{v}\left(\tilde{v}^3\tilde{\mathbf{A}}\cdot\underline{\underline{\tilde{\mathbf{f}}}}_2\right)\right]$$
$$= -\frac{\tilde{Z}^2\tilde{n}_i}{\tilde{v}^3}\tilde{\mathbf{f}}_1 + \tilde{C}_{ee1}(\tilde{f}_0,\tilde{\mathbf{f}}_1)\,, \tag{3.2}$$

$$\left[\frac{D\underline{\underline{\tilde{\mathbf{f}}}}_2}{D\tilde{t}} + \tilde{v}\left(\tilde{\nabla}\underline{\underline{\mathbb{I}}} - \frac{1}{3}\underline{\underline{\mathbb{I}}}\tilde{\nabla}\right)\cdot\tilde{\mathbf{f}}_1 - \tilde{v}\left(\tilde{\mathbf{A}}\,\underline{\underline{\mathbb{I}}} - \frac{1}{3}\underline{\underline{\mathbb{I}}}\,\tilde{\mathbf{A}}\right)\cdot\frac{\partial}{\partial v}\tilde{v}\left(\tilde{\mathbf{f}}_1/\tilde{v}\right) - 2\tilde{\boldsymbol{\omega}}\times\underline{\underline{\tilde{\mathbf{f}}}}_2\right.$$
$$\left. + \mathcal{O}(f_3) + 3\frac{\tilde{Z}^2\tilde{n}_i}{\tilde{v}^3}\underline{\underline{\tilde{\mathbf{f}}}}_2\right]_2 = \tilde{C}_{ee2}(\tilde{f}_0,\tilde{\mathbf{f}}_1,\underline{\underline{\tilde{\mathbf{f}}}}_2)\,, \tag{3.3}$$

$$\tilde{\nabla}\times\tilde{\boldsymbol{\omega}} = \left(\frac{1}{\tilde{\delta}_c}\right)^2\tilde{\mathbf{j}} + \left(\frac{1}{\tilde{c}}\right)^2\frac{\partial\tilde{f}_0}{\partial\tilde{v}}\quad, \tag{3.4}$$

$$\tilde{\nabla}\times\tilde{\mathbf{E}} = -\frac{\partial\boldsymbol{\omega}}{\partial t}\quad. \tag{3.5}$$

where $[\ ]_l$ denotes the summation of all permutations and division by l. The convective derivative is defined in terms of the ion fluid velocity by

$$\frac{D}{D\tilde{t}} = \frac{\partial}{\partial \tilde{t}} + \tilde{\mathbf{C}} \cdot \tilde{\nabla} \ , \tag{3.6}$$

and the transformed electric field is given by

$$\tilde{\mathbf{A}} = \tilde{\mathbf{E}} + \tilde{\mathbf{C}} \times \tilde{\boldsymbol{\omega}} - \frac{D\tilde{\mathbf{C}}}{D\tilde{t}} \ , \tag{3.7}$$

The code uses a hydrodynamic ion model, with continuity and momentum equations for the ions given by

$$\frac{\partial \tilde{n}_i}{\partial \tilde{t}} + \tilde{\nabla} \cdot \left(\tilde{n}_i \tilde{\mathbf{C}} \right) = 0 \ , \tag{3.8}$$

$$\frac{M_i}{Z_0 m_e} \tilde{n}_i \left(\frac{\partial \tilde{\mathbf{C}}}{\partial \tilde{t}} + \tilde{\mathbf{C}} \cdot \tilde{\nabla} \tilde{\mathbf{C}} \right) = \left(\tilde{Z} \tilde{n}_i - \tilde{n}_e \right) \tilde{\mathbf{E}} + \tilde{\mathbf{j}} \times \tilde{\boldsymbol{\omega}} - \tilde{\nabla} \cdot \left(\tilde{p}_e \underline{\underline{\mathbb{I}}} + \underline{\underline{\tilde{\Pi}}} \right) \ , \tag{3.9}$$

where the additional set of normalizations in the hydrodynamic equations is $\tilde{n}_i = Z_0 n_i / n_{e0}$, $\tilde{\mathbf{C}} = \mathbf{C}/v_n$, and $\underline{\underline{\tilde{\Pi}}} = \underline{\underline{\Pi}}/(m_e v_n^2 \, n_{e0})$. M_i is the mass of the ion species.

This ion model is a reduced version of the model developed by Ridgers [101], but also includes ion contributions to $\underline{\underline{\mathbf{f}}}_2$ by inclusion of the corrections in the $\underline{\underline{\mathbf{f}}}_2$ equation. Note that the first term on the right hand side of Eq. (3.2) and last term on the left hand side of Eq. (3.3) correspond to electron-ion collisions. In un-normalized form, the former is $-\nu_{ei}\mathbf{f}_1$ where $\nu_{ei} = Y \, Z^2 n_i / v^3 \, \ln \Lambda_{ei}$ is the electron-ion angular scattering frequency for an electron with speed v, $Y = 4\pi (e^2/4\pi\epsilon_0 m_e)^2$, and $\ln \Lambda_{ei}$ the Coulomb logarithm for electron-ion scattering. This assumes that the ions are cold so that their thermal velocity spread is much less than the electron speed appearing in ν_{ei}. The Rosenbluth coefficients

$C(f_0)$ and $D(f_0)$ are

$$\tilde{H}(\tilde{v},\tilde{\mathbf{r}},\tilde{t}) = 4\pi \int_0^{\tilde{v}} \tilde{f}_0(\tilde{u},\tilde{\mathbf{r}},\tilde{t})\tilde{u}^2 d\tilde{u} \ , \tag{3.10}$$

$$\tilde{G}(\tilde{v},\tilde{\mathbf{r}},\tilde{t}) = \frac{4\pi}{\tilde{v}} \int_0^{\tilde{v}} \tilde{u}^2 \left\{ \int_{\tilde{u}}^{\infty} \tilde{f}_0(\tilde{w},\tilde{\mathbf{r}},\tilde{t})\tilde{w} d\tilde{w} \right\} d\tilde{u} \ . \tag{3.11}$$

Note that the e–e collision terms $\tilde{C}_{ee1}$ and $\tilde{C}_{ee2}$ are nonlinear, integro-differential operators involving f_0, $\mathbf{f}_1$ and $\underline{\underline{\mathbf{f}}}_2$ that are reminiscent of the right hand side of Eq. (3.1) but more involved.

3.1.1 Inverse Bremsstrahlung Heating Operator

Langdon [74] formulated an expression describing inverse bremsstrahlung heating by analyzing the first order cycle-averaged effect of an oscillating electric field on electrons in the presence of collisions with ions, resulting in an isotropic heating and distortion of the distribution function.

Following a similar approach to Langdon where the Vlasov-Fokker-Planck equation for $\mathbf{f}_1$, in the approximation that electron inertia, $\underline{\underline{\mathbf{f}}}_2$, magnetic fields ω_B and gradients in f_0 are small gives

$$\frac{\partial \mathbf{f}_1}{\partial t} = \mathbf{E}\frac{\partial}{\partial v} f_0 - \frac{n_i Z^2}{v^3}\mathbf{f}_1 \ , \tag{3.12}$$

Under the same assumptions, and ignoring electron-electron collisions, the equation for f_0 is

$$\frac{\partial f_0}{\partial t} = \frac{\mathbf{E}}{3v^2} \cdot \frac{\partial}{\partial v}(v^2 \mathbf{f}_1) \ . \tag{3.13}$$

Although the time average over the fast oscillations of the electric field will yield a zero $\mathbf{f}_1$, $\mathbf{E} \cdot \mathbf{f}_1$ will be non-zero and heat the electrons. Equation (3.12) can be analyzed for laser

fields oscillations at frequency ω by

$$\mathbf{f}_1 = \frac{\mathbf{E}}{\left(i\omega + \frac{n_i Z^2}{v^3}\right)} \frac{\partial}{\partial v} f_0 \ , \tag{3.14}$$

the real part of which is

$$\frac{1}{2}(\mathbf{f}_1 + \mathbf{f}_1^*) = \frac{\mathbf{E}}{2} \left[\frac{1}{\left(i\omega + \frac{n_i Z^2}{v^3}\right)} + \frac{1}{\left(-i\omega + \frac{n_i Z^2}{v^3}\right)} \right] \frac{\partial}{\partial v} f_0 = \frac{n_i Z^2 \mathbf{E}}{v^3 \left(\omega^2 + \frac{1}{\tau_{ei}^2}\right)} \frac{\partial}{\partial v} f_0 \ .$$

Rearranging and taking the time averaged dot product with $\mathbf{E}$ yields:

$$\langle \mathbf{E} \cdot \mathbf{f}_1 \rangle = \frac{n_i Z^2}{2v^3} \frac{{E_0}^2}{\omega^2} \frac{1}{\left(1 + \frac{1}{\omega^2 \tau_{ei}^2}\right)} \frac{\partial}{\partial v} f_0 \equiv \frac{n_i Z^2}{2v^3} \frac{{E_0}^2}{\omega^2} g(\omega \tau_{ei}) \frac{\partial}{\partial v} f_0 \ , \tag{3.15}$$

where E_0 is the peak laser field. Assuming $g(\omega\tau_{ei}) \approx 1$ (which is to say that the laser frequency is much larger than the electron-ion collision frequency), we get a contribution to $\mathbf{f}_1$ that when contracted and time averaged with $\mathbf{E}$ is a source of heating in the f_0 equation:

$$\mathbf{f}_{1\text{laser}} = \left[\frac{\mathbf{E}}{{E_0}^2} \right] \frac{1}{2} n_i Z^2 v_0^2 \frac{1}{v^3} \frac{\partial}{\partial v} f_0 \tag{3.16}$$

where $v_0 = E_0/\omega$ is the maximum electron oscillation velocity in the laser field. Inserting into the f_0 equation yields Langdon's heating operator:

$$\left. \frac{\partial f_0}{\partial t} \right|_{IB} = \frac{1}{6} n_i Z^2 v_0^2 \frac{1}{v^2} \frac{\partial}{\partial v} \left(\frac{1}{v} \frac{\partial}{\partial v} f_0 \right) \ . \tag{3.17}$$

3.2 Numerical Form of the Equations

The equations from Section 3.1 are differenced over a volume of the x, y, v phase-space defined over $x_{min} \leq x \leq x_{max}$, $y_{min} \leq y \leq y_{max}$ and $v_{min} \leq v \leq v_{max}$. In this section,

and for the rest of the thesis, for convenience the tildes are omitted from the normalized quantities throughout. This computational domain is divided up into $n_x \times n_y \times n_v$ cells. The finite difference notation for a function $f(x_i, y_j, v_k, t_n) \equiv f^n_{i,j,k}$. Alternatively, functions of time and space only will be denoted by $f^n_{i,j}$.

3.2.1 Electron Vlasov-Fokker-Planck Equation

The electron kinetic equations are finite differenced as follows. The equation for f_0 (Eq. (3.1)) in finite difference form is

$$\left(\frac{1}{\Delta t} + \mathbf{C}^n \cdot \nabla\right) {f_0}^{n+1,l+1} + \frac{v}{3}\nabla \cdot {\mathbf{f}_1}^{n+1,l+1} - \frac{1}{3v^2}\frac{\partial}{\partial v} v\left(v^2 \mathbf{E}^{n+1} \cdot {\mathbf{f}_1}^{n+1,l}\right) - \left[C_{ee0} + H\right]^{n+1}$$
$$= \frac{{f_0}^n}{\Delta t} + \frac{1}{3v^2}\left[\mathbf{U}^n \times \boldsymbol{\omega}^n - \left(\frac{D\mathbf{U}}{Dt}\right)^n\right] \cdot \frac{\partial}{\partial v} v\left(v^2 {\mathbf{f}_1}^n\right) \ , \tag{3.18}$$

where C_{ee0} and H are the electron-electron collision and inverse bremsstrahlung heating operators described in [110]. The equation for $\mathbf{f}_1$ (Eq. (3.2)) is

$$\left(\frac{1}{\Delta t} + \mathbf{C}^n \cdot \nabla\right) {\mathbf{f}_1}^{n+1,l+1} + v\nabla {f_0}^{n+1,l+1} - \mathbf{E}^{n+1}\frac{\partial {f_0}^{n+1,l}}{\partial v} - \boldsymbol{\omega}^{n+1} \times {\mathbf{f}_1}^{n+1,l}$$
$$+ \left[\frac{2}{5} v\, \nabla \cdot \underline{\underline{\mathbf{f}}}_2^{\,n+1,l+1} - \frac{2}{5v^3}\frac{\partial}{\partial v} v\left(v^3 \mathbf{E}^{n+1} \cdot \underline{\underline{\mathbf{f}}}_2^{\,n+1,l}\right)\right] - \frac{Z^2 n_i}{v^3}{\mathbf{f}_1}^{n+1,l+1}$$
$$= \frac{{\mathbf{f}_1}^n}{\Delta t} + \left[\mathbf{C}^n \times \boldsymbol{\omega}^n - \left(\frac{D\mathbf{C}}{Dt}\right)^n\right] \cdot \left[\underline{\underline{\mathbb{I}}}\frac{\partial {f_0}^n}{\partial v} + \frac{2}{5v^3}\frac{\partial}{\partial v} v\left(v^3 \underline{\underline{\mathbf{f}}}_2^{\,n}\right)\right] \ . \tag{3.19}$$

The equation for $\underline{\underline{\mathbf{f}}}_2$ (Eq. (3.3)) is

$$\left[\left(\frac{1}{\Delta t}+\mathbf{C}^n\cdot\nabla\right)\underline{\underline{\mathbf{f}}}_2{}^{n+1,l+1}+v\left(\nabla\underline{\underline{\mathbb{I}}}-\frac{1}{3}\underline{\underline{\mathbb{I}}}\nabla\right)\cdot\mathbf{f}_1{}^{n+1,l+1}\right.$$
$$-v\left(\mathbf{E}^{n+1}\underline{\underline{\mathbb{I}}}-\frac{1}{3}\underline{\underline{\mathbb{I}}}\mathbf{E}^{n+1}\right)\cdot\frac{\partial}{\partial v}v\left(\frac{\mathbf{f}_1}{v}^{n+1,l}\right)-2\boldsymbol{\omega}^n\times\underline{\underline{\mathbf{f}}}_2{}^{n+1,l+1}+3\frac{Z^2n_i}{v^3}\underline{\underline{\mathbf{f}}}_2{}^{n+1,l+1}$$
$$\left.=\frac{\underline{\underline{\mathbf{f}}}_2}{\Delta t}^n+v\left(\left[\mathbf{U}^n\times\boldsymbol{\omega}^n-\left(\frac{D\mathbf{U}}{Dt}\right)^n\right]\underline{\underline{\mathbb{I}}}-\frac{1}{3}\underline{\underline{\mathbb{I}}}\left[\mathbf{U}^n\times\boldsymbol{\omega}^n-\left(\frac{D\mathbf{U}}{Dt}\right)^n\right]\right)\cdot\frac{\partial}{\partial v}v\left(\frac{\mathbf{f}_1}{v}^n\right)\right]_2, \tag{3.20}$$

where, as before, $\underline{\underline{\mathbb{I}}}$ is the identity tensor and $[\ ]_l$ denotes the summation of all permutations and division by l. For simplicity, the terms from the hydrodynamic solver are differenced explicitly except for the convective derivative. The corrections to the electric field due to the hydro-motion are given by

$$\left(\frac{D\mathbf{C}}{Dt}\right)^n=\frac{\alpha}{n_i}\left[\left(Z^n_{i,j}(n_i)^n_{i,j}-(n_e)^n_{i,j}\right)\mathbf{E}^n_{i,j}+\mathbf{j}^n_{i,j}\times\boldsymbol{\omega}^n_{i,j}-\nabla_{i,j}\left((p_e)^n_{i,j}\underline{\underline{\mathbb{I}}}+\underline{\underline{\Pi}}^n_{i,j}\right)\right]. \tag{3.21}$$

Center differencing is used for both velocity grid and spatial grid derivatives. As was discussed in reference [110], center differencing of the velocity space turns out to be stable in this scheme. Velocity derivatives and integrals in IMPACTA, i.e. finite differences and summations involving v_k, are similar to those in IMPACT [110]. The derivatives with respect to velocity used in the code are calculated using

$$\frac{\partial}{\partial v}\left(v^m f_s\right)\equiv\frac{{v_k}^m f^n_{i,j,k+1}-{v_k}^m f^n_{i,j,k-1}}{\Delta v_{k+1}+\Delta v_{k-1}}. \tag{3.22}$$

The simulation quantities are cell-centered rather than having some located at the boundaries as in IMPACT. This results in a slight loss in accuracy (center-differencing of spatial derivatives now gives $\sim(2\Delta)^2$ accuracy instead of $\sim\Delta^2$ accuracy due to the loss of quan-

tites defined at $i+1/2$ and $i-1/2$) for the compensation of simplicity of indexing, which for the very complex $\underline{\mathbf{f}}_{\underline{=}2}$ equation is convenient. In addition, it greatly simplifies the spatial gradient terms, which are defined as

$$\left(\frac{\partial f}{\partial x}\right)^n_{i,j,k} \equiv \frac{f^n_{i+1,j,k} - f^n_{i-1,j,k}}{2\Delta x_i} \,, \tag{3.23}$$

$$\left(\frac{\partial f}{\partial y}\right)^n_{i,j,k} \equiv \frac{f^n_{i,j+1,k} - f^n_{i,j-1,k}}{2\Delta y_j} \,. \tag{3.24}$$

Other spatial operators including divergence, curl and gradient are all formed by the linear combination of the finite difference operators. Because the spatial derivatives in the finite differenced equations are in divergence form, it is easy to demonstrate the conservation properties of this differencing scheme by summing up over the domain and showing complete cancellation for periodic and reflecting boundaries.

3.2.2 Ion Hydrodynamic Equations

The finite differenced form of the equations used in IMPACTA for the hydrodynamics can be explicit because of the significant difference in important timescales between electrons and ions due to their mass difference. The ion velocity equation, Eq. (3.9), that depends on the thermal and magnetic pressure is pushed via a two step algorithm [112] given by

$$\mathbf{C}^{n\star}_{i,j} = \mathbf{C}^n_{i,j} + \Delta t \frac{\alpha}{n_i}\left[\left(Z^n_{i,j}(n_i)^n_{i,j} - (n_e)^n_{i,j}\right)\mathbf{E}^n_{i,j} + \mathbf{j}^n_{i,j} \times \boldsymbol{\omega}^n_{i,j} - \nabla_{i,j}\left((p_e)^n_{i,j}\underline{\underline{\mathbb{I}}} + \underline{\underline{\Pi}}^n_{i,j}\right)\right] \,, \tag{3.25}$$

where $\alpha = Z_0 m_e/M_i$. Next the plasma is transported with the bulk flow velocity and the new plasma velocity is found by

$$\mathbf{C}^{n+1}_{i,j} = \mathbf{C}^{n\star}_{i,j} - \Delta t \mathbf{C}^{n\star}_{i,j} \cdot \nabla_{i,j}\mathbf{C}^{n\star}_{i,j} \,, \tag{3.26}$$

3.3 Laser Propagation with Ray Tracing

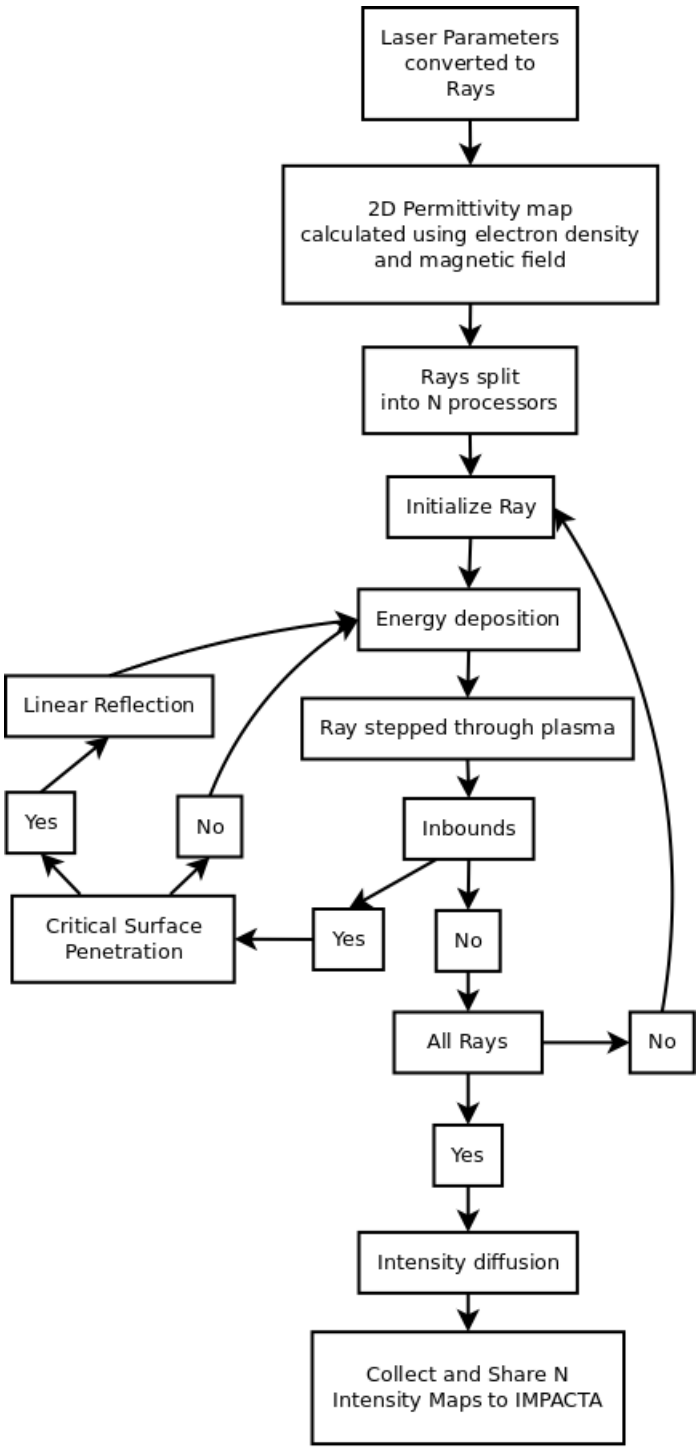

Figure 3.1: Flowchart describing the laser propagation module.

Laser propagation is calculated using an adapted implementation of the finite differ-

enced ray-tracing equations given in ref. [113] which are

$$\mathbf{r}_{1/2} = \mathbf{r}_0 + \mathbf{v}_0 \frac{ds}{2}, \tag{3.27}$$

$$\Omega_0 = \left(\frac{\nabla\epsilon}{2\epsilon}\right)_{1/2} \times \mathbf{v}_0 \frac{ds}{2}, \tag{3.28}$$

$$\Omega_{1/2} = \left(\frac{\nabla\epsilon}{2\epsilon}\right)_{1/2} \times (\mathbf{v}_0 + \mathbf{v}_0 \times \Omega_0) \frac{ds}{2}, \tag{3.29}$$

$$\mathbf{v}_1 = \mathbf{v}_0 + \frac{2}{1 + (\Omega_{1/2}\frac{ds}{2})^2}(\mathbf{v}_0 + \mathbf{v}_0 \times \Omega_{1/2}) \times \Omega_{1/2}, \tag{3.30}$$

$$\mathbf{r}_1 = \mathbf{r}_{1/2} + \mathbf{v}_1 \frac{ds}{2}. \tag{3.31}$$

The details of this implementation are provided in Appendix B but a flowchart describing the procedure is given in Fig. 3.1. By passing along the laser intensity profile from the ray-tracing to the inverse Bremsstrahlung heating operator, the module is designed to deposit laser energy along a dynamic path.

3.4 Numerical Convergence

Numerical diffusion arises naturally as a consequence of finite difference of the equations in space, time, and velocity and affects transport calculations. In order to ensure that the code converges after increasing resolution in velocity, space, and time, 1D test runs with laser heating upon a density gradient were performed over 1 ns. The laser heating is performed such that it spatially reproduces the heating profile that is created by the ray-tracing. Figure 3.2 shows the results of these tests 250 ps after the start of the heating. The density distribution is given by $n_e(x,y) = (2.98 + 2.93\tanh(\frac{x-750}{40}))\ 10^{22}/\text{cm}^3$. The Z gradient is given by $Z(x,y) = 41.25 + 37.75\tanh(\frac{x-750}{40})$. The heating profile is described by $H(x,y) = \exp(-\left(\frac{x-750}{100}\right)^2) + \exp(-\left(\frac{x+750}{100}\right)^2)$.

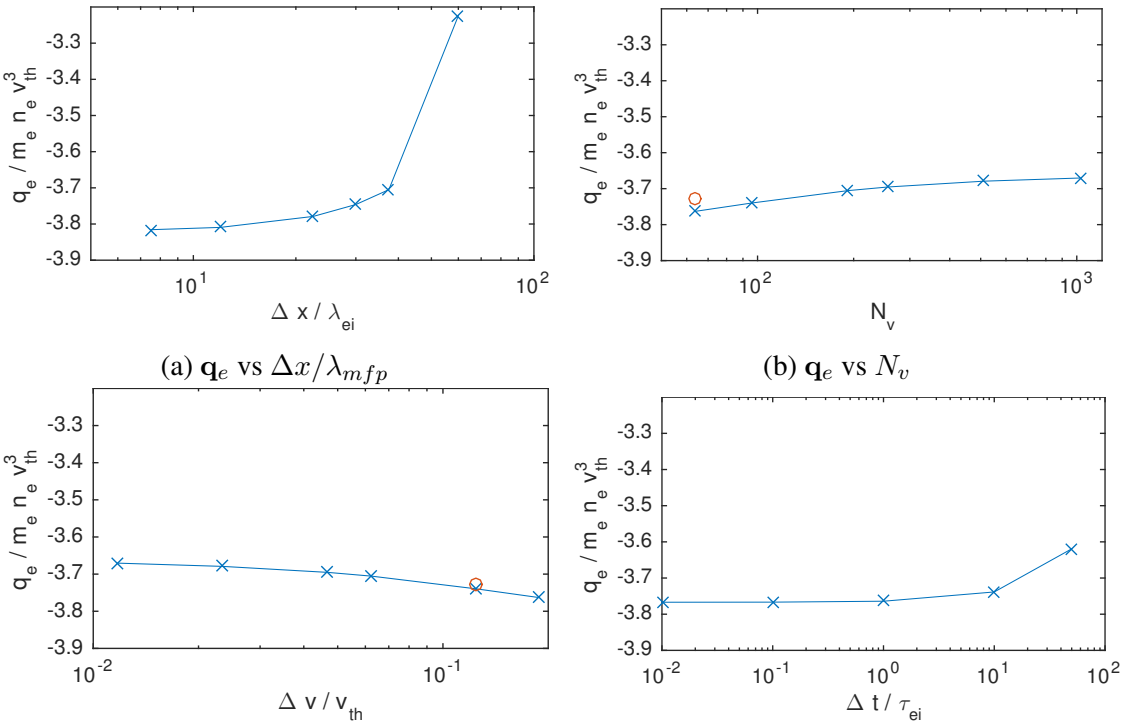

(a) $\mathbf{q}_e$ vs $\Delta x/\lambda_{mfp}$

(b) $\mathbf{q}_e$ vs N_v

(c) $\mathbf{q}_e$ vs $\Delta v/v_{th}$

(d) $\mathbf{q}_e$ vs $\Delta t/\tau_{ei}$

Figure 3.2: The heat flow at 250 ps is compared for a series of discretizations in (a) space, (b) and (c) velocity space, and (d) time to quantify the effects of numerical diffusion. The red circle represents the calculation from a non-uniform grid in velocity space where $(\Delta v/v_{th})_{\text{min}} = 0.125$ and $N_v = 64$.

Figure 3.2a shows that numerical diffusion due to finite differencing of the spatial grid affects the total heat flow by approximately 10% from accumulation over a 250 ps time-scale. Finite differencing of the velocity grid shows that the distribution function is resolved well enough such that the heat flow is affected on the order of a percent. Diffusion due to differencing in time also affects the heat flow on the order of a percent. The data are plotted over the same range to illustrate that numerical diffusion due to spatial differencing is much more influential than diffusion from velocity and time differencing. Figure 3.2 also illustrates convergence with increasing resolution.

In the modeling performed for the research results in this thesis, $\Delta x/\lambda_{\text{mfp}} \sim 30$, $\Delta t/\tau_{\text{ei}} \sim 1.2$ and $(\Delta v/v_{\text{th}})_{\text{min}} = 0.125$. The minimum value is given because the modeling uses a non-uniform grid in velocity space to resolve the tail of the distribution function. The tail

is captured by the larger velocity cells while the details of the distribution near thermal velocities are preserved with smaller velocity cells. Since the initial temperature is small, a non-uniform grid enables efficient computation at earlier times when the plasma is relatively cold. Fig. 3.2b and c show the heat-flow from a simulation with a non-uniform velocity grid, indicated by the red circle, where the non-uniform simulation effectively reproduces the heat flow from a calculation that uses 3 times as many velocity cells. Using a non-uniform velocity grid is primarily motivated by the decrease in computation time.

CHAPTER 4

Self-Generated Magnetic Fields and Electron Transport Dynamics in a Hohlraum

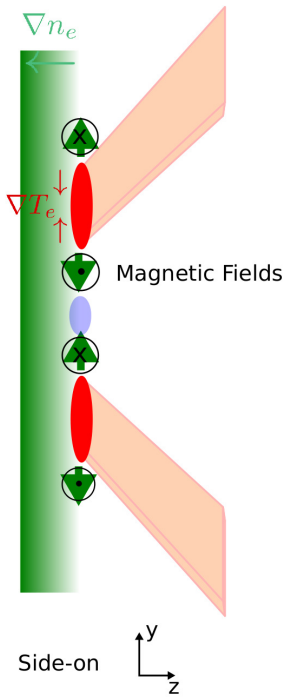

Figure 4.1: The Biermann Battery mechanism is illustrated where the temperature gradients induced by the laser heating are in $\hat{y}$ while the material density gradient is in $\hat{x}$. This creates magnetic fields around the laser heating region in $\hat{z}$. These geometries are ubiquitous in a hohlraum and therefore, understanding the influence of these fields on thermal energetics in this geometry is very important.

In Section 2.3, the magnetic field self-generation mechanism was introduced where a magnetic field arises due to orthogonal gradients in density and temperature. This mecha-

nism is particularly applicable at the laser incidence region near the high Z surface of the hohlraum. From the side-on view for one of the spots, shown in Fig. 4.1, the temperature gradient in $\hat{y}$ that arises due to the laser heating is perpendicular to the material density gradient in $\hat{x}$. The orthogonal gradients produce a curl in the electric field resulting in a magnetic field in the $\hat{z}$ direction. In what follows, a kinetic formulation for the generation of magnetic field in the presence of laser-heating is obtained and a magnetic field generation mechanism that depends on the gradients of the distribution function is discussed. This chapter discusses the influence of kinetic effects that may arise from non-local transport and inverse Bremsstrahlung (IB) heating, introduced in Section 2.2, in the presence of these self-generated magnetic fields.

4.1 Kinetic Formulation of Magnetic Field Generation

Studying the effects of electron kinetics on magnetic field generation requires a version of the Biermann battery mechanism that takes into account the shape of the distribution function. A model can be developed for magnetic field generation from a general DLM distribution akin to that for the Biermann battery effect. The term corresponding to the pressure gradient from Eq. (2.77) that is responsible for the magnetic field generation[1] can be expanded if the f_0 moments can be evaluated. In the presence of laser-heating, by assuming the distribution is a DLM due to laser-heating, the moments are analytically

[1] Refer to Section 2.3 for details.

determined. Substituting Eq. (2.64) into Eq. (2.54) yields

$$n_e\langle v^n\rangle = 4\pi\int_0^\infty f_{sG}\, v^{n+2}dv, \tag{4.1}$$

$$= 4\pi C(m)\frac{n_e}{(2T_e)^{3/2}}\int_0^\infty \exp\left[-\left(\frac{v}{\alpha_e\sqrt{2T_e}}\right)^m\right] v^{n+2}dv,$$

$$= \left(3\frac{\Gamma[\frac{3}{m(x,y)}]}{\Gamma[\frac{5}{m(x,y)}]}\right)^{n/2}\frac{\Gamma\left[\frac{3+n}{m(x,y)}\right]}{\Gamma[\frac{3}{m(x,y)}]}n_e(x,y)\, T_e(x,y)^{n/2}, \tag{4.2}$$

where $\Gamma(z) = (z-1)!$ is the gamma function for all $z > 0$. Using this relation for the f_0 moments provides a model for magnetic field generation from a DLM distribution function. By substituting Eq. (4.2) into $\frac{\nabla(n_e\langle v^5\rangle)}{6n_e\langle v^3\rangle}$ from Eq. (2.77) gives

$$\mathbf{E} = \frac{1}{4}\frac{\Gamma\left(\frac{3}{m(x,y)}\right)\Gamma\left(\frac{8}{m(x,y)}\right)}{\Gamma\left(\frac{6}{m(x,y)}\right)\Gamma\left(\frac{5}{m(x,y)}\right)}\frac{1}{m(x,y)^2n_e(x,y)}$$

$$2m(x,y)^2T_e(x,y)\nabla n_e(x,y)$$

$$+C_En_e(x,y)T_e(x,y)\nabla m(x,y)$$

$$+5m(x,y)^2n_e(x,y)\nabla T_e(x,y), \tag{4.3}$$

where $C_E = -9\psi\left[\frac{3}{m(x,y)}\right] + 25\psi\left[\frac{5}{m(x,y)}\right] - 16\psi\left[\frac{8}{m(x,y)}\right]$, and $\psi(z) = \Gamma'(z)/\Gamma(z)$.

Equation (4.3) provides a relation for the electric field from the pressure gradient in the presence of DLM distribution functions. In the limit that the distribution function is a Maxwell-Boltzmann, $\mathbf{E} = T_e\nabla n_e/n_e + 5/2\nabla T_e$ as expected. However, the presence of $m(x,y)$ and $\nabla m(x,y)$ creates additional contributions to the electric field. Using Faraday's law, this formulation can be extended to a magnetic field generation mechanism from these additional contributions.

Substituting Eq. (4.2) into Eq. (2.83) gives

$$\begin{aligned}\frac{\partial \mathbf{B}}{\partial t} =& \frac{1}{2}\frac{\Gamma\left(\frac{3}{m(x,y)}\right)\Gamma\left(\frac{8}{m(x,y)}\right)}{\Gamma\left(\frac{6}{m(x,y)}\right)\Gamma\left(\frac{5}{m(x,y)}\right)}\frac{1}{m(x,y)^2 n_e(x,y)}\times \\ & \left(C_T T_e(x,y)\left(\nabla m(x,y)\times\nabla n_e(x,y)\right)\right. \\ & + C_n n_e(x,y)\left(\nabla m(x,y)\times\nabla T_e(x,y)\right) \\ & \left.+\, m(x,y)^2\left(\nabla n_e(x,y)\times\nabla T_e(x,y)\right)\right) \end{aligned} \tag{4.4}$$

where the constants are

$$C_T = -3\psi\left[\frac{3}{m(x,y)}\right] + 5\psi\left[\frac{5}{m(x,y)}\right] + 6\psi\left[\frac{6}{m(x,y)}\right] - 8\psi\left[\frac{8}{m(x,y)}\right] \tag{4.5}$$

$$C_n = -3\left(\psi\left[\frac{3}{m(x,y)}\right] - 5\psi\left[\frac{6}{m(x,y)}\right] + 4\psi\left[\frac{8}{m(x,y)}\right]\right) \tag{4.6}$$

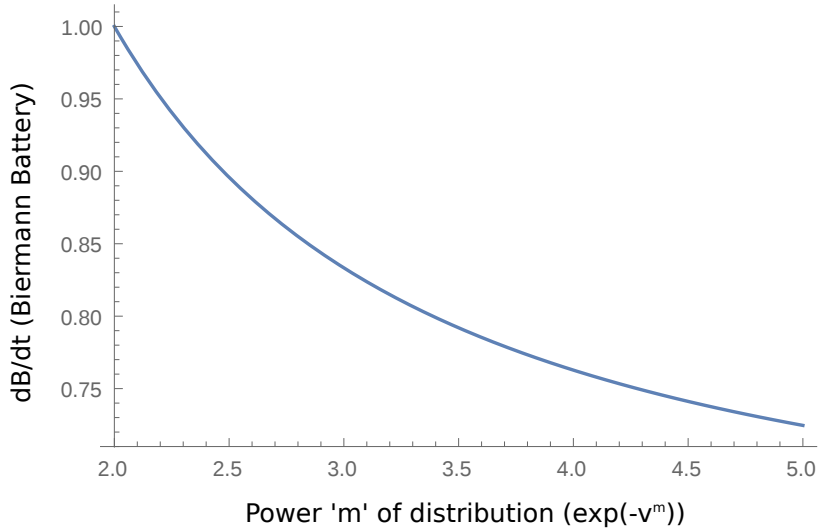

Figure 4.2: DLM distributions result in suppressed field generation rates. In the case of a Langdon distribution where $m = 5$, the field generation rate decreases by nearly 30%.

The previously mentioned Biermann Battery effect is represented by the third term in Eq. (4.4) and can be retrieved by setting $m = 2, \nabla m = 0$. DLM distributions, however, decrease the field generation rate by approximately 25% as shown in Fig. 4.2. Given a

laser intensity of 10^{14} W/cm^2, $m \approx 3.5$ from Eq. (2.65). A suppression of $10\% - 20\%$ is expected for the magnetic field generation rate for such intensities.

The presence of m gradients also results in magnetic field generation as described in the first two terms of Eq. (4.4). Discussion of these effects has been focused on the electric field counterpart of the generation mechanism as in ref. [65]. Ref. [77] has furthered that work and provided transport theory coefficients in the presence of ∇m and briefly discusses the presence of magnetic fields introduced by the presence of ∇m. Next, modeling of ∇m-sourced fields is performed to illustrate the field generation mechanism.

4.2 Modeling Results

4.2.1 Single Spot Field Generation From Gradients in Distribution Function

Using IMPACTA, an m gradient was imposed in the radial direction by setting $m(i,j) = 2.0 + 3.0\exp[-0.02((i-0.5N_x)^2 + (j-0.5N_y)^2)]$. The initial temperature is uniform, $T_e = 1$ in order to isolate one of the ∇m generation mechanism terms. A constant and uniform density gradient, $\partial_z n_e = 0.1$, was imposed out of plane. This gradient creates an electric field in $\hat{z}$ given by simplifying Eq. (4.3) for a $\hat{z}$ gradient only in density. The relation that describes the electric field is

$$E_z = \frac{1}{2}\frac{\Gamma\left(\frac{3}{m(x,y)}\right)\Gamma\left(\frac{8}{m(x,y)}\right)}{\Gamma\left(\frac{6}{m(x,y)}\right)\Gamma\left(\frac{5}{m(x,y)}\right)}\frac{T_e(x,y)}{n_e(x,y)}\partial_z n_e. \tag{4.7}$$

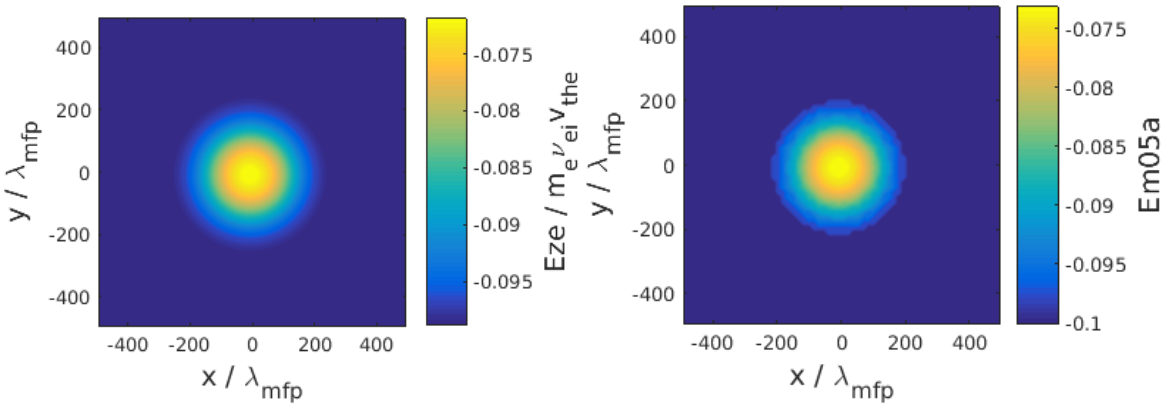

(a) $E_{z-\text{code}}$ (b) $E_{z-\text{Eq. (4.7)}}$

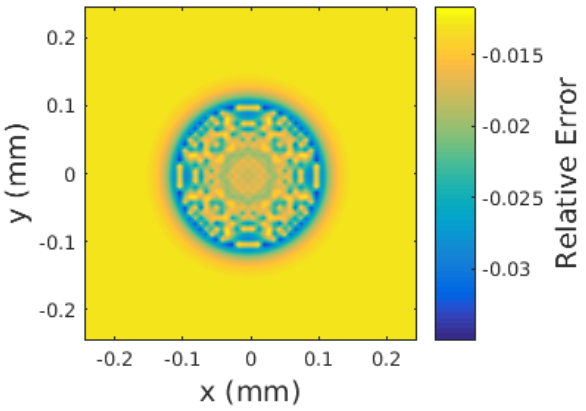

(c) Relative error

Figure 4.3: The electric fields from a radial gradient in the DLM coefficient @ $t = 1\tau_{ei}$. (a) E_z from code, (b) E_z from Eq. (4.7), and (c) $E_{z-\text{code}}/E_{z-\text{Eq. (4.7)}} - 1$

Figure 4.3 shows good agreement between the calculation from the code, shown in (a), and that from the analytical formulation in Eq. (4.7), in (b). The slight discrepancy may be due to the fact that the distribution function is not static. Equation (4.7) reduces to $E_z = T_e \partial_z n_e / n_e$ when $m(x, y) = 2.0$.

From Faraday's law, the curl of the electric field gives the magnetic field. The ∇m

contribution to the magnetic field in the plane of the simulation is given by

$$\frac{\partial B_x}{\partial t} = \frac{1}{2}\frac{\Gamma\left(\frac{3}{m(x,y)}\right)\Gamma\left(\frac{8}{m(x,y)}\right)}{\Gamma\left(\frac{6}{m(x,y)}\right)\Gamma\left(\frac{5}{m(x,y)}\right)}\frac{0.1C_T T_e(x,y)}{m(x,y)^2 n_e(x,y)}\left(\partial_y m(x,y) + m(x,y)^2 \partial_y T_e(x,y)\right) \tag{4.8}$$

and is shown in Fig. 4.4a.

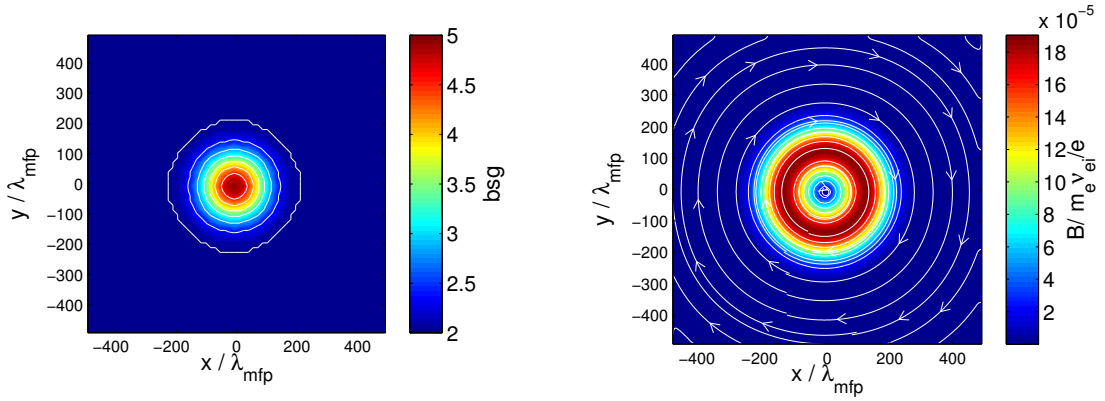

(a) ∇m @ $t = 0$ (b) $\mathbf{B}$ @ $t = 1\tau_{ei}$

Figure 4.4: The initial m profile (a) with a uniform out-of-plane density gradient generates an azimuthal magnetic field (b).

Since the gradients in plasma density, temperature, and distribution function shape are significantly more complicated in a hohlraum geometry, the influence of kinetic effects on the magnetic field generation must be examined. The following section shows full-scale 2D hohlraum modeling that self-consistently includes the kinetic magnetic field generation mechanism along with IB heating.

4.3 Hohlraum Modeling

Using IMPACTA, 2D simulations of laser heating in a hohlraum geometry are performed. The normalizing laser intensity is $I\lambda^2 = 1.6 \times 10^{15}$ W/cm^2 while the normalizing electron density is, $n_{e0} \approx 10^{21}$ cm^{-3}, the normalizing charge $Z_0 = 79$, and normalizing mass is $A = 197$. The plasma starts at a background temperature of approximately $T_e = 0.1 \approx 50$

eV corresponding to a normalizing electron thermal velocity of $v_{\text{th}}/c = 0.08$.

A 2-dimensional slice of a hohlraum is modeled in the x-y plane where the y-axis represents the longitudinal axis of the hohlraum and the fuel pellet would sit at the origin. The fuel pellet is not modeled in this study. The hohlraum walls are approximated by an almost fully ionized, high Z plasma and they are located at approximately $x = \pm 2$ mm while the fill is approximated with a slightly ionized high Z plasma, effectively a low Z plasma. The density distribution is given by $n_e(x, y) = 10.0(6.48 + 6.39\tanh((x - 4474)/600))$ and the Z profile by $Z(x, y) = 0.5 + 0.45\tanh((x - 4474)/600)$. The laser parameters are provided by [114]. The ray tracing package tracks 4 laser cones to their critical surfaces and allows for some reflection.

Figure 4.5 illustrates the initial setup of the simulation and shows the laser heated region at approximately 10 ps into the simulation. The laser light enters from $x = 0, y = \pm 4$mm.

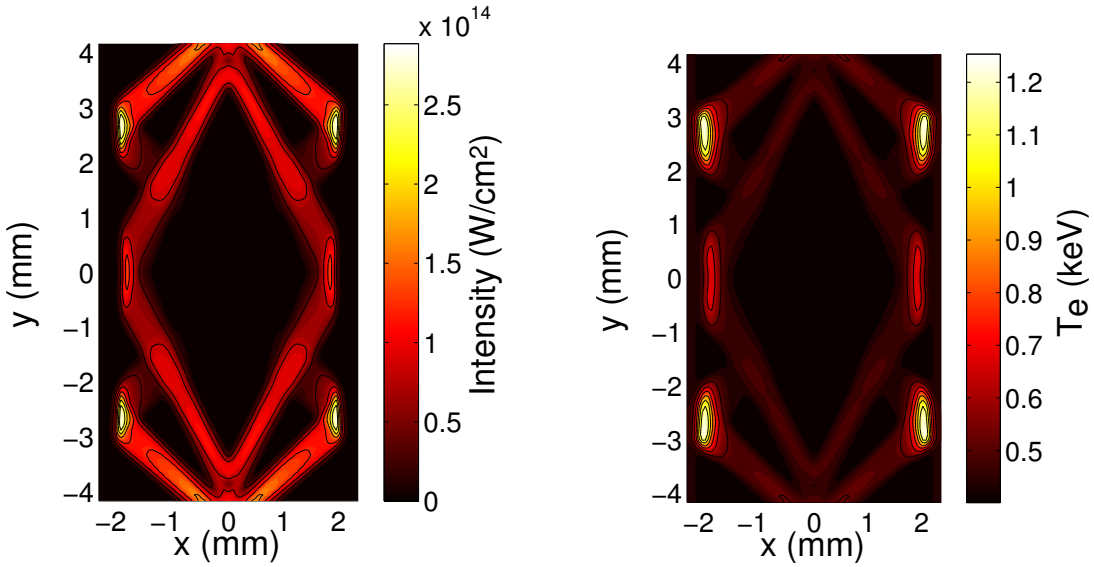

(a) Intensity @ $t = 10$ ps

(b) T_e @ $t = 10$ ps

Figure 4.5: Intensity profile (left) and temperature profile (right) at 10 ps into the simulation.

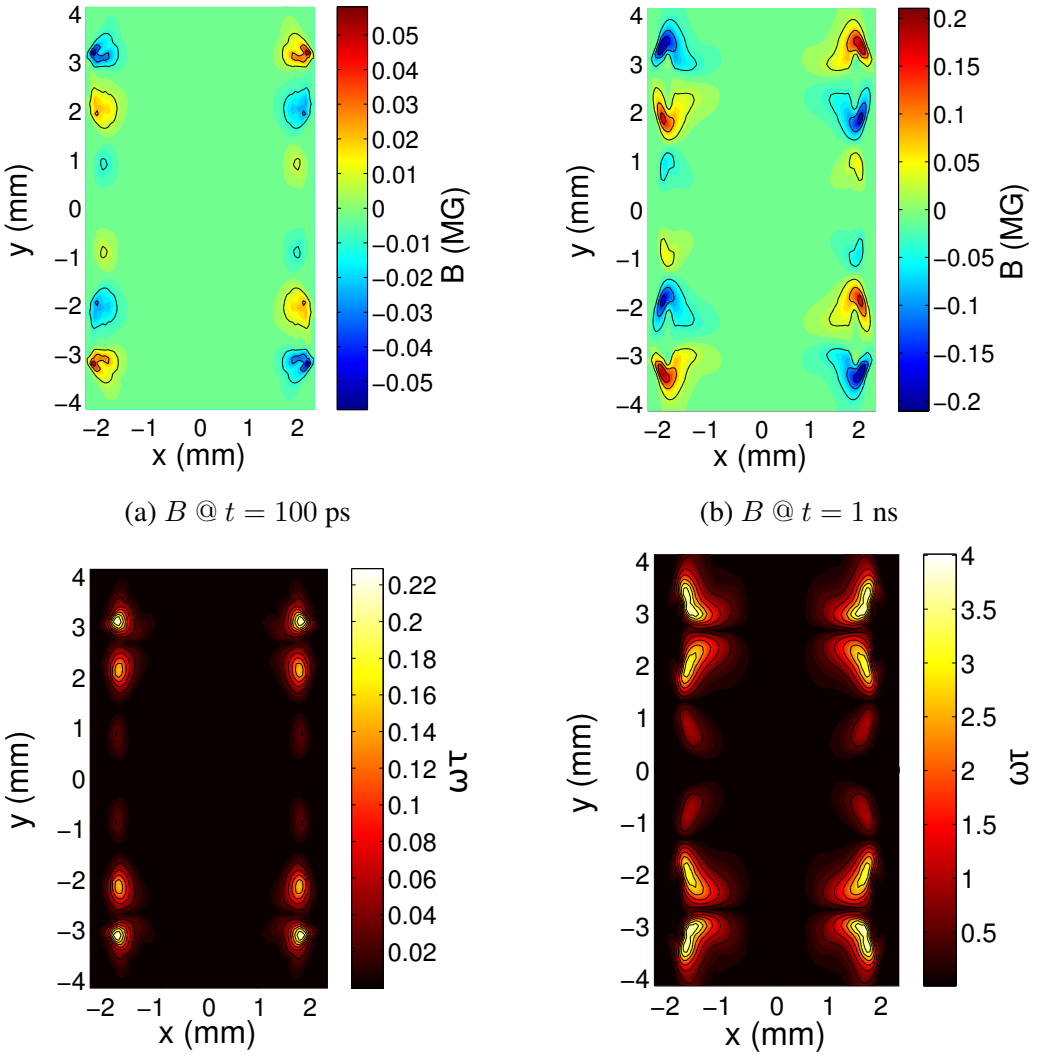

(a) B @ $t = 100$ ps

(b) B @ $t = 1$ ns

(c) B @ $t = 100$ ps

(d) B @ $t = 1$ ns

Figure 4.6: Magnetic fields 100 ps (a) and 1 ns (b) into the simulation. Corresponding magnetization is shown in (c) and (d).

4.3.1 Magnetic Field Generation

The resulting magnetic field is shown in Fig. 4.6. The magnetic fields are approximately 0.2 MG in magnitude, similar to those measured in [41, 47]. Some portion of these magnetic fields is transported towards the axis due to heat flows in addition to plasma bulk flow. These elongated structures in Fig. 4.6b resemble those seen in ref. [48]. Much of the magnetic field, however, is generated near the critical surface and transported laterally due

to the Nernst effect. The Righi Leduc heat flow that arises as the plasma is magnetized also transports the magnetic field towards the overdense plasma. This agrees well with observation and modeling of self-generated magnetic fields on thin foils [115, 87].

The $\mathcal{O}(10)$T magnetic fields result in magnetization of the plasma, especially the low density plasma near the location of laser incidence. Figure 4.6d shows that the plasma is magnetized i.e. $\omega\tau > 1$ at 1 ns into the laser pulse. Since $\omega\tau \sim n_e^{-1}$, the lower density plasma magnetizes earlier.

As suggested in the introduction, the motivation for the study is to observe and understand the effect of such self-generated magnetic fields on the thermal energy transport dynamics of the hohlraum plasma. The magnetization of the plasma causes interesting thermal transport effects. According to classical transport from Section 2.2.1, this should result in heat flow inhibition as well as the introduction of the Righi Leduc effect. The differences in the temperature profile that arises from these thermal transport effects is shown in the following section.

4.3.2 Effect of Magnetic Field on Plasma Temperature

The magnetization of the plasma results in confinement of thermal energy to the laser heated region. This effect is shown in Fig. 4.7. To better illustrate the modification to the temperature profiles from the self-generated magnetic fields, the temperature profiles with self-generated fields are compared to simulations where the magnetic field does not affect the plasma transport and dynamics.

While the plasma is only magnetized to 20%, the thermal energy distribution looks very similar to the unmagnetized case at the same time in Fig. 4.7(b). After nearly a ns of laser heating, there is clear thermal energy confinement in the dense laser heated plasma near the critical surface in Fig. 4.7(c) in comparison to (d). There are steep temperature gradients

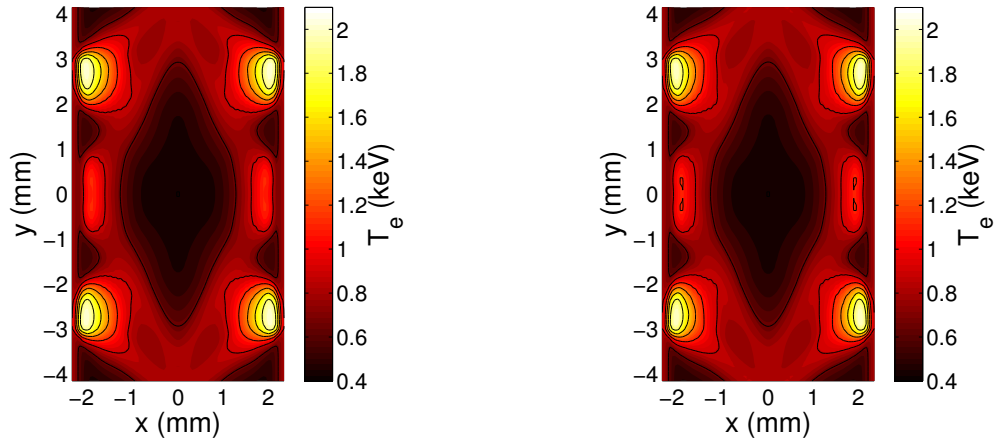

(a) T_e @ $t = 100$ ps with B

(b) T_e @ $t = 100$ ps without B

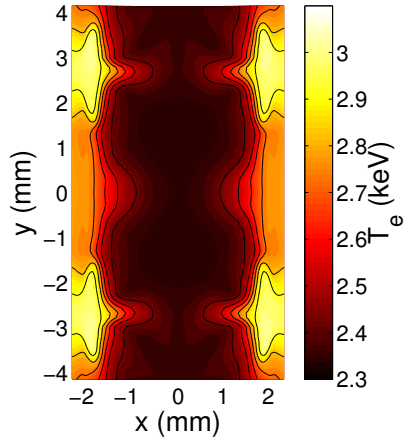

(c) T_e @ $t = 1$ ns with B

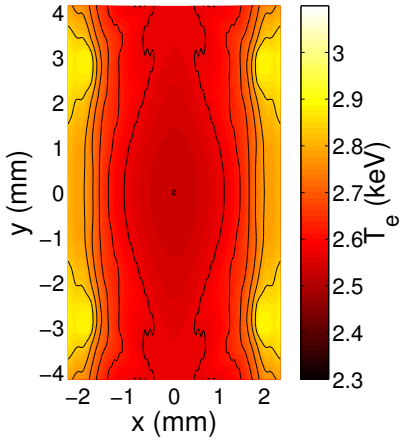

(d) T_e @ $t = 1$ ns without B

Figure 4.7: Temperature profiles 100 ps (a,b) and 1 ns (c,d) into the simulation. (a,c) are the cases where the magnetic field does influence plasma dynamics and (b,d) are the cases where the magnetic field does not influence the plasma

that develop due to the 800 eV difference between the temperature in the laser heated region and the low Z gas fill. These temperature gradients may result in augmented magnetic field generation rate as well as non-local heat flow. Consideration of these effects may be vital to performing accurate modeling of hohlraum implosions as the influence of the electron plasma temperature profile is directly relevant to determining the radiation drive that spurs the implosion.

The evolution of the temperature profile is primarily governed by the heat flow. Examining the effect of the magnetization on the heat flow using a kinetic treatment is useful

towards understanding the evolution of the temperature profiles.

4.3.3 Effect of Magnetic Field on Heat Flow

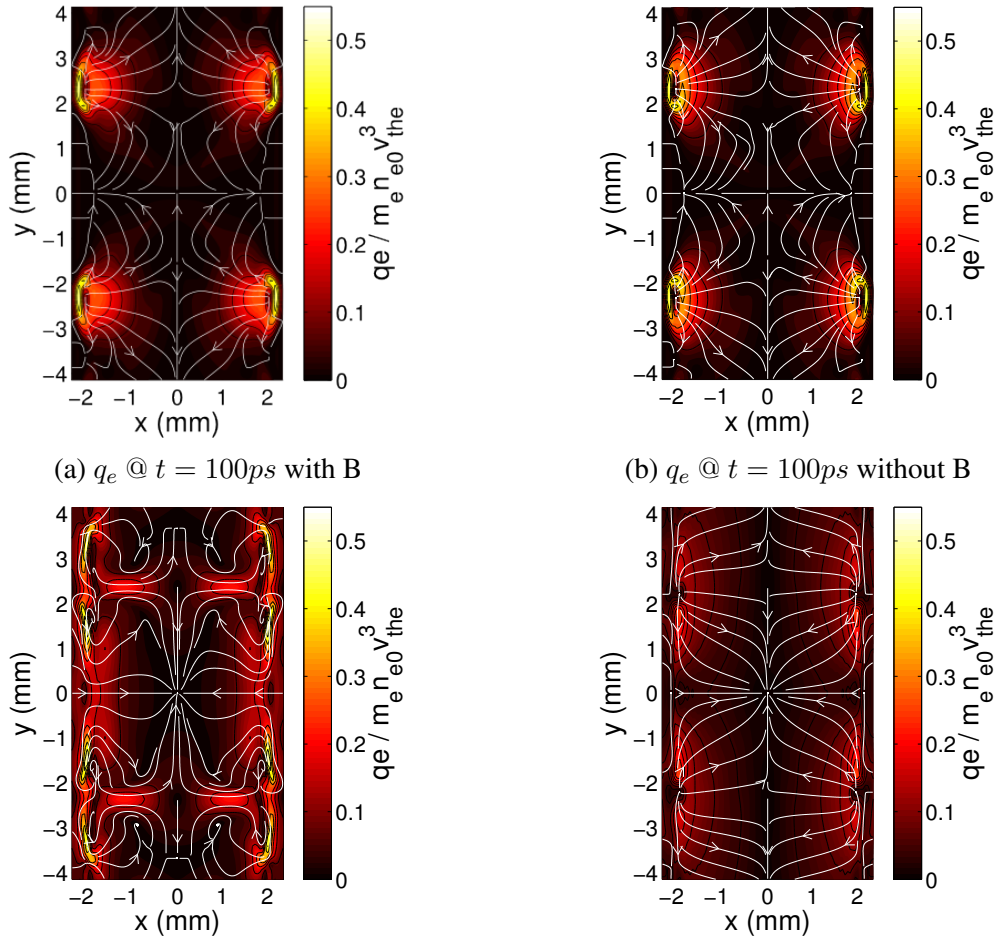

(a) q_e @ $t = 100ps$ with B

(b) q_e @ $t = 100ps$ without B

(c) q_e @ $t = 1ns$ with B

(d) q_e @ $t = 1ns$ without B

Figure 4.8: Heat Flow profiles 100 ps (a,b) and 1 ns (c,d) into the simulation. (a,c) are the cases where the magnetic field does influence plasma dynamics and (b,d) are the cases where the magnetic field does not influence the plasma

The heat flow profiles are illustrated in Figure 4.8. While the profiles in Figure 4.8(a) and (b) are very similar, there is a larger heat flow down the density gradient towards the hohlraum axis in (a) that is non-existent in (b). This is due to restriction of flow along the critical surface, and its redirection by being squeezed through the magnetic fields that have

developed on both sides of it. This effect is amplified significantly in (c). The heat flow jet into the center of the hohlraum from the laser-heated region is evident.

As the plasma becomes magnetized, the Righi Leduc effect gains prominence and deflects the heat flow around the magnetic fields. This results in strong heat flow along the critical surface. The heat flow toward and along the critical surface is absorbed on a smaller length scale than that streaming into the low Z plasma. The confined heating of the critical surface results in a temperature increase near the laser heated regions. In comparison, (d) does not show these directional tendencies and displays generally isotropic heat flow profiles through the hohlraum due to the lack of magnetic field effects. The temperature profile that arises as a result of these deflections in the heat flow influences the magnetic field generation and is discussed next.

4.3.4 Effect of Temperature Profile on Magnetic Field Generation

The self-generated magnetic fields result in a higher temperature at the location of laser incidence by a factor of 7%, and lower temperature by 9% in the region of highest magnetic field, effectively increasing the temperature gradient. Since the magnetic field generation mechanism depends on the temperature gradient, the steepening of the gradient is a feedback mechanism for the magnetic field generation.

This effect is quantified by comparing the magnetic field from the self-consistent treatment against a post-processed calculation of the generated magnetic field from a simulation where magnetic fields are turned off. The latter simulation clearly does not involve the feedback mechanism since the thermal energy does not pile up because it does not respond to the generated magnetic fields. The maximum magnetic field strength and the total magnetic energy is compared for the two simulations and plotted in Fig. 4.9. It shows that the steepening mechanism does not become an important effect till approximately 0.5 ns

since the gradients in both cases are comparable. However, over 1 ns, the total amount of magnetic field generated in the case with the feedback mechanism is approximately twice as much as that generated in the case without magnetic fields influencing the plasma dynamics. Similarly, the maximum magnetic field also incurs a growth by a factor of 2. This is illustrated in Fig. 4.9.

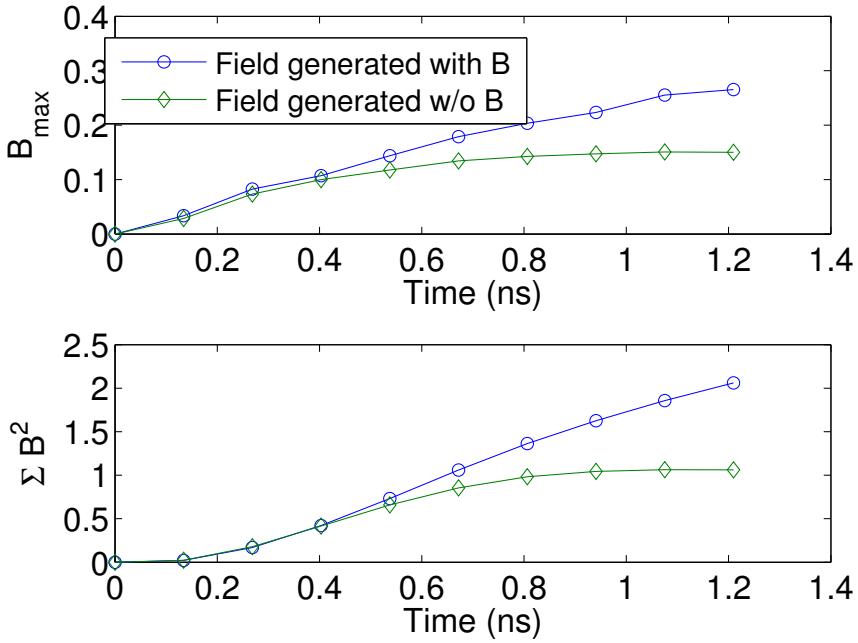

Figure 4.9: Magnitude of (a) maximum and (b) total magnetic field generated in simulations where the magnetic field does and does not influence plasma dynamics.

This suggests that inclusion of a magnetic field generation mechanism, but neglecting the resulting heat flow inhibition and Righi Leduc effect results in a magnetic field that will be half the strength in magnitude and energy. To model magnetic field generation accurately, its full effects on thermal energy transport must be considered self-consistently. Using kinetic modeling, the effect of IB heating on the magnetic field generation mechanism is quantified in the following section.

4.3.5 Effect of Non-Maxwellian Distribution Function on Magnetic Field Generation

Equation (4.4) shows that there is a distribution function dependency on the rate of magnetic field generation. The coefficient for magnetic field generation varies from $0.85 - 1$ as m, the power of the DLM distribution, varies from 2.0. Therefore, a DLM distribution has a smaller field generation rate than that of a Maxwell-Boltzmann. We observe this effect in Fig. 4.10. The different curves are all normalized to the electric field from the code. Individually, they correspond to the different reconstructions of a simple version of Ohm's Law given by

$$E_{\text{non-local}} = \frac{\nabla(n_e\langle v^5\rangle)}{6en_e\langle v^3\rangle}, \tag{4.9}$$

$$E_{\text{local}} = \frac{\nabla P_e}{en_e}, \tag{4.10}$$

$$E_{\text{corrected-local}} = \frac{C(m)5n_e\nabla T_e + 2T_e\nabla n_e}{en_e}, \tag{4.11}$$

where $C(m) = \frac{1}{4}\frac{\Gamma\left(\frac{3}{m(x,y)}\right)\Gamma\left(\frac{8}{m(x,y)}\right)}{\Gamma\left(\frac{6}{m(x,y)}\right)\Gamma\left(\frac{5}{m(x,y)}\right)}\frac{1}{m(x,y)^2 n_e(x,y)}$ and all quantities are dimensionless .

Figure 4.10 shows that the local magnetic field generation mechanism overestimates the rate of field energy generation by a factor of 2. The corrected version of the local Ohm's Law includes the modified magnetic field generation rate that is given in Eq. (4.4) and shown in Fig. 4.2. This is a better approximation of the value of the magnetic field generation rate, overestimating by nearly 50%. The rest of the discrepancy could be due to some kinetic effects that were introduced previously but are more difficult to isolate. The "corrected" model does not account for all non-Maxwellian effects such as the presence of ∇m. In these simulations, as in others [116], there is often a hot Maxwellian tail, suggesting a two temperature effect that could lead to gradients in the distribution function shape. Additionally, Eq. (4.11) does not include the effects of gradients in the distribution

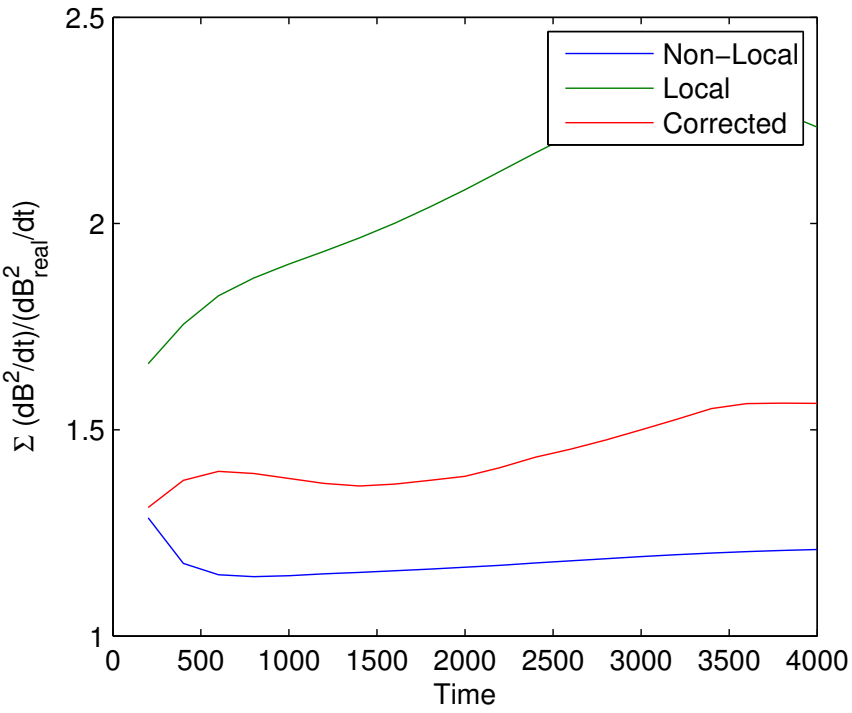

Figure 4.10: $\nabla \times \mathbf{E}$ for different versions of Ohm's Law. The corrected version allows for much better approximation of the true non-local rate.

function caused by IB, which have been shown to contribute towards heat flow in hohlraums [79].

4.3.6 Summary

In this section, using a ray-tracing module coupled to IMPACTA along with NIF hohlraum and laser parameters, results from Vlasov-Fokker-Planck modeling of magnetized plasma dynamics for 1 ns are presented. $\mathcal{O}(10)$ T magnetic fields are generated when a NIF-like laser is incident on a hohlraum wall over a nanosecond timescale. The magnetic fields are strong enough such that $\omega\tau > 1$ in some regions of the dense plasma in the laser-absorption region. The magnetization of the thermal energy carrying electrons results in energy confinement near the critical surface. The magnetic fields deflect the heat flows from the natural path down the temperature gradient. This causes a non-uniformity in

the temperature profile in comparison to that produced without the generation of magnetic fields.

Steepening of the temperature gradient due to deflected heat flows provides a feedback mechanism for magnetic field generation as the magnetic field generation rate is proportional to the gradient of the temperature profile. A post-processed calculation of the generated magnetic field from a simulation where the magnetic field is not included was performed. Comparing the peak magnitude and overall energy of the magnetic field shows a difference of a factor of 2. This can be attributed to the accurate modeling of heat flow in magnetized plasmas resulting in steeper temperature gradients and stronger magnetic fields.

There are severe non-uniformities in electron plasma temperature caused by heat flow inhibition and the Righi Leduc effect. The influence of the Righi Leduc effect leads to heat flow along the critical surface and along with heat flow inhibition from magnetization, the thermal energy is confined near the laser heated regions. The temperature profile from the magnetized plasma shows a significant deviation from the unmagnetized simulations and may be able to explain some of the observed asymmetries in hohlraum implosions due to its effect on radiation drive.

Through this, it is shown that in order to model thermal energy transport in a hohlraum plasma accurately, self-consistent treatment of magnetic fields must be included. Quantifying and modeling non-locality is also important since non-local heat fluxes can modify the thermal and magnetic energy distribution in a plasma. Additionally, laser heating is an inherently non-Maxwellian process that requires careful treatment in order to determine the correct amount of energy received by the plasma. The kinetic modeling performed here self-consistently includes these effects without many approximations to which hydrodynamic models succumb.

CHAPTER 5

Compression and Cavitation of an Externally Applied Magnetic Field in a Hohlraum

5.1 Externally Applied Magnetic Fields

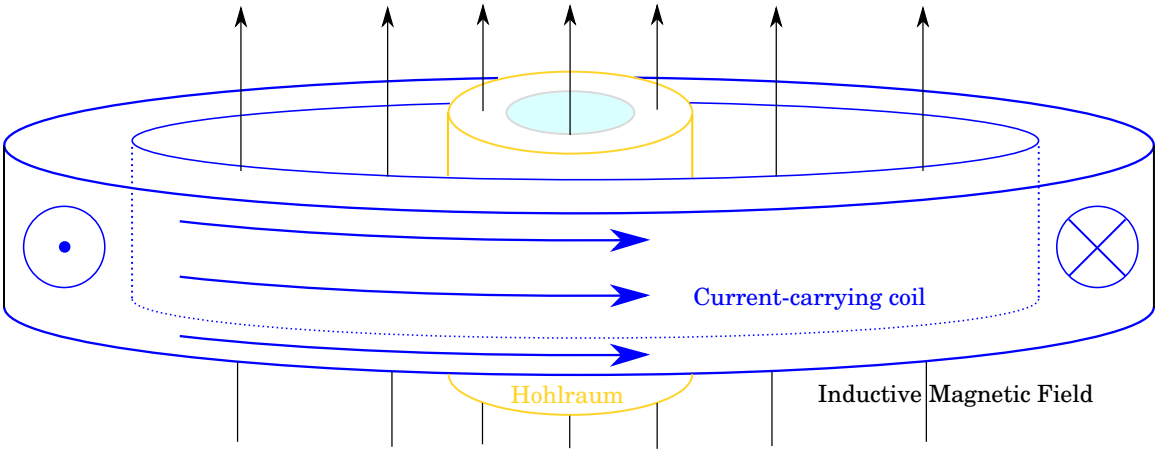

Figure 5.1: Illustration of the principle of the Magneto-Inertial Fusion Electric Discharge System (MIFEDS) device. A hohlraum experiences an axial magnetic field when it is placed at the center of a current loop. MIFEDS produces currents such that a 7.5 T magnetic field is applied axially.

There has been recent interest in the role of applied magnetic fields in ICF plasmas. The Magneto-Inertial Fusion Electric Discharge System (MIFEDS), based on the concept illustrated in Fig. 5.1, has been developed in order to provide steady state magnetic fields for long time-scales relative to the ICF experiments and has been shown to result in in-

creased neutron yield and ion temperatures [117, 118]. A recent experiment on the Omega Laser Facility at the LLE with a 7.5 T external magnetic field imposed on an Omega-scale hohlraum demonstrated a rise in observed temperature along the hohlraum axis [119]. The rise in temperature of the gas fill has been suggested to alleviate some of the parametric instabilities [120] that arise from laser-plasma interactions such as two-plasmon decay and stimulated Brillouin scattering. These instabilities generate supra-thermal, or hot electrons [62, 121] which can travel the length of the hohlraum, and have been shown to be transported towards the fuel capsule [122].

The application of an external magnetic field to hohlraums prompts a rich area of study not only due to the abovementioned applications but also because of the complexities in electron transport of magnetized plasmas that is introduced. In this thesis, this study is motivated by the dynamic relationship between thermal energy transport and the external magnetic field on a hohlraum.

5.2 Modeling Setup

Much like in Chapter 4, a 2-dimensional slice of a hohlraum is modeled in the x-y plane where the y-axis represents the longitudinal axis of the hohlraum and the fuel pellet would sit at the origin. The hohlraum surface is approximated by an almost fully ionized, high Z plasma ($Z_0 = 79$ and $A = 197$) and is located at approximately $x = \pm 800$ μm. The fill is approximated with a moderately ionized high Z plasma, and described by $Z(x, y) = 59.25 + 19.75 \tanh(\frac{x-750}{40})$. The density distribution is given by $n_e(x, y) = (2.98 + 2.93 \tanh(\frac{x-750}{40}))\ 10^{22}/\text{cm}^3$. $T_{e0} = 160$ eV and $\mathbf{B}_0(\hat{y}) = 7.5$ T.

The laser parameters are made to resemble the work in ref. [119]. The ray tracing package tracks the three beam cones that enter at 21, 42, and 59 $^\circ$ from the axis, to their respective refraction points and allows for some reflection. The rays and the initial heating

profile are shown in Fig. 5.2a. Fig. 5.2b shows the temperature profile after 300 ps of laser heating. Figure 5.2c shows the cavitation and amplification in the in-plane magnetic field profile caused by intense laser heating. The Nernst flow, in Fig. 5.2d, flows down $\pm\hat{x}$ of the temperature gradient of the laser heated region. Through the rest of this chapter, we show that the Nernst flow is responsible for the magnetic field profile seen in Fig. 5.2c.

5.3 Results

Given the geometry, the generation terms from Eq. (2.77) do not produce magnetic fields in the $\hat{y}$ direction. Therefore, the only dynamics that can be expected for the externally applied magnetic field are magnetic diffusion through the resistivity term, and magnetic field transport through the plasma bulk flow, currents, and the Nernst effect. In the following section, we examine the effects of the various field transport terms and ignore the magnetic diffusion effects due to a relatively large Magnetic Reynolds number signifying a regime where magnetic diffusion is relatively unimportant.

In order to elucidate the various field transport effects, careful modeling of the heat flow that will affect the magnetic field must be performed. The geometry in this chapter is slightly different than in the previous chapter. An OMEGA hohlraum is smaller than a NIF hohlraum by approximately a factor of 3 in both directions and the laser heating profile also differs. Therefore, the following section illustrates kinetic effects that are prevalent in the heat flows in an OMEGA hohlraum that may alter the dynamics of an externally applied magnetic field.

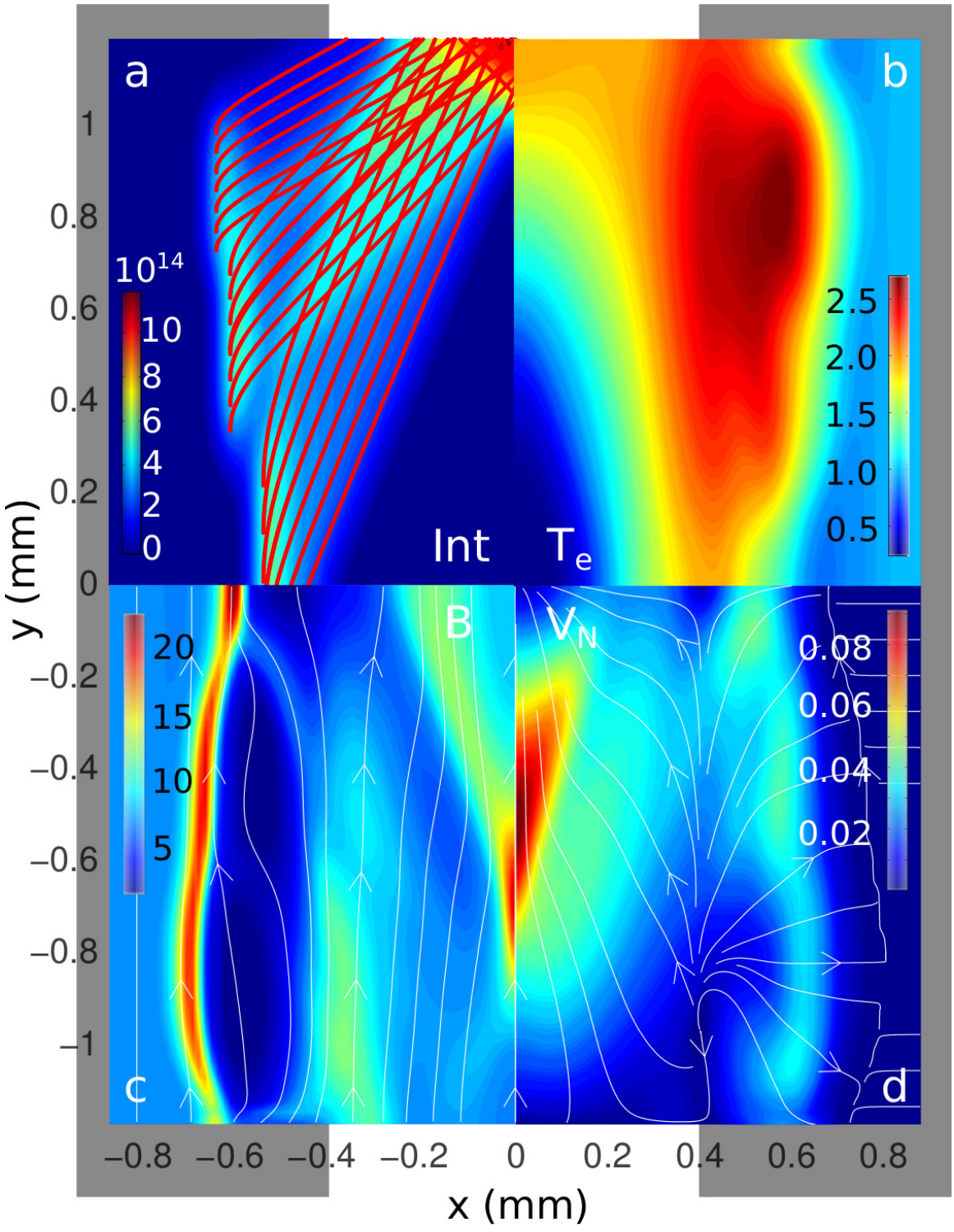

Figure 5.2: (a) Ray tracing profile overlaid onto laser intensity profile (W/cm^2) at t = 0. (b) Electron Plasma Temperature (keV), (c) Externally applied magnetic field (T), (d) Nernst Velocity ($v_N/v_{\text{th}0}$) at t = 250 ps.

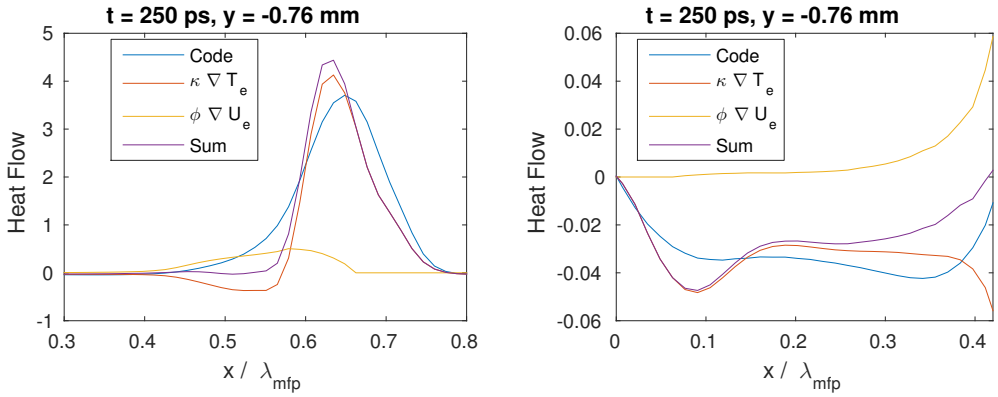

(a) Heat flow away from axis

(b) Heat Flow towards axis

Figure 5.3: The heat flow from the code is compared to that calculated by classical transport and super-Gaussian transport. $\phi\nabla U_e$ contributes a 10% correction to the total heat flow flowing away from the hohlraum axis into the wall. However, the heat flow towards the axis is non-local and not adequately described by either of the approximations.

5.3.1 Heat Flows

5.3.1.1 Anomalous Heat Flow

As discussed in Section 2.2.2, inverse Bremsstrahlung heating of the plasma results in a DLM electron distribution [74], which consequently modifies the transport coefficients [65, 78] and even introduces new terms including an anomalous heat flux up a pressure gradient $\mathbf{q}_n$, represented by the last term in the heat flow equation from Eq. (2.67). The heat flow equation is

$$\mathbf{q}_e = -\frac{T_e}{e}\underline{\underline{\psi'}} \cdot \mathbf{j} - \underline{\underline{\kappa}} \cdot \nabla T_e - \underline{\underline{\phi}} \cdot \nabla P_e;, \tag{5.1}$$

where ψ, ϕ and κ are transport coefficients as described in ref. [78]. $\mathbf{q}_n$ increases as $m > 2$ increases, where m is the power of the DLM distribution function defined by Eq. (2.64).

In these simulations, m reaches a maximum of 3.1 near the centers of the laser heated regions, but varies spatially and temporally thus requiring the preservation of the distribution function at each point throughout the simulation for accurate calculation of the heat flow. Using the theory detailed in refs. [65, 78], the heat flow can be modified in

a hydrodynamics code to include this effect. However, the distribution is not precisely a super-Gaussian due to other effects such as non-locality and therefore this fix remains an approximation.

We examine relative magnitudes of the real heat flow, and the classical heat flow calculated using all three terms that form the full post-processed heat flow from Eq. (5.1) that includes anomalous heat flow. Calculation of the anomalous heat flow as a function of the best-fit distribution function, table look-up, and pressure gradient shows that there is heat flow into the hohlraum wall and approximately performs a 10% correction to the diffusive heat flow i.e. $\kappa\nabla T_e$. This is shown in Fig. 5.3.

The anomalous heat flow naturally influences regions of high internal energy gradients. Figure 5.3a shows that the anomalous heat flow corrects the heat flow predicted by $\kappa\nabla T_e$ by 10% near 0.6 mm. The code predicts a smooth increase in heat flow into the wall, even in regions of opposite temperature gradients where the red line is negative. The super-Gaussian anomalous heat flow accounts for some but not all of this. This suggests the existence of a non-local version of the anomalous heat flow.

In fact, the clear discrepancy between the heat flow from the code and the transport approximated heat flow as a whole may be explained by non-locality. Classical transport overestimates the heat flow at the maximum point, as it should, and underestimates farther from the gradient, where the heat flow carrying electrons actually deposit their energy. The heat flow near 0.7 mm is therefore underestimated by classical transport. The particulars of non-local heat flow for these simulations is discussed next.

5.3.1.2 Non-Local Heat Flow

A majority of the disagreement between the heat flow from the code and the heat flow from the post-processed modified classical transport theory is due to the strongly non-local heat flow that is prevalent in the hohlraum. Figure 5.4b shows a 2D profile of a metric

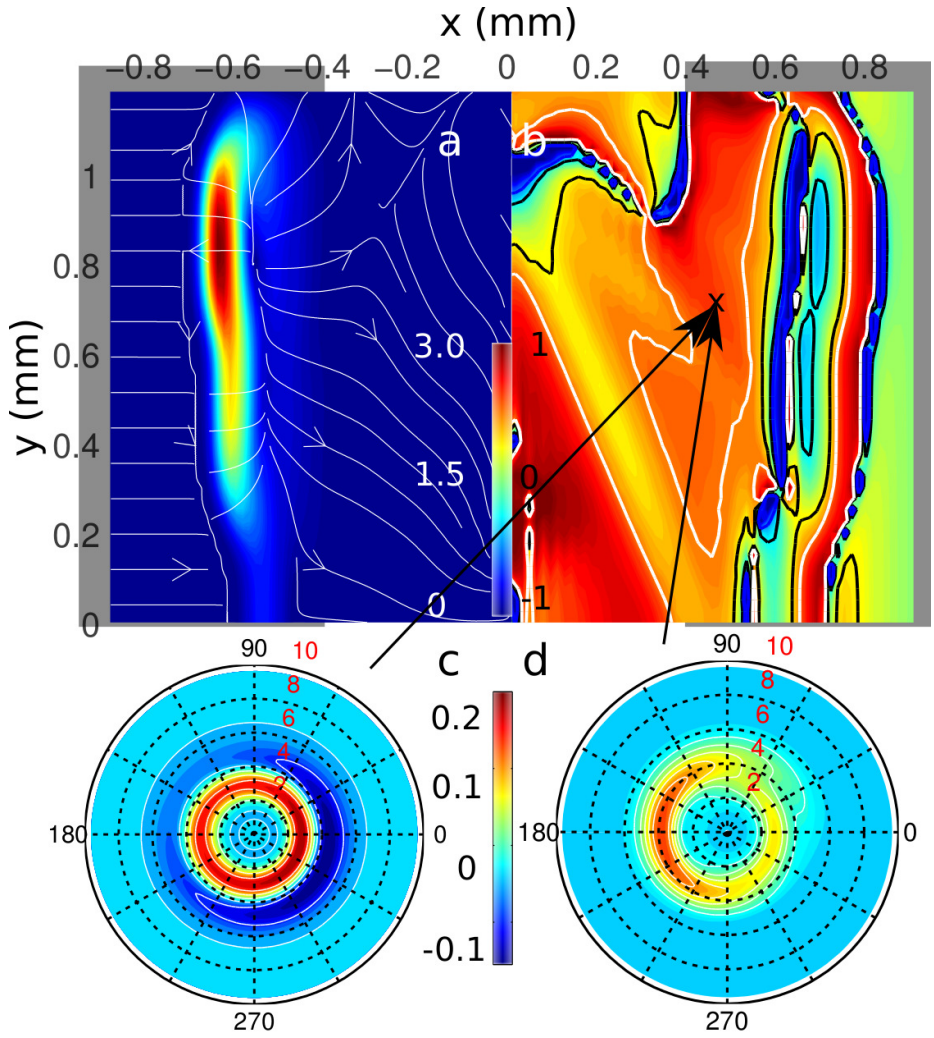

Figure 5.4: (a) Heat flow (b) $1 - q_{\text{Eq. (5.1)}}/q_{\text{code}}$ (c) $v^5(f_{\text{code}} - f_{\text{MB}})$ (d) $v^5(f_{\text{code}} - f_{\text{SG}})$ @ $x = 0.44$ mm, $y = -0.61$ mm, $m = 2.625$, $t = 100$ ps.

for quantifying the magnitude of the discrepancy between the two heat flows. Described by $1 - q_{\text{Eq. (5.1)}}/q_{\text{code}}$, this ranges from -1 to 1. The blue and yellow are regions of $\pm 25\%$ agreement between the two heat flows. The red regions correspond underestimation by the classical heat flux while the blue regions correspond to it's overestimation. Heat flow from regions near the temperature hotspots is overestimated by the classical calculation while the heat flow further away from the hotspots is underestimated, as expected from the existence of non-locality. Due to the laser heating, the mean free path of the hot electrons is increased and the parameter $\lambda_{\text{mfp}}/L < 50$ suggesting that non-local heat flow becomes prevalent in

the laser heated region.

Examining the distribution function in Fig. 5.4c shows the significance of inverse - bremsstrahlung heating. Since $\mathbf{q} \propto \int_0^\infty v^5 \; f(\theta, v) \; dvd\theta$, the contribution to the total heat flow from an angular part of the distribution is described by $v^5 f(\theta, v)$. $v^5(f - f_{\text{Maxwell}})$, therefore, represents the difference in the contribution to the heat flow from the two distributions. Figure 5.4c shows that the contribution is enhanced in the region of $2 - 4 \; v_{\text{th}}$, and suppressed in the region of $4 - 6 \; v_{\text{th}}$, which is characteristic of inverse-bremsstrahlung heating. Calculating the heat flow contribution difference between the real distribution and the best-fit super-Gaussian ($m = 2.2$ in this case), shows that the inverse-bremsstrahlung model does not replicate the distribution function fully due to the non-local effects. The enhanced tail and shifted center in the 180° direction is characteristic of the non-local heat flow down the hohlraum wall while the colder return flow is a result of the features in the 0° direction.

The dynamics of the externally applied magnetic field are equally rich and complex, and the interplay between these kinetic thermal energy transport effects and magnetic field dynamics is discussed in the following section.

5.3.2 Magnetic Field Dynamics

Over 0.5 ns, the simulation shows that there is magnetic field cavitation on the hohlraum axis and compression in the hohlraum wall due to the energy deposition from the laser. Pile-up of the magnetic flux results in a 25 T magnetic field, more than 3 times the strength of the initial 7.5 T field.

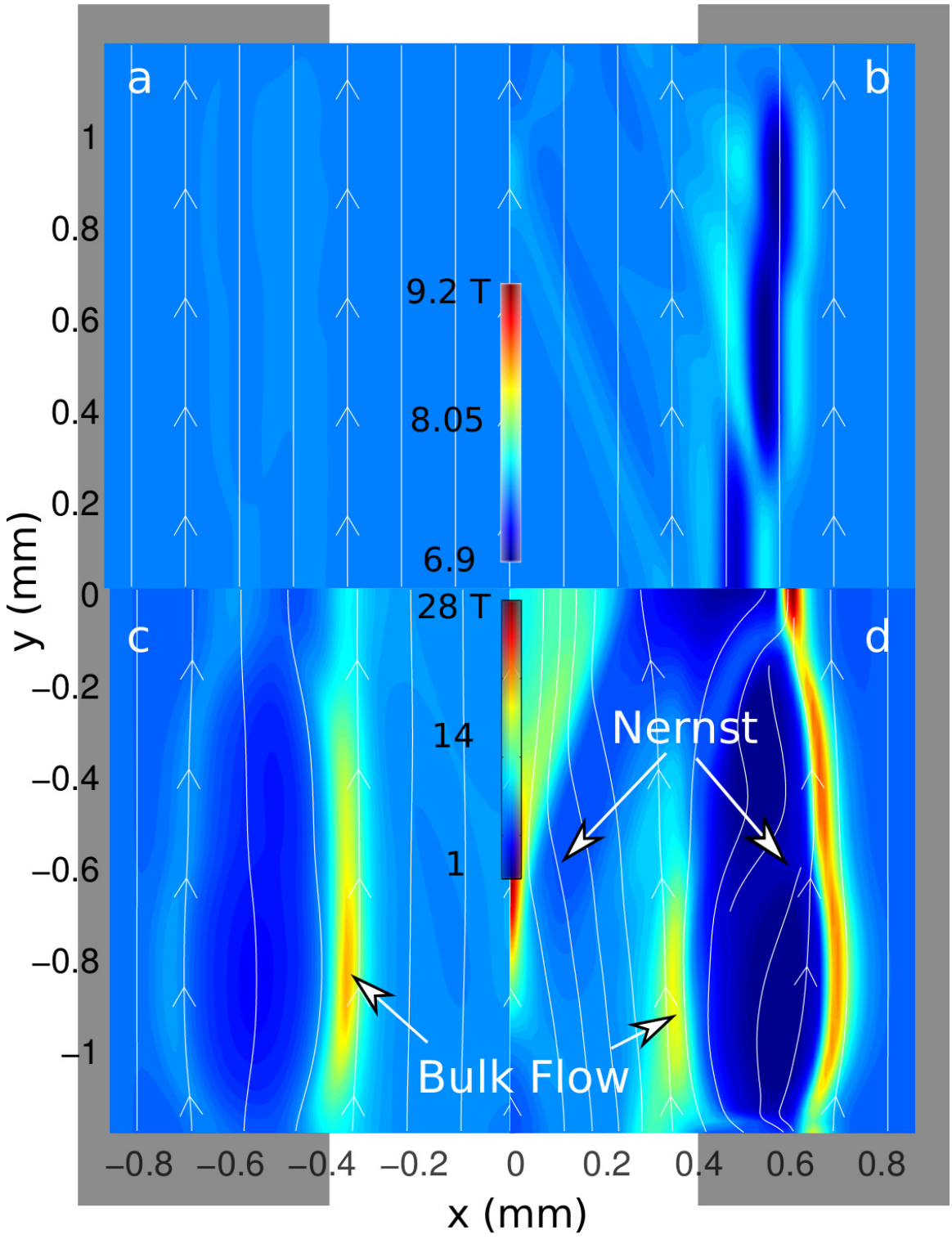

Figure 5.5: Magnetic field after 50 ps with only plasma bulk flow (a) and full Ohm's Law (b). Magnetic field after 400 ps with only plasma bulk flow (c) and full Ohm's Law (d)

5.3.2.1 Cavitation

In order to determine the effect of Nernst advection on the magnetic field evolution, simulations with and without the $\mathbf{B} \times \mathbf{f}_1$ term in the $\mathbf{f}_1$ equation were compared. This term is responsible for the interaction of kinetic electrons with the magnetic field as is illustrated by the procedure performed to obtain Eq. (2.77). It represents the Nernst effect in Ohm's Law as well as the Righi-Leduc effect in the heat flow equation. The magnetic field after 50 ps without and with full Ohm's Law treatment is shown in Fig. 5.5a and Fig. 5.5b, respectively. The laser heated region results in magnetic field cavitation in both cases but the magnitudes differ. It is not evident in Fig. 5.5a since the field is only modified by a few percent by the plasma bulk flow. Thermal energy transport results in a more noticeable change immediately over 50 ps.

The relevant time-scale for the plasma bulk flow to travel to the center of the hohlraum (with the magnetic field in tow) is given by, $\frac{r_H}{C_s} \approx \frac{r_H}{\sqrt{k_B T_e / M_i}} \approx 2$ ns. Figure 5.5d shows that including the Nernst effect results in magnetic field cavitation on a faster time-scale than can be expected due to field advection only through bulk plasma flow in Fig. 5.5c. In the case of a 7.5 T initial field strength, the magnetic field on the axis grows to 30 T within 0.5 ns. Figure 5.5d also shows that the magnetic flux pile-up in the hohlraum wall occurs due to the Nernst effect. The field increases to a strength of nearly 25 T in the hohlraum wall.

Figure 5.6a shows the results of the magnetic field cavitation study for increasing field strengths suggesting that as

$$\lim_{B_{y0} \to \infty} B_{y-\text{axis}} / B_{y0} = 1.$$

As predicted by ref. [65, 106], the Nernst velocity decreases due to the increase in magnetization. The decrease in Nernst velocity towards the hohlraum axis results in a decrease of magnetic field transport.

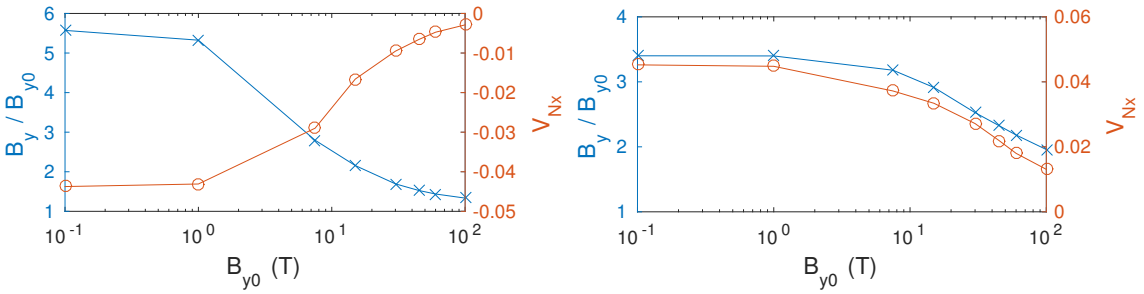

(a) On-axis (b) Wall

Figure 5.6: Magnetic field cavitation (a) and compression (b) for different magnetic field strengths. As field strength is increased, the Nernst advection mechanism is mitigated. This results in suppression of cavitation as there is negligible field pileup for a 100 T field but the advection into the wall is not so strongly affected and can result in the effective doubling of a 100 T field in the hohlraum wall.

5.3.2.2 Compression

The degree of magnetic flux pile up in the hohlraum wall, however, is not so strongly affected by the increase in magnetic field strength because $\omega\tau \propto n_e^{-1}$. Figure 5.6b shows that the magnitude of maximum field strength in the wall ranges from $2 < B_{\mathrm{y}}/B_{\mathrm{y0}} < 3$ for $1 < B_{\mathrm{y0}} < 100$ T. Of possible significance is the fact that an initial 100 T field can be augmented to a strength of 180 T within 300 ps from Omega-like laser heating.

5.3.2.3 Effect of Non-locality on Magnetic Field Evolution

The existence of non-local heat flow necessarily dictates the non-local Nernst convection. Figure 5.4b shows that while non-locality occurs throughout the hohlraum, it is prevalent in the low-Z gas fill. The heat flow in the gas fill is responsible for transporting the magnetic field towards the hohlraum axis and therefore, it is reasonable to expect the non-local heat flow to contribute towards magnetic field transport. The fact that the Nernst velocity is dependent on a higher order moment of the distribution function only serves to reinforce the importance of non-local advection of magnetic field.

The non-local effects of Nernst convection are studied by comparing the Nernst velocity

calculated by Eq. (2.88) and Eq. (2.89) where the classical heat flow in Eq. (2.88) is $q_e = \kappa \nabla T_e$. Therefore, the calculation from the classical approximation does not encompass the non-local effects of the plasma.

The discrepancy between the non-local Nernst velocity and the local approximate version is illustrated in 2D profiles of v_N calculated from the code and those calculated from the classical approximation in Fig. 5.7a and Fig. 5.7b.

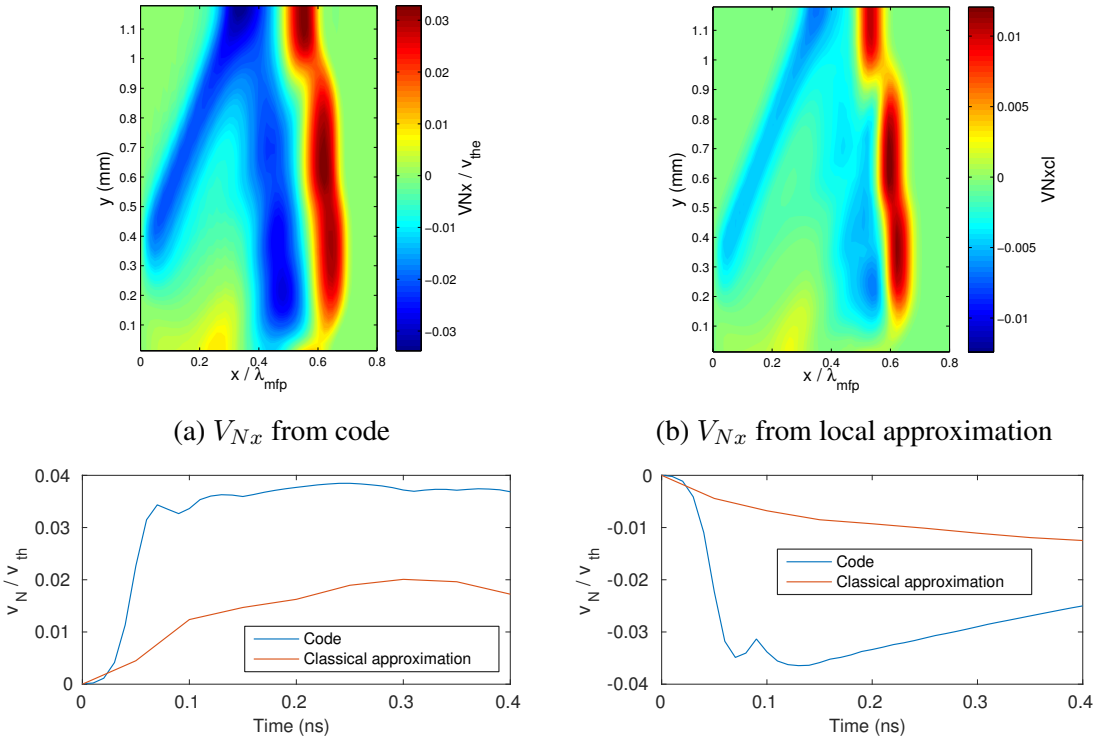

(a) V_{Nx} from code

(b) V_{Nx} from local approximation

(c) V_{Nx} towards hohlraum wall

(d) V_{Nx} towards hohlraum axis

Figure 5.7: (a) The Nernst velocity calculated from the code is compared with that (b) from the approximate relation provided by Eq. (2.88). (c,d) show this comparison over time. All 4 plots show that the classical approximation to the Nernst velocity fails in a hohlraum. This is especially relevant for the flow towards the hohlraum axis because the discrepancy is larger, and the result is faster transport of the magnetic field.

In Fig. 5.7c and Fig. 5.7d, the magnitude of the calculated Nernst velocity is clearly larger than that calculated through a post-processed approximation of $\mathbf{v}_N \approx 2\kappa \nabla T_e / 5P_e$. Consider that this approximation includes the non-local contribution to P_e and therefore,

more accurate than that which a classical code might reproduce. However, we have already determined that since $\kappa \nabla T_e$ is lacking, the v_N calculation will be similarly lacking in the non-local component, but will also include the relevance of the higher order moment that the Nernst velocity requires in comparison to the heat flow moment. Due to these effects, the Nernst velocity of the code differs from the approximate calculation by at least a factor of 2. This discrepancy is much larger for the primarily non-local flow towards the hohlraum axis.

5.3.3 Influence of B_y on T_e

One of the motivations for placing an external magnetic field on a hohlraum is to inhibit thermal conduction losses from the fuel capsule. In the context of the laser-heated plasma region, the inhibition of thermal transport in the $\hat{x}$ direction results in thermal energy confinement at the hohlraum walls, as suggested in [119]. Their observation that the temperature increases due to the imposition of a magnetic field is supported by HYDRA simulations that include Laser Entrance Hole (LEH) material and "frozen-in-flow" calculations. HYDRA shows that the magnetic field collimates the LEH plasma onto the hohlraum axis and results in a higher temperature.

Performing these same simulations without LEH material in IMPACTA shows that the thermal energy is confined to the dense high Z plasma near the critical surface of the hohlraum wall. Due to this confinement, the low Z fill is actually at a lower temperature than it would be without an external axial *magnetizing* magnetic field. This effect is shown in Fig. 5.8. In Fig. 5.8(a), the imposition of a 7.5 T field causes a small increase in thermal energy along the hohlraum wall. With no external field, this thermal energy flows down to the center of the hohlraum towards the axis resulting in a 700 eV increase in electron plasma temperature. Figure 5.8(b) shows a 300-600 eV electron plasma temperature

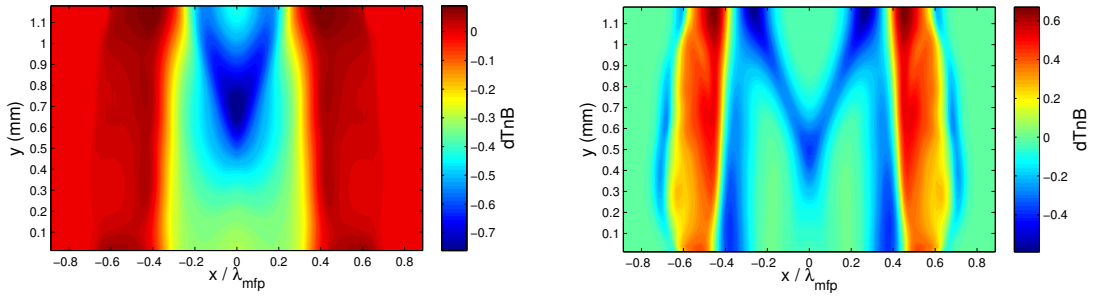

(a) 7.5 T vs 0 T

(b) 60 T vs 7.5 T

Figure 5.8: (a) shows the difference in electron plasma temperature when a 7.5 T MIFEDS-like field is imposed. The walls retain much of the thermal energy that flows down into the gas fill. The gas fill is significantly cooler. (b) shows this effect is very much exaggerated when a 60 T field is imposed in comparison to a 7.5 T field because the electrons are magnetized immediately. Temperature differences are in units of keV.

increase near the critical surface. The thermal energy responsible for this increase appears to be withdrawn from the low Z plasma. Not coincidentally, this is the same region over which the magnetic field accumulates near the hohlraum axis in the $7.5T$ field. This suggests that imposing a 60 T field would prevent field accumulation on the axis over the same time-scale.

The heat flow in the radial direction, $\hat{x}$ in this geometry, is inhibited due to the externally imposed magnetic field. Using the classical transport interpretation, $\kappa_{\perp}$ decreases as the magnetization increases resulting in the inhibition of perpendicular heat flow. The parallel heat flux remains unaffected. This results in most of the heat flow becoming parallel to the magnetic field axis, an effect shown in Fig. 5.9 (a-d). The inhibition of perpendicular heat flow is what results in the increase in thermal energy near the hohlraum wall.

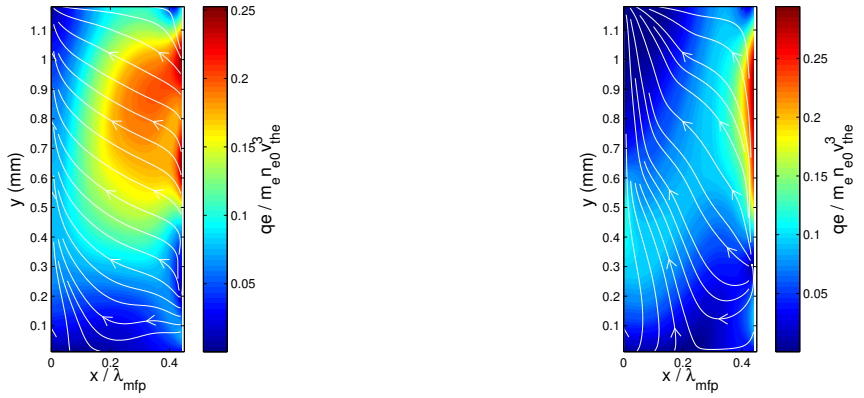

(a) 0 T

(b) 7.5 T

(c) 30 T

(d) 60 T

Figure 5.9: (a) The heat flow without an external magnetic field (b)-(d) Increasing magnetic field strength results in heat flow confinement in the $\hat{y}$ direction.

5.3.4 Summary

This chapter discussed Vlasov-Fokker-Planck-Maxwell (VFPM) simulations of a magnetized hohlraum scale plasma including ray-tracing of an Omega-like laser configuration over a nanosecond time-scale. With the use of IMPACTA, the effect of non-equilibrium electron kinetics on thermal energetic and magnetic field dynamics of a LLE hohlraum with an externally imposed 7.5 T magnetic field is displayed. We found that significant proportions of the total heat flow are non-local. Additionally, the presence of inverse bremsstrahlung heating results in anomalous heat flow towards the over-dense plasma of the hohlraum

wall. Therefore, the diffusive heat flow from the laser-heated regions is not an adequate description of the thermal energy dynamics. The heat flows from the laser heating move the externally imposed magnetic field through Nernst convection. To examine the effects of Nernst convection in relation to the plasma bulk flow, we showed modeling without an electron contribution to the transport of magnetic field in Ohm's Law.

Magnetic field transport due to Nernst flow results in significantly faster field cavitation than that which occurs as a result of plasma bulk flow. Magnetic field cavitation occurs due to heat flow down the density and temperature gradient, which is shown to be non-local. Retention of the distribution function allows for accurate modeling of the magnetic field cavitation because the local approximation to the Nernst velocity underestimates the true convection velocity by a factor of 2. Nernst flow into the over-dense region causes magnetic flux pile-up at the walls and results in magnetic field amplification by a factor of 3. Magnetic flux pile-up does not occur with only plasma bulk flow present as there is a negligible amount of plasma bulk flow toward the wall from the laser heated region.

We have shown Vlasov-Fokker-Planck modeling of an external magnetic field of 1-100 T imposed upon a hohlraum. Magnetic flux pile-up causes an increase in magnetic field magnitude by a factor of 3 for a 7.5 T magnetic field. Additionally, the heat flow is responsible for magnetic field cavitation on a faster time-scale than that from the bulk flow of the plasma. Not only is the heat flow strongly non-local, it also has distinct signatures of inverse bremsstrahlung heating. The ability to preserve distribution function information through use of a kinetic code allows to model the heat flow accurately. Full Vlasov-Fokker-Planck treatment of the problem enables accurate modeling of magnetic field dynamics due to the implicit thermoelectric terms containing the non-local effects in the $\mathbf{f}_1$ equation. It is shown that the Nernst flow is the dominant mechanism for magnetic field transport and is responsible for the increase in field strength, up to 100 T for a initial 100 T field, in the wall as well as transport of the magnetic field towards the hohlraum axis. The magnetic

field transport is mitigated at higher field strengths as expected.

The thermal energy is confined to the critical surface of the hohlraum because of the external magnetic field. The axial magnetic field causes inhibition of perpendicular heat flow and prevents thermal energy transport to the hohlraum axis resulting in lower temperatures in the gas fill for increasingly higher magnetic field strengths. The loss of thermal energy in this region corresponds to the increase in thermal energy near the laser critical surface on the plasma near the hohlraum wall.

CHAPTER 6

Heat Flux Mediated Magnetic Reconnection

6.1 Background

Magnetic reconnection is a prominent phenomenon in astrophysical systems such as the magnetosphere and the solar corona [91] and has been recently recreated in laser-plasma experiments [52, 53, 54]. Similar geometries are formed in hohlraums by nearby laser spots.

In heating plasma with a finite laser spot, an azimuthal magnetic field about the heated region arises through the Biermann battery effect [88] as discussed in Section 2.3.2 and shown in Chapter 4. For multiple spots in close proximity, these magnetic fields will be in a configuration with oppositely directed field lines. Under such conditions, reconnection of magnetic field lines may occur.

Under conditions similar to those found in hohlraums, where heat flux effects in Ohm's law are important, it can be shown that reconnection of field lines can also occur but by a different mechanism than those in literature. The heat fluxes that are generated by the laser hot-spots drive reconnection through advection at the Nernst velocity v_N. The Nernst effect allows magnetic field advection without an associated electron current, which is different than the standard Hall effect within the reconnection layer; this breaks the Alfvenic constraint (at least within the parameters considered) and allows characteristic reconnec-

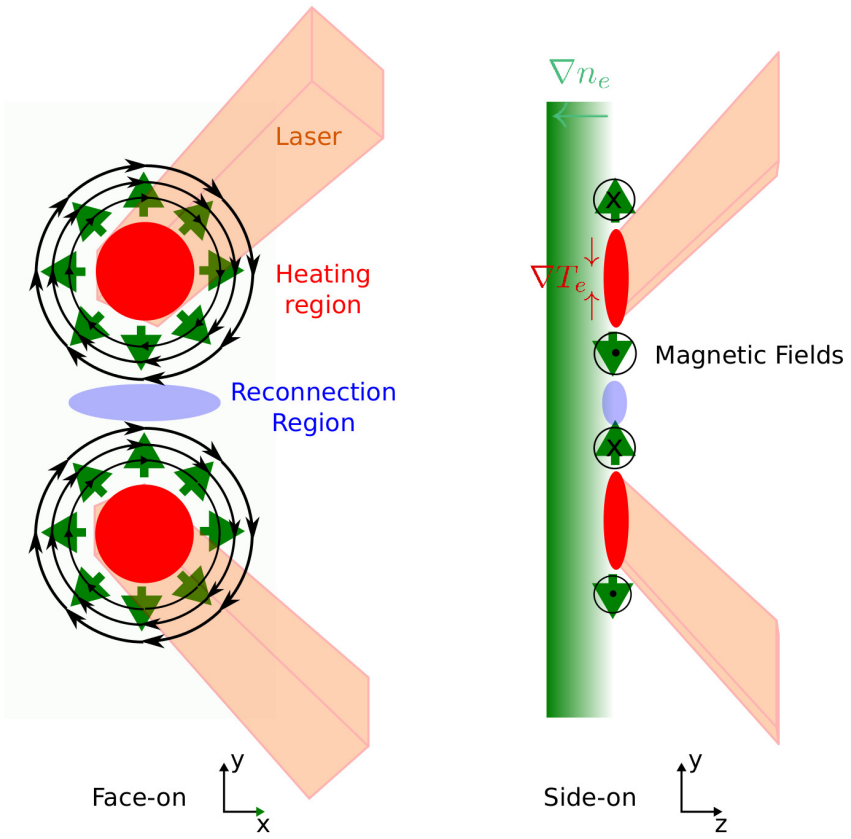

Figure 6.1: Magnetic reconnection geometry from neighboring laser spots (a) shows the face on view that illustrates the reconnection geometry and (b) the side on view helps illustrate the magnetic field generation mechanism that arises due to the laser heating.

tion rates of $E_z/(B_0 v_T)$ rather than $E_z/(B_0 v_A)$. This can be shown to occur for conditions described by a dimensionless number describing the ratio of Nernst to electron flow velocities. The dimensionless number indicates that this mechanism is only relevant in a high β plasma, i.e. where the ratio of thermal pressure to magnetic pressure is large. However, the Hall parameter $\omega_c \tau_{ei}$ can be large even for $\beta > 1$ so that thermal transport is strongly modified by magnetic fields, which can impact longer time scale temperature homogeneity and ion dynamics.

In order to discuss the differences between reconnection in semi-collisional plasmas and those previously studied, the prior models for magnetic reconnection need introduction.

6.1.1 Resistive Reconnection

Fundamentally, magnetic reconnection relies on two mechanisms; one to move the magnetized plasma in and out of a certain region where the field lines may reconnect, and the second to result in topological changes in the magnetic field alignment in the region where the opposing field lines are brought together. Figure 6.2 illustrates this process.

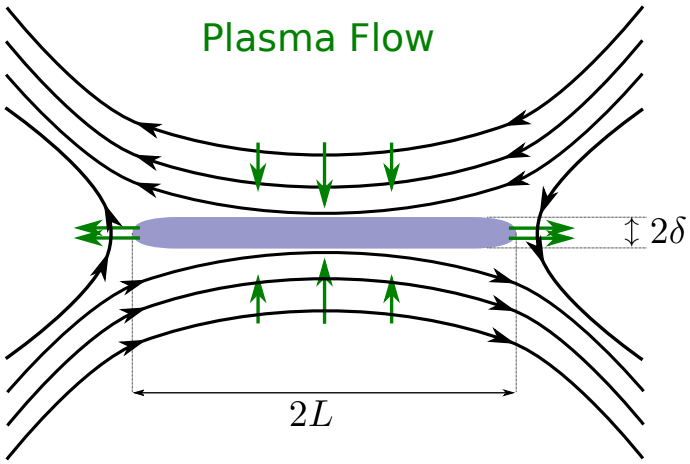

Figure 6.2: The fundamental requirements for magnetic reconnection are shown. An inflow of magnetic field into a diffusion region of width 2δ and length $2L$ from which reconnected magnetic field lines emerge with plasma outflow.

The process can be described by the resistive-magnetohydrodynamics (MHD) Ohm's law that gives the *out-of-plane* electric field,

$$E_z = -\mathbf{C} \times \mathbf{B} + \eta j_z, \tag{6.1}$$

that governs the time evolution of the in-plane magnetic fields. As discussed in Section 2.3, the magnetic field can be transported by the bulk flow of the plasma. In resistive reconnection, the plasma is brought in towards the resistive layer by the bulk flow. In the resistive layer, the field lines reconnect and the magnetic field is then ejected outwards with the plasma. Since the outflow is attributed to magnetic pressure and the outflow velocity is the Alfven velocity, $v_A = \sqrt{B^2/2\mu_0 m_i n_i}$. The inflow velocity can be found by considering

that the convective electric field from frozen-in-flow is balanced by the resistive electric field. Therefore,

$$\begin{aligned} v_{\text{in}} B_{\text{in}} &= \eta j_z, \\ &= \eta \frac{B_{\text{in}}}{\delta \mu_0}, \\ v_{\text{in}} &= \frac{\eta}{\delta \mu_0}. \end{aligned}$$

The reconnection rate is $v_{\text{in}}/v_A = \delta/L = \sqrt{\eta}\mu_0 L v_A = S^{-1/2}$ where S is the Lundquist number, the ratio between Ohmic diffusion time $\tau_{\text{diff}} \equiv L^2/\eta$ and global Alfven time $\tau_A \equiv L/v_A$. The width of the region is $\delta = LS^{-1/2} = \delta_{\text{SP}}$, and suggests that reconnection occurs over distances smaller than δ_{SP}. This is the first mechanism for reconnection, proposed by Parker [123] & Sweet [124], that consistently discussed the macroscopic behavior and this regime of reconnection has been identified experimentally [125]. In most astrophysical systems, S is large and Sweet-Parker reconnection is too slow to explain observations. To reconcile these differences, the importance of two fluid effects in magnetic reconnection was proposed.

6.1.2 Hall Reconnection

On small enough scale lengths, two fluid effects in MHD are important where the electrons must receive separate consideration from the ions. In case of a small diffusion region for which the Sweet-Parker width, δ_{SP}, is smaller than the ion inertial length, c/ω_{pi}, the electron fluid effectively decouples from the ions and the ion velocity goes to 0.

Over such small scales, the contribution to Ohm's Law from the electron fluid has to be added in the form of current (since $v_i \neq v_e$, $j = en(v_i - v_e) \neq 0$ and the electron pressure

tensor. The new Ohm's law is given by

$$E_z = -\mathbf{C} \times \mathbf{B} + \eta j_z - \frac{\mathbf{j} \times \mathbf{B}}{e n_e} + \nabla \cdot \underline{\underline{\Pi_e}} \tag{6.2}$$

Again, an illustration explains this concept very well and is provided in Fig. 6.3.

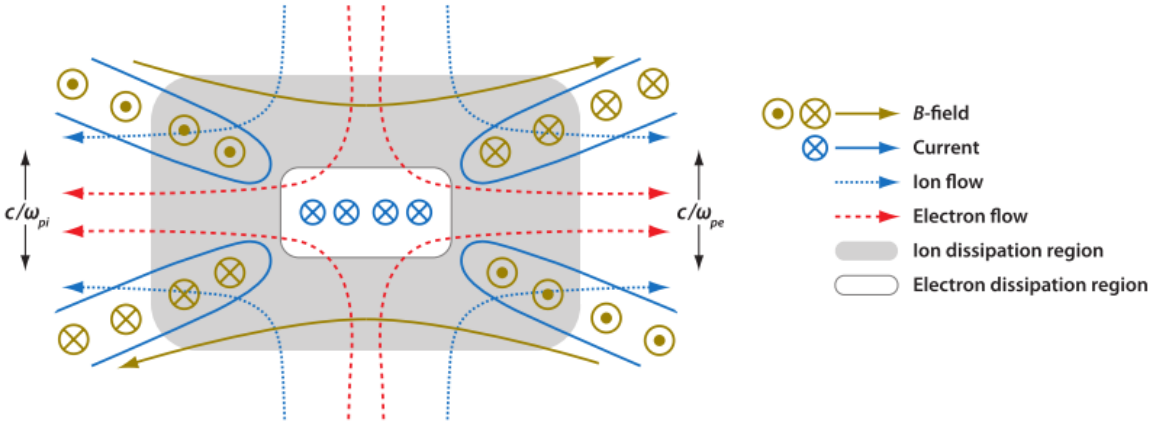

Figure 6.3: The length scales associated with two fluid effects required for Hall reconnection are illustrated. Figure from Zweibel and Yamada [91].

Much like in the mechanism proposed by Sweet-Parker, the plasma transports the magnetic field to the reconnection region. Once the plasma is within the ion dissipation region, which is approximately the size of the ion skin depth, the electrons are effectively decoupled from the ions. The magnetic field is transported further into the dissipation region by the Hall current. This mechanism becomes important when $\delta_{\text{SP}} < \delta_i$ i.e. when

$$\frac{\delta_{\text{SP}}}{\delta_i} = \left(\frac{L}{\lambda_{mfp}}\right)^{1/2} \left(\frac{m_e}{m_i}\right) < 1. \tag{6.3}$$

This suggests that the Hall effect becomes important when the length of the current sheet is comparable to the electron mean-free-path. Because of this, Hall reconnection is also called collisionless reconnection.

The electron dissipation can be supported by resistivity or the electron pressure. In ideal

MHD, i.e. collisionless MHD, the collisionless pressure tensor is the only term that can support the electric field, E_z, in the reconnection region. The contribution from anisotropic pressure is from the following off-diagonal terms in the pressure tensor [94, 96]:

$$E_{z-\Pi} = \frac{\partial P_{xz}}{\partial x} + \frac{\partial P_{yz}}{\partial y}, \tag{6.4}$$

and has been experimentally measured [126]. Collisionless reconnection is particularly relevant because not only are the plasmas collisionless in the planetary magnetosphere where reconnection may occur [127] but also because two fluid effects are essential to study electron acceleration that has been attributed to magnetic reconnection [128, 129]. The inclusion of Hall physics suggests that the dynamics at such small scale lengths contribute strongly to reconnection.

6.1.3 Semi-Collisional Reconnection

This theory can be extended for a semi-collisional system described by the VFPM equations. The generalized Ohm's Law, Eq. (2.77), that includes the anisotropic pressure effects from $\underline{\underline{\mathbf{f}}}_2$ is considered again:

$$\int_0^\infty v^6 dv \left(\frac{\partial \mathbf{f}_1}{\partial t} + v\nabla f_0 - \frac{e\mathbf{E}}{m_e}\frac{\partial f_0}{\partial v} - \frac{e\mathbf{B}}{m_e} \times \mathbf{f}_1 + \frac{2}{5} v \, \nabla \cdot \underline{\underline{\mathbf{f}}}_2 = f_{Cee} \frac{Y n_i Z^2}{v^3} \mathbf{f}_1 \right) \tag{6.5}$$

$$\mathbf{E} = \overline{\eta}\mathbf{j} + \frac{\mathbf{j} \times \mathbf{B}}{e n_e} - \mathbf{v}_N \times \mathbf{B} - \frac{\nabla \left(n_e m_e \langle v^5 \rangle \right)}{6 e n_e \langle v^3 \rangle} - \frac{\nabla \cdot \left(n_e m_e \langle \mathbf{v}\mathbf{v} v^3 \rangle \right)}{2 e n_e \langle v^3 \rangle} \tag{6.6}$$

where the last term refers to the effect of a semi-collisional version of anisotropic pressure.

Magnetic reconnection in the intermediate regime between collisionless and collisional reconnection created in recent laser-plasma experiments [52, 53, 56, 57] has introduced an experimental platform with plasma conditions such that the Nernst effect is important.

Given the analogous form of the Nernst term and Hall current term in Ohm's law, it

is natural to assume that the Nernst effect may enable reconnection in a similar manner to Hall reconnection, but with the electron currents replaced by heat fluxes.

To parameterize under what conditions the situation where the Nernst velocity may be the dominant method of field convection, we can compare the relative magnitudes of the Hall term, $\mathbf{j} \times \mathbf{B}/en_e$, and the heat flow term, $\mathbf{v}_N \times \mathbf{B}$ in Ohm's law to generate a new dimensionless number:

$$H_N = \frac{en_e|\mathbf{v}_N|}{|\mathbf{j}|} = \frac{1}{5}\frac{\kappa_\perp^c}{\omega_c\tau_{ei}}\left(\frac{1}{\tilde{\delta}_c}\right)^2 \equiv \frac{1}{5}\kappa_\perp^c\beta\omega_c\tau_{ei} \tag{6.7}$$

where $\omega_c\tau_{ei}$ is the Hall parameter, $\kappa_\perp^c$ is the normalized perpendicular thermal conductivity coefficient [70] and we have used the heat flux component $\mathbf{q}_{e\perp} \sim \kappa_\perp \nabla T_e$ to estimate $\mathbf{v}_T$ and assumed the gradient scale lengths for the temperature and magnetic field are similar. The normalized skin depth, $\tilde{\delta}_c = c/(v_{\text{th}}\omega_{pe}\tau_{ei})$ serves as an independent parameter in Eqn. 6.7. A small skin depth relative to the mean-free-path means that electron currents are inhibited, but the semi-collisional behavior still allows for electron energy transport. β is the ratio of thermal pressure to magnetic pressure. In the limit of large $\omega_c\tau_{ei}$, the $\kappa_\perp^c$ approaches the asymptotic limit $\kappa_\perp^c = \gamma_1'/(\omega_c\tau_{ei})^2$, where γ_1' is a coefficient between 3.25 and 4.66 depending on Z [70]. Hence, for large $\omega_c\tau_{ei}$, $H_N = (\gamma_1'/5)\beta/\omega_c\tau_{ei}$ and can therefore only be significant for a high β plasma.

An important parameter in magnetic reconnection is the Lundquist number S. We can also introduce an analogously formulated Nernst-Lundquist number, $S_N = v_N L\mu_0/\eta$, which is defined according to the usual definition, but replacing the Alfvèn velocity with the more relevant Nernst velocity. The relationship between these two dimensionless parameters is described by

$$S_N = H_N\omega_c\tau_{ei} = \frac{\kappa_\perp^c}{5}\left(\frac{1}{\tilde{\delta}_c}\right)^2 \tag{6.8}$$

From these dimensionless numbers, we can see that for an interesting heat-flux recon-

nection problem (i.e. for $\omega_c \tau_{ei} \geq 1$) dominated by Nernst effects ($H_N \gg 1$), the Nernst-Lundquist number must also be large, $S_N \gg 1$. This means that resistive effects will be small, and therefore anisotropic pressure-like (f_2) effects must be included in Ohm's law to support the electric field at the X-point. In ref. [130], Daughton et al. included heat flux effects in their reconnection study, but for their system $H_N \lesssim 1$ so the thermal contribution was small. Here we examine a situation where $H_N \gg 1$ where heat flux effects dominate.

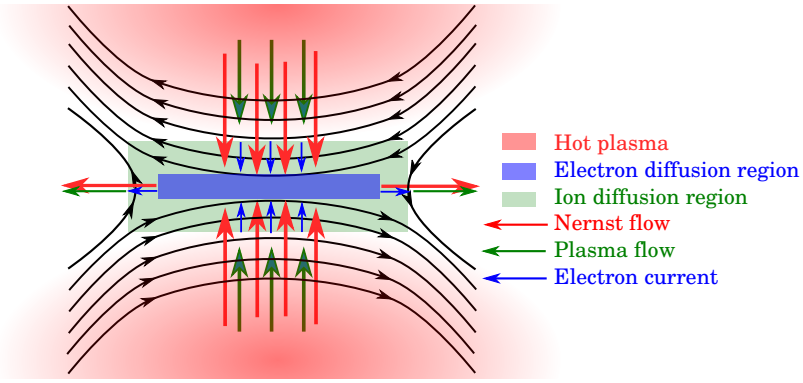

Figure 6.4: An extension of Hall reconnection in semi-collisional plasmas is proposed where the Nernst flow is also responsible for magnetic field transport. The heat flow does not have the same scale of separation over which bulk and two-fluid effects differ in strength and can transport the field over longer distances than the current.

An illustration of the proposed reconnection mechanism is provided in Fig. 6.4 where the Nernst flow is an additional field transport term that becomes relevant and can perform similarly to the Hall and Bulk flow term but is not subject to the separation of scale necessary for Hall reconnection. It can act much like the Hall term and the plasma bulk flow term and serve to transport the magnetic field into and out of the reconnection region. The semi-collisional analogue of the anisotropic pressure tensor from Eq. (6.4) is predicted to be responsible for the electric field in the reconnection region because the resitivity is negligible.

6.2 Results

The computation is performed in a domain defined over the range $-100\lambda_{\text{mfp}} < y < 100\lambda_{\text{mfp}}$ and $-1500\lambda_{\text{mfp}} < x < 1500\lambda_{\text{mfp}}$. The cells near the boundary in $\hat{x}$ are exponentially increasing in step size such that they can be considered "far away". The domain of interest in $\hat{x}$, where the cell size is constant, is $-400\lambda_{\text{mfp}} < x < 400\lambda_{\text{mfp}}$. The numerical resolution in the runs shown in the paper is $\Delta x = 13.3333\lambda_{mfp}, \Delta y = 3.125\lambda_{mfp}, \Delta v = 0.0625 v_{th}$.

The connection between the normalized quantities and real parameters is made through the ratios v_{th}/c and $\omega_{pe}\tau_n$. Here, $v_{\text{th}}/c = 0.08$ and $\omega_{pe}\tau_n = 125$ are chosen in order to put the system into inertial confinement relevant conditions, corresponding to a temperature $T_{e0} = 1.6$ keV and electron number density $n_e = 2.5 \times 10^{22}$ cm^{-3}. A magnetic field of $B_0 = 1$ corresponds to a field strength of 400 T (4 MG).

The magnetic field is generated through the $\nabla n_e \times \nabla T_e$ mechanism. An out of plane plasma density gradient given by

$$\frac{\partial n(x,y)}{\partial z} = \frac{n_0}{L_n} e^{-(x/r_0)^2} \left(e^{-((y+y_{\text{max}})/r_0)^2} + e^{-((y-y_{\text{max}})/r_0)^2} \right), \tag{6.9}$$

where $L_n = 50$ and $r_0 = 50$, is introduced by adding a z component of electric field. This gradient is switched off at $t = 800\tau_n$ to prevent excessive magnetic field generation. The temperature profile is accomplished by heating the plasma near the y-boundaries of the system using an inverse bremsstrahlung heating operator [65] with a profile $H(x,y) = H_0 e^{-(x/r_0)^2} \left(e^{-((y+y_{\text{max}})/r_0)^2} + e^{-((y-y_{\text{max}})/r_0)^2} \right)$ where $H_0 = 0.5$, corresponding to a laser of intensity 2.5×10^{14} W cm^{-2}. The heated regions result in strong heat fluxes in the $\hat{y}$ direction that advect the magnetic field lines inwardly towards the reconnection region. Ions are stationary in the simulation to isolate these effects, which may be justified physically in the case of the walls of a hohlraum as they are heavy ions (for example gold) [21]. Simulations run with ion motion show similar behavior. However, as shown in ref. [101], there is a

scale length dependence on the ratio $\mathbf{v}_N/\mathbf{C}$ where C is the ion velocity, so that for larger systems and longer time scales, hydrodynamic motion will become more important.

Figure 6.5 shows output from the simulation at a time $19000\ \tau_n$. (a) shows the magnetization of the plasma, $\mathbf{B}$ and (b) illustrates the temperature profile of the system. The Nernst velocity (c) is approximately 10^2 larger in magnitude than the maximum current (not shown). The flow direction of the Nernst velocity (calculated directly from the distribution function) indicates that thermal energy is being brought inwards in the y-direction towards the reconnection region and is subsequently redirected outwards in the x-direction, carrying the magnetic field with it. Distinct "jets" of heat flux are formed out of the reconnection region.

Figure 6.5(d) shows the magnetic field profile after the majority of the flux has reconnected, at a time $27000\ \tau_n$ into the simulation, which corresponds to approximately 0.6 ns. The reconnected field lines are then advected by the Nernst jets towards the $\hat{x}$ boundaries. Figure 6.5(e) shows the temperature profile at the same time as the magnetic field in (d). The outward heat flow in $\hat{x}$ from the reconnection process causes the change in the temperature profile from (b) to (e).

The quantity E_z is the rate at which magnetic flux crosses the neutral point. In the case of oppositely directed magnetic fields, B_x, the reconnecting magnetic field, B_y, is generated through Faraday's Law by the out of plane electric field, $\partial E_z/\partial x$ in a 2-D Cartesian geometry. We can analyze the various contributions from the generalized Ohm's Law, Eq. (2.77) by directly calculating the velocity moments. Figure 6.6 shows the out-of-plane electric field, E_z, and four of the terms that contribute to it. Anisotropic pressure tensor-like terms almost entirely support E_z at the X-point where the flows diverge, with a small contribution from the resistive term. The $\mathbf{v}_N \times \mathbf{B}$ term provides an analogue of the Hall current, with the actual Hall current $\mathbf{j} \times \mathbf{B}$ being negligible. The sum of just these moments of the numerical distribution function agrees well with the electric field taken from the code

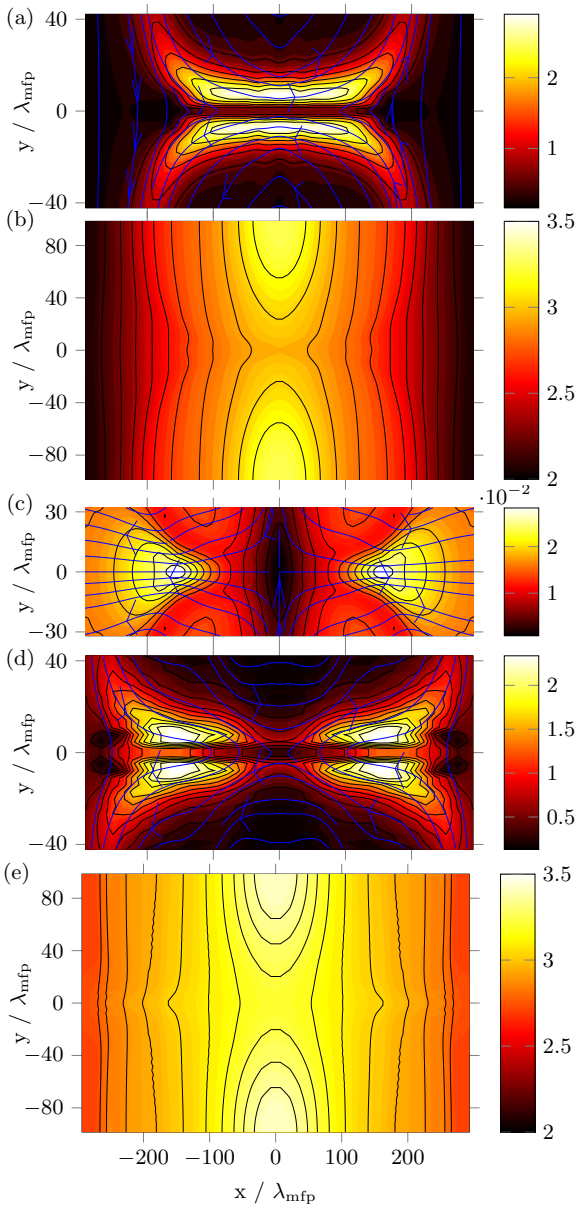

Figure 6.5: At a time $t = 19000\,\tau_n$ into the simulation (a) $\mathbf{B}/m\nu_{ei}/e$, (b) T_e/T_{e0}, (c)$\mathbf{v}_T/v_{\text{th}0}$ in the $x-y$ plane, (d) $\mathbf{B}/m\nu_{ei}/e$ and (e) T_e/T_{e0} at $t = 27000\,\tau_n$. Figure reproduced from ref. [106]. Note: The axes are not square.

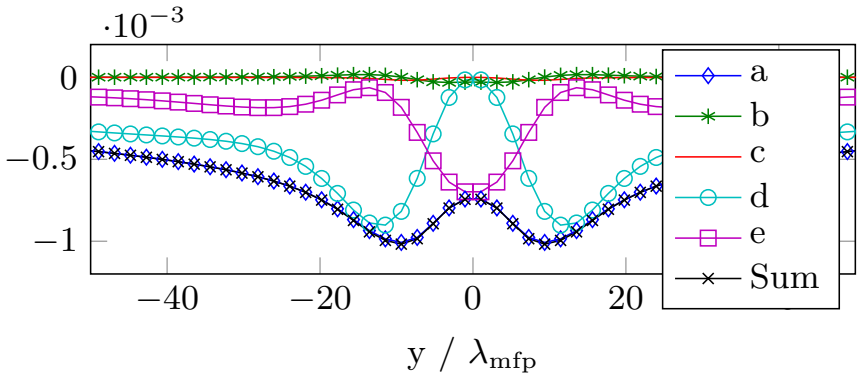

Figure 6.6: Illustration of the contribution of the different components of Ohm's Law in Eq. (2.77) taken from the simulation at a time $t = 11000\ \tau_n$. (a) E_z calculated from the code, (b) $\bar{\eta} j_z$, (c) $[\mathbf{j} \times \mathbf{B}]_z$, (d) $[\mathbf{v}_N \times \mathbf{B}]_z$,(e): $\left[\frac{\nabla \cdot \langle \mathbf{v}\mathbf{v} v^3 \rangle}{2\langle v^3 \rangle}\right]_z$, (f) Sum of all contributions (b-e). Figure reproduced from ref. [106].

(which in these calculations includes electron inertia).

6.2.1 Reconnection Rate

By convention, as in [56], the reconnection rate coefficient is reported as E_z/Bv_A where v_A is the Alfvèn velocity and typical rates associated with fast reconnection are $E_z/Bv_A = 0.1 - 0.2$. In this simulation, the ions are fixed, and consequently, Alfvènic flows are nonexistent. The characteristic flow velocity for the flux is clearly $\mathbf{v}_N$. There is a marked increase in the strength of the magnetic field near the reconnection region. Fox et al. [56] account for this effect in the calculation of the local magnetic field, and we perform the same correction. We find that in our simulation, $E_z/Bv_N \approx 0.1$, as shown in Fig. 6.7(a).

Figure 6.7(b) illustrates the evolution of β, the ratio of thermal pressure to magnetic pressure. The sharp peak arises due to rapid heating of the plasma, and then the subsequent decrease comes from the compression of the magnetic field flux before the reconnection process can begin. Once the anisotropic pressure-like term, Fig. 6.6(e) supports the out-of-plane electric field, E_z, across the reconnection layer, the field compression is maintained and eventually reduced, while the plasma is heated due to the decrease in transport inhi-

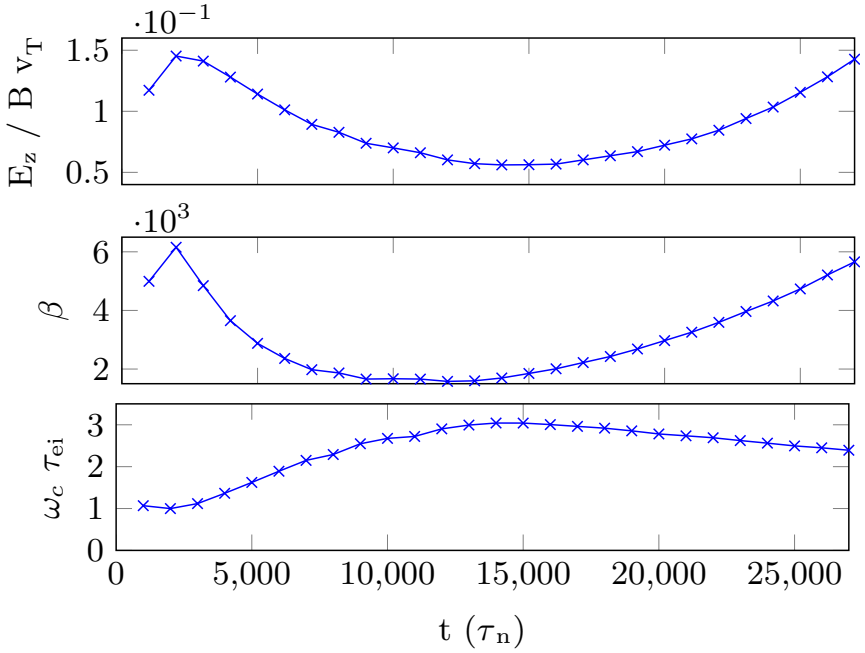

Figure 6.7: (a) The reconnection rate (b) β - the ratio of thermal pressure to magnetic pressure (c) $\omega_c \tau_{ei}$ as functions of time.

bition because of the reconnection process. This corresponds to the steady increase in β as observed after $t = 13000\tau_n$. Figure 6.7(c) illustrates the magnetization of the plasma over time. The initial rise in $\omega_c \tau_{ei}$ is due to the compression phase of the magnetic field. After this period, a plateau arises because while the magnetic field decompresses due to reconnection, the plasma heats in the reconnection region, effectively increasing τ_{ei}. The steady decrease in the late-time behavior is attributed to the magnetic field decompression as the reconnected field lines relax from the Nernst outflows.

When simulations are performed with different values of ω_p/ν_{ei} and v_{th}/c, i.e. different plasma density and temperature, they evolve similarly for fixed $\tilde{\delta}_c$, with a reconnection rate stabilizing close to $E_z/Bv_N \approx 0.1$, as expected from H_N, which only depends on $\tilde{\delta}_c$ for fixed $\omega_c \tau_{ei}$. Hence, the ratio of the skin depth to the collision mean-free-path is the important consideration for this mechanism. One significant difference with Hall reconnection that we wish to highlight is that quasi-neutrality can be maintained throughout the system and therefore there is no necessity for ion motion outside of the reconnection region to

maintain dynamic equilibrium. Redirected heat flows by magnetic reconnection can result in a redistribution of thermal energy and reconnection of field lines can remove thermal transport barriers.

CHAPTER 7

Conclusion

This chapter will attempt to summarize the consequences of the work performed in this thesis. The overarching goal was to examine the kinetic behavior of thermal energy transport in ICF plasmas and the research showed that the plasmas exhibit kinetic behavior in a myriad of ways. The author was responsible for the development of a ray-tracing module for IMPACTA and then using this code to perform and discuss the results of kinetic modeling of ICF plasmas in a full-scale 2D hohlraum with laser heating and self-generated, and externally applied, magnetic fields as well as modeling and discussion of a novel magnetic reconnection mechanism in ICF plasmas.

In the kinetic modeling that has been performed in this thesis, the necessary approximations in fluid modeling are not made and the classical transport coefficients are not used in the calculations, but used only for comparison. Such comparisons serve to illustrate and quantify the importance of kinetic effects. By using a VFPM formulation, this work self-consistently included kinetic effects such as distortion of the distribution due to IB heating, velocity dependent electron-electron and electron-ion collisions, and non-local heat flow that result in noticeable distortion of the electron distribution function in ICF plasma.

Given the prior history on the subject [23, 31, 41, 131, 21], the most straightforward topic of study with respect to magnetic fields in hohlraums is examining the influence of self-generated magnetic fields, due to the Biermann Battery effect, on thermal energy

transport. The details of this work are given in Chapter 4.

The temperature gradients caused by laser heating are perpendicular to the plasma density gradient and result in MG fields near the laser incidence region. This significantly modifies the thermal transport from Braginskii theory. The self-generated fields result in moderate magnetization of the electron plasma, $\omega\tau \sim 1$. Due to the behavior of the "wedge" transport coefficients, $\alpha_\wedge$, $\kappa_\wedge$, and $\beta_\wedge$, the effects in the $\mathbf{b}\times\mathbf{s}\times\mathbf{b}$ direction become relevant for such moderately magnetized plasmas. The study shows that the Righi-Leduc effect, from the $\kappa_\wedge$ term, becomes prominent in influencing the heat flow. The heat flow is increasingly moved towards the dense plasma rather than flowing into the low Z plasma. The inhibition of perpendicular thermal conduction results in thermal energy confinement near the laser hot-spots. Examining the distribution function shows the prevalence of DLM distributions and illustrates the effect of IB heating. The distorted distribution function results in anomalous heat flow as prescribed by ref. [65]. Most importantly, the simulations show evidence of non-local heat flow throughout the hohlraum. This can be shown by comparing the calculated heat flow to that calculated using the transport coefficients. It can also be qualitatively observed by examining the distribution function. The suppression of heat flow near the laser hot-spots due to non-locality naturally leads to increased heat flow in regions farther downstream causing some anisotropic heating of the low density plasma in regions where the self-generated magnetic field does not affect the heat flow significantly.

A natural extension to the hohlraum study, given the burgeoning interest in the application of external magnetic fields to hohlraums [132, 119]. Given the strongly non-local heat flows that were shown in Chapter 4, and the Nernst effect that was described in Chapter 2, it was reasonable to expect that this external magnetic field can be significantly affected by the Nernst effect. Considering the scalings provided in [65, 106], the Nernst effect should be a relevant, if not dominant, contributor towards the advection of magnetic fields. The simulations show that the Nernst effect is crucial towards modeling the magnetic field

dynamics accurately. The magnetic field is transported towards the hohlraum axis on timescales much faster than in the case where the magnetic field is frozen to the plasma. Additionally, the prevalence of non-locality results in an augmentation of the Nernst effect for the case of a 7.5 T imposed field.

Running these simulations for different magnetic field strengths showed the expected result that the Nernst velocity is decreased by increasing magnetic fields. However, clear trends for the magnitude of the temperature profile were also evident. Increasing the magnetic field resulted in an increase in thermal energy confinement near the laser-heated region due to the inhibition of perpendicular heat flow.

The third primary topic of study in this thesis was magnetic reconnection driven by heat flux effects. Since we have shown that the Nernst term can be a significant, if not dominant, contributor to the advection of the magnetic field, it is a straightforward extension to suggest that the Nernst term can act as the primary advection in magnetic reconnection instead of plasma bulk flow or the Hall term. The simulations confirmed these predictions in the regime of a high Beta, $\beta > 1000$, and weakly magnetized, $\omega\tau \sim 1$, plasma. Performing analysis of the reconnection rate showed that "fast" reconnection was recovered when considering that the characteristic velocity of the magnetic field carrying particles was governed by the Nernst velocity, rather than the Alfven velocity. This is particularly relevant to the hohlraum. The thermal energy transport inhibition that occurs due to the magnetization of the plasma that is discussed in the side-on geometry in Chapter 4 is also displayed in the face-on geometry. In the modeling in Chapter 6, however, the topological change in the magnetic field re-enables thermal transport between the two laser spots, and allows release of thermal energy towards the magnetic reconnection outflow region. Therefore, the reconnection process, by governing the magnetic field dynamics, may be influential towards accurately determining the thermal energy profile in a hohlraum.

In summary, the work performed here describes the richness of kinetic behavior in ICF

plasmas and shows that it manifests itself not only in the form of non-local heat flow but also by redirecting heat flow and modifying magnetic-field-generation and magnetic-field-transport rates due to the presence of magnetic fields. It emphasizes the need for kinetic modeling of magnetized plasma that fully contains the various effects that are influential towards the evolution of plasma properties such as heat flow, temperature, and magnetic fields. At the very least, it exhibits the ability of kinetic modeling to identify new effects that may be important to include in fluid modeling of ICF plasmas over nanosecond time-scales.

7.1 Future Work

There are approximations made that could be improved upon within this work. Primarily, this work focuses on understanding the thermal energy dynamics in different contexts relevant to a high Z hohlraum using kinetic modeling for the electron plasma and hydrodynamic ions.

The inclusion of a radiation transport model would not only enable better determination of the x-ray drive asymmetry discussed in Section 1.3.2, but also opens a new regime of thermal energy transport modeling. At the time of writing, only 1D radiation-hydrodynamic-Vlasov-Fokker-Planck has been performed [133] but modeling in 2D with electromagnetic fields does not exist. The work in ref. [133] provides a starting point for the inclusion of radiation effects in kinetic modeling. The availability of such tools enables comparisons with radiation-hydrodynamics codes used for designing ICF experiments.

In a similar theme, inclusion of thermal energy transfer from electrons to ions through collisions improves conservation of the thermal energy in the system. This enables the influence of effects such as resistive heating and dynamic ion thermal pressure. The ion temperature, and thus the ion thermal pressure, is currently implemented as a static value.

In the context of the electron plasma kinetics, the treatment of electron-electron collisions in the $\mathbf{f}_1$ equation could be improved upon. The integro-differential equation set is provided by Epperlein & Haines [70]. The computational cost of calculating these has, however, been prohibitive. Innovative methods of the calculation of these quantities could involve truncating the electron-electron collision operator, but ideally, should involve a speed increase in the full calculation through improvements in the numerics. This feature would enable the calculation of the transport coefficients that depend on the atomic number, Z, the power of the super-Gaussian fit to the distribution function, m, and magnetization, $\omega\tau$. At the time of writing, the transport coefficients are only a function of $\omega\tau, Z$ [70] or $\omega\tau, m$ [65].

Inclusion of these missing effects will further the goals of this thesis; to perform detailed calculations of electron transport and magnetic field dynamics using a kinetic formulation such that the thermal energetics of the hohlraum are subject to fewer approximations than in the classical transport model, and study the significance of the modification to transport by kinetic effects. These improvements would go one step further and enable better comparisons with an integrated radiation-hydrodynamics code.

APPENDIX A

Electron-Electron Collisions in the f_1 equation

The Fokker-Planck collision terms are expanded in [72] and are rewritten as

$$C_0 = \frac{Y}{3v^2}\frac{\partial}{\partial v}\left[A_0 f_0 + B_0 \frac{\partial f_0}{\partial v}\right] + \mathcal{O}(m_e/m_i), \tag{A.1}$$

$$C_{1i} = \frac{Y}{3v^2}\Bigg[- \frac{A_0(f_{\text{ions}})}{v} f_{1i} + \frac{\partial}{\partial v}\left(A_0 f_{1i} + B_0 \frac{\partial f_{1i}}{\partial v}\right) - \left(\frac{\partial B_0}{\partial v} + A_0\right) f_{1i} + \frac{v}{5}\left(3\{B_1\}_i \frac{\partial^2 f_0}{\partial v^2} - \frac{\partial}{\partial v}\{B_1\}_i \frac{\partial f_0}{\partial v}\right) + \frac{\{A_1\}_i}{3}\frac{\partial f_0}{\partial v} + 12\pi f_0 f_{1i} v^2\Bigg] + \mathcal{O}(m_e/m_i), \tag{A.2}$$

$$C_{2ij} = -\frac{A_0(f_{\text{ions}})}{v^3} f_{2ij} + \{C_{2ee}\}_{ij} + \mathcal{O}(m_e/m_i), \tag{A.3}$$

$$C_{3ijk} = -\frac{6A_0(f_{\text{ions}})}{v^3} f_{3ijk} + \{C_{3ee}\}_{ijk} + \mathcal{O}(m_e/m_i), \tag{A.4}$$

where,

$$A_i = 3I_i^i, \qquad B_i = \left(I_{2+i}^i + J_{-1-i}^i\right), \tag{A.5}$$

$$I_j^i = \frac{4\pi}{v^j}\int_0^v f_i u^{j+2} du, \qquad J_j^i = \frac{4\pi}{v^j}\int_v^\infty f_i u^{j+2} du, \tag{A.6}$$

$$Y = 4\pi\left(\frac{ZZ'e^2}{4\pi\epsilon_0 m_e}\right)^2 \ln\Lambda. \tag{A.7}$$

IMPACTA was developed with the Lorentz approximation in mind for modeling high Z plasmas so it was developed to utilize the first term in C_{1i}. This is the only term that refers

to electron-ion collisions, the rest account for electron-electron collisions. Using IMPACTA for hohlraums requires better modeling of the low Z plasma where the collisions between electrons result in non-negligible momentum changes.

The author of this dissertation was responsible for the implementation of a scaling for the collision frequency that reproduces the effects of electron-electron collisions on the heat flow. The authors of ref. [134] had prescribed a Z-dependent scaling, $\phi_E = (Z + 4.2)/(Z + 0.24)$ for the collision frequency that results in better agreement with the full calculation of the thermal conductivity in low Z plasmas such as that performed in ref. [70]. In the implementation with IMPACTA, the collision frequency is scaled such that

$$\nu_{ei} = \frac{Y\phi Z^* n}{v^3} \text{ where } \phi = \frac{1}{0.236}\frac{1 + 0.236Z}{Z + 0.236}. \tag{A.8}$$

This fit for the collision frequency in low Z plasma results in better agreement with the thermal conductivity calculated in ref. [70] and the results of testing for a range of magnetizations are shown below in Fig. A.1. The collision frequency increases as the atomic number of the plasma decreases. Since the work performed in [134] is for unmagnetized plasmas, the scaling is not accurate for $\omega\tau > 0.1$ because electron-electron collisions are influenced by the magnetic fields.

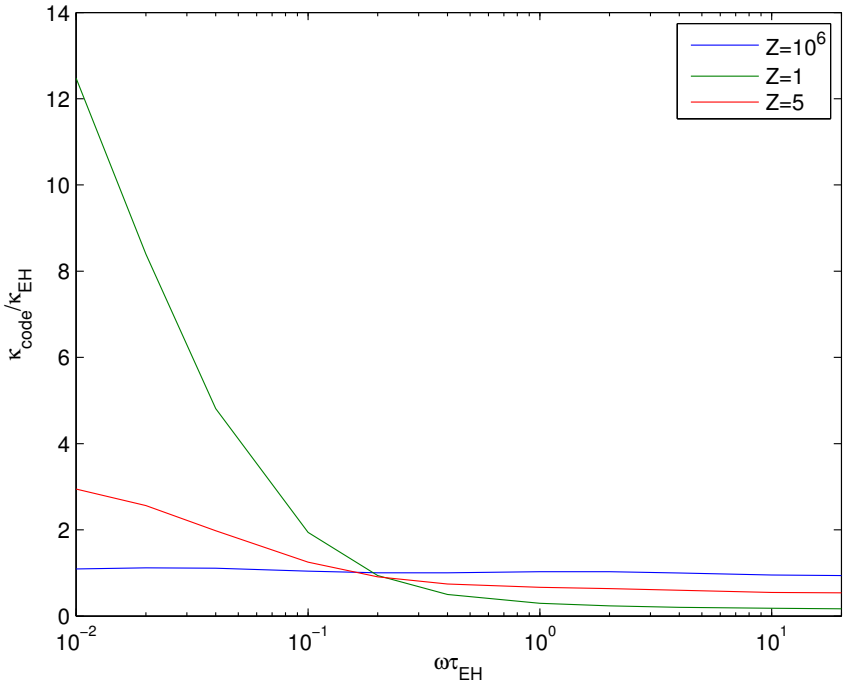

(a)

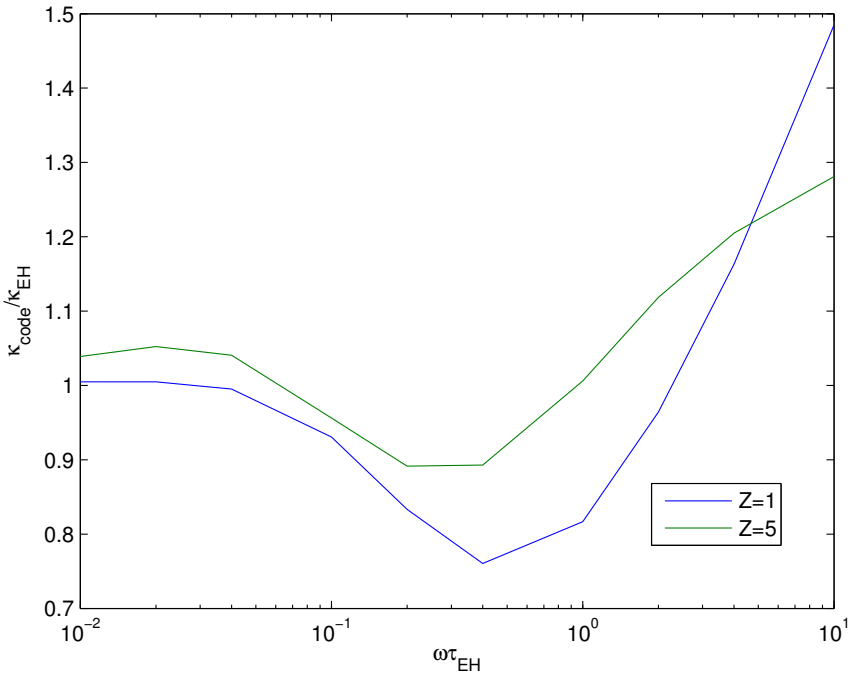

(b)

Figure A.1: (a) The Lorentz approximation results in an overcalculation of κ at low $\omega\tau$ for low Z plasma, (b) Using the correction provided by Eq. (A.8), κ at low $\omega\tau$ for low Z plasma is accurate to that which is calculated by the collision operator specified in ref. [70]. This scaling, however, does not extend to magnetized plasmas and results in errors for low Z, moderate $\omega\tau$ plasmas.

APPENDIX B

Ray Tracing

The author was responsible for the development of the ray-tracing module that is coupled to IMPACTA through the IB heating operator. This appendix describes the steps the algorithm performs to model the passage of a laser through a magnetized plasma and approximates a energy deposition pattern along the laser path. A flowchart for these steps is shown in Fig. B.1.

B.1 Laser Parameters

The implementation requires the following 11 inputs.

1. W_{beam}: Beam width in units of λ_{mfp},
2. N_{rays}: Beam resolution. This is the number of rays per processor,
3. x or y: Boundary from which the beam is launched,
4. U, S, G: Shape of the beam. This can be Uniform, Sin^2, or Gaussian,
5. n_c: Critical density in units of n_{e0},
6. x_0: Initial x position. Disabled for hohlraum problem,
7. y_0: Initial y position. Disabled for hohlraum problem,

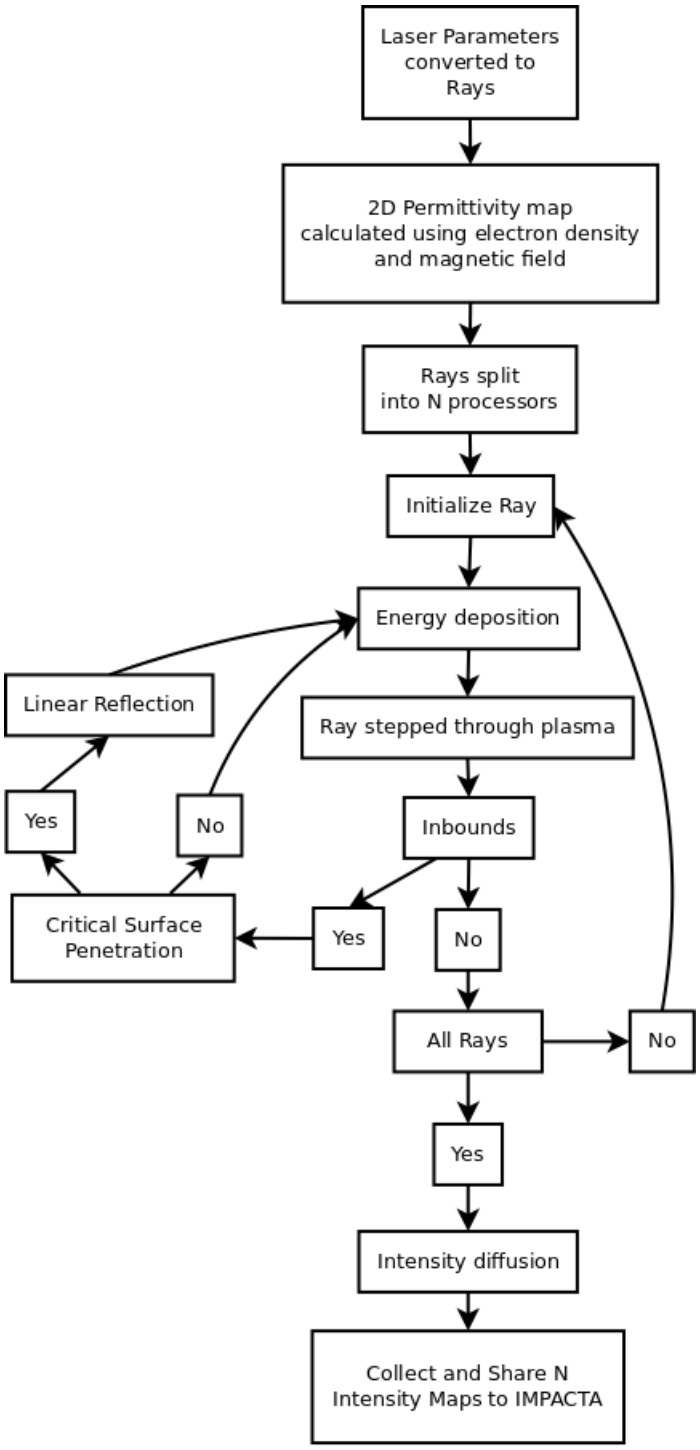

Figure B.1: Step-by-step illustration of the algorithm and how it calculates the propagation of each ray

8. θ_0: Angle of propagation relative to surface,

9. $\delta\theta$: Angular spread,

10. ds: Step size of each ray in units of smallest cell dimension,

11. $N_{\text{i-d}}$: Number of intensity diffusion iterations.

Since the path taken by each ray is independent, each processor can perform the algorithm independently. The algorithm essentially splits the beam into $N_{\text{processors}}$ parts. These parts are modeled by the propagation of N_{rays} so the beam is modeled by the propagation of $N_{\text{totalrays}} = N_{\text{processors}} \times N_{\text{rays}}$.

The subroutine calculates $x_{r,0}$ for each ray as a function of x_0, r, W_{beam} where r is the ray index and performs the same for $y_{r,0}$. Using the angular information, the routine calculates v_x, v_y where $|v| = 1$. The angular spread is used as a function of the number of beams. The angle of incidence of ray r is

$$\theta_r = (\theta_0 - \delta\theta) + 2\delta\theta \frac{r}{N_{\text{totalrays}}}.$$

B.2 Index of Refraction

The extraordinary wave relation is

$$\epsilon = \left(\frac{ck}{w}\right)^2 = 1 - \frac{\omega_p^2}{\omega^2}\frac{\omega^2 - \omega_p^2}{\omega^2 - \omega_p^2 - \omega_c^2}, \tag{B.1}$$

$$= 1 - \frac{n}{n_c}\frac{1 - n/n_c}{1 - n/n_c - \tilde{B}^2/n_c\frac{\nu_{ei0}^2}{\omega_{pe0}^2}}, \tag{B.2}$$

where ω is the laser frequency. The algorithm only requires $\nabla\eta/\eta$ where η is the index of refraction. Since the code uses ϵ, η/η is provided as $\nabla\epsilon/2\epsilon$. $\nabla\epsilon$ is calculated using center differencing. Both of these quantities are stored prior to the start of the ray tracing algorithm and retrieved when necessary as the ray progresses. This is detailed in Appendix B.4.

B.3 Energy deposition

The energy deposition is based on the IMPACTA laser heating module. IMPACTA has the capability to heat the plasma using inverse bremsstrahlung heating in the form of a 2D profile that provides the equivalent of out-of-plane laser heating. Extending this capability to in-plane laser heating requires an in-plane laser map that provided by the ray tracing algorithm.

The intensitycalc() function receives

1. the normalizing constant,
2. position of ray (x, y) and $I(x, y)$, the intensity matrix with respect to the spatial grids, as well as the spatial grids,
3. the density matrix, $n(x, y)$ along with n_c, the critical value,
4. the initial group velocity, v_{G0}.

The intensity map generated by each ray is given by calculating

$$\frac{dI}{dt} = \frac{C}{v_G(x, y)} \frac{A_{\text{ray}}}{A_{\text{cell}}} \tag{B.3}$$

along the path of the ray. On a discrete spatial grid, the intensity map calculation requires the allocation of deposited energy at a point (x, y) to the nearest grid points, (x_0, y_0), (x_1, y_1), (x_2, y_2), and (x_3, y_3). This is performed using the reverse process of bilinear interpolation. illustrated in Fig. B.2.

Given a ray is at (x, y), the energy allocated to each of the four grid points between which (x, y) exists, (x_0, y_0), (x_1, y_1), (x_2, y_2), and (x_3, y_3), is a function of the area between the grid point and the ray location. By discretizing Eq. (B.3), the intensity at the grid points

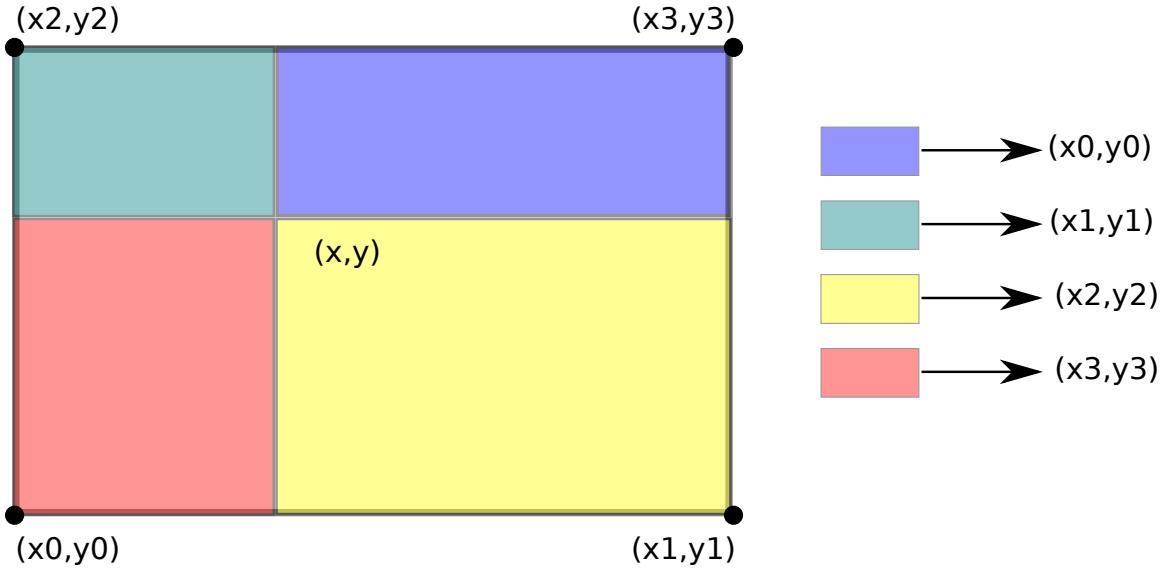

Figure B.2: Illustration of the reverse bilinear interpolation concept that is used to allocate laser intensity to the IMPACTA (x,y) grid.

is given by

$$I_{i,j}^{n+1} - I_{i,j}^{n} = \frac{C}{v_{G:i,j}} \left(1 - \frac{A_{\text{ray}}}{A_{\text{cell}}} \right), \tag{B.4}$$

$$I_{i,j}^{n+1} = I_{i,j}^{n} + \frac{C}{v_{G:i,j}} \left(1 - \frac{|(x - x_{i,j})(y - y_{i,j})|}{dx\ dy} \right), \tag{B.5}$$

$$I_{i,j}^{n+1} = I_{i,j}^{n} + I_N \frac{v_{G:r0}}{v_{G:i,j}} \left(\frac{|(x - x_{i+1,j+1})(y - y_{i+1,j+1})|}{dx\ dy} \right). \tag{B.6}$$

The algorithm allocates to the intensity map every time the ray takes a successful step in the domain. For this reason, it is simpler to include the allocation in the form given in Eqs. (B.7) to (B.10) for the 4 adjacent grid points to the position of the ray. The allocation

is given by

$$I(x_1, y_1) = I(x_1, y_1) + I_N \frac{|x - x_2||y - y_2|}{dx\ dy} \frac{v_G(x_0, y_0)}{v_G(x, y)}, \tag{B.7}$$

$$I(x_2, y_1) = I(x_2, y_1) + I_N \frac{|x - x_1||y - y_2|}{dx\ dy} \frac{v_G(x_0, y_0)}{v_G(x, y)}, \tag{B.8}$$

$$I(x_1, y_2) = I(x_1, y_2) + I_N \frac{|x - x_2||y - y_1|}{dx\ dy} \frac{v_G(x_0, y_0)}{v_G(x, y)}, \tag{B.9}$$

$$I(x_2, y_2) = I(x_2, y_2) + I_N \frac{|x - x_1||y - y_1|}{dx\ dy} \frac{v_G(x_0, y_0)}{v_G(x, y)}. \tag{B.10}$$

The fraction to the right of I_N is the result of the areal weighting scheme. The last fraction containing the group velocity is a direct result of the discretization of Eq. (B.3) where the group velocity (normalized to c) is $v_G(x, y) = \sqrt{1 - n/n_c}$.

I_N is the factor that normalizes the contribution from all the rays that represent a single beam as well as the contribution that arises from the multiple steps needed for a ray to traverse a cell. The normalizing constant for intensity is given by

$$I_N = S(x, y) \frac{W_b}{N_{\text{total}}} \frac{ds/\cos(\theta_0)}{dx\ dy}, \tag{B.11}$$

where W_{beam} is the beam width in mean free paths, and N_{total} is # of rays per beam. This fraction represents the width of each ray and accounts for the inclusion of multiple rays per beam. $S(x, y)$ is a beam shaping function as one of the input parameters. The next fraction is due to the fact that $ds < dx$ & $ds < dy$. Because of the small step size, there are multiple contributions to the four grid points adjacent to the location of the ray as it propagates through a cell. This term normalizes the various contributions to each grid point. The cell dimension that is parallel to the width of the beam, either dx or dy, normalizes the width of the beam. The $\cos(\theta_0)$ term normalizes the other dimension along the direction of propagation.

B.3.1 Absorption in Overdense Plasma

The simple relation in Eq. (B.3) used for the intensity calculations is incorrect near the critical surface due to the singularity that arises as the group velocity approaches zero. This results in a intensity profile with an infinitely tall peak. A more realistic absorption profile includes absorption in the overdense plasma as well as a peak in the underdense region and is given by the following analysis based on ref. [135].

The wave equation for the electric field of a plane electromagnetic wave normally incident onto an inhomogeneous plasma slab with a gradient in the $\hat{x}$ direction is

$$\frac{d^2E}{dx^2} + \frac{\omega^2}{c^2}\epsilon(\omega, x)E = 0. \tag{B.12}$$

Assuming that the plasma gradient scale length ($L = 10 - 100$ μm), is much larger than the wavelength of the laser ($2\pi c/\omega = 351$ nm), the density can be approximated as a linear function of position ($n = n_c x/L$). Using this, the wave equation becomes

$$\frac{d^2E}{dx^2} + \frac{\omega^2}{c^2}\left(1 - \frac{x}{L}\right)E = 0. \tag{B.13}$$

Letting $\chi = (\omega^2/c^2L)^{1/3}(x - L)$ and substituting gives

$$\frac{d^2E}{d\chi^2} - \chi E = 0. \tag{B.14}$$

The solution to this differential equation is the linear combination of the Airy functions, A_i and B_i, given by

$$E(\chi) = \alpha \mathrm{A}_i + \beta \mathrm{B}_i, \tag{B.15}$$

where α and β are constants depending on boundary conditions. By physical arguments,

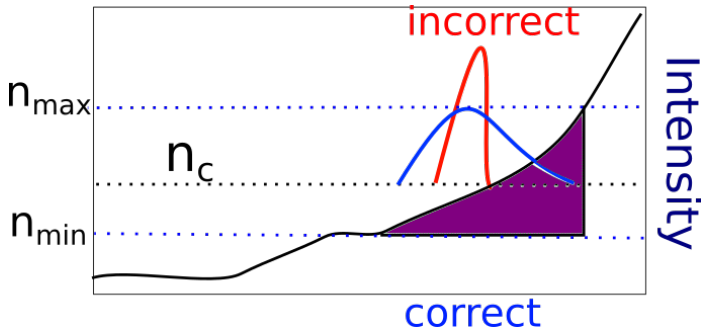

Figure B.3: Since the intensity profile will result in an infinitely tall peak at the critical surface, the ray-tracing algorithm is "tricked" into having a Monte-Carlo prescribed range of critical densities such that it reproduces the Airy absorption profile.

$\beta = 0$. The absorbed laser intensity is given by

$$I_{\text{abs}}(\chi) = |E(\chi)|^2 = \frac{1}{\text{A}_i(1)^2}\text{A}_i(\chi), \tag{B.16}$$

where the normalizing constant is chosen such that the maximum value of $I_{\text{abs}} = 1$. Note that the maximum value occurs at $\chi = 1$ which is in the underdense plasma. The profile decays into the overdense plasma such that $I_{\text{abs}}(-2) \approx 0.002$. The absorption profile is replicated in IMPACTA by determining the critical density for the incoming rays that are weighted according to I_{abs} using a Monte Carlo method such that I_{abs} is replicated from $-2 < \chi < 1$. The idea is illustrated in Fig. B.3.

The algorithm to accomplish this is based on the following three steps:

1. Generate χ from $X \sim U[-1, 2]$ and E from $Y \sim U[0, 1]$.

2. If $I_{\text{abs}}(\chi) \geq E$, convert χ to x in IMPACTA units. If not, repeat step 1.

3. Set the density at x as the critical density for that ray.

B.4 Ray Step

The authors of ref. [113] developed a Crank-Nicholson scheme using the Boris approach. Particle energy is conserved in the Boris scheme and is often used in particle motion schemes involving magnetic fields. The authors extend this method to ray-tracing in plasmas. The algorithm itself is available in ref. [113] but the implementation in IMPACTA uses the extraordinary wave relation where the magnetic field is included in calculation of the index of refraction, and is provided in Eqs. (B.17) to (B.21). The algorithm, reproduced from [113], is

$$\mathbf{r}_{1/2} = \mathbf{r}_0 + \mathbf{v}_0 \frac{ds}{2}, \tag{B.17}$$

$$\Omega_0 = \left(\frac{\nabla\epsilon}{2\epsilon}\right)_{1/2} \times \mathbf{v}_0 \frac{ds}{2}, \tag{B.18}$$

$$\Omega_{1/2} = \left(\frac{\nabla\epsilon}{2\epsilon}\right)_{1/2} \times (\mathbf{v}_0 + \mathbf{v}_0 \times \Omega_0) \frac{ds}{2}, \tag{B.19}$$

$$\mathbf{v}_1 = \mathbf{v}_0 + \frac{2}{1 + (\Omega_{1/2}\frac{ds}{2})^2}(\mathbf{v}_0 + \mathbf{v}_0 \times \Omega_{1/2}) \times \Omega_{1/2}, \tag{B.20}$$

$$\mathbf{r}_1 = \mathbf{r}_{1/2} + \mathbf{v}_1 \frac{ds}{2}. \tag{B.21}$$

This algorithm has been verified against analytical solutions to ray tracing in the presence of linear gradients in the permittivity i.e. $\nabla\epsilon \propto$ constant.

B.5 Test: Oblique Incidence On A Linear Density Ramp

For the test, the linear gradients in permittivity are created by linear density ramps such that

$$\epsilon = 1 - x/L, \tag{B.22}$$

where ϵ is the permittivity and L is the scale-length of the gradient. The permittivity is related to the index of refraction, η, by $\epsilon = \eta^2$.

An analytical expression for the 2D path of a ray incident upon a linear density ramp varying over 1 dimension can be calculated. The governing differential equation for the path of the ray is

$$\frac{d}{ds}\left(\eta\frac{d\mathbf{r}}{ds}\right) = \nabla\eta. \tag{B.23}$$

Assuming that the density gradient is only in the $\hat{x}$ direction, the $\hat{y}$ equation is reduced to

$$\frac{d}{ds}\left(\eta\frac{dy}{ds}\right) = 0. \tag{B.24}$$

To get past this, an initial condition is required. Given that $\eta = \eta_0$ at $\mathbf{r} = (x_0, y_0)$, and $dy/ds = \sin\alpha$ where α is the angle that the ray forms with respect to the $\hat{x}$ axis at $\mathbf{r}$. Integrating the above yields

$$\left(\eta\frac{dy}{ds}\right) = \eta_0 \sin\alpha, \tag{B.25}$$

$$\frac{dy}{ds} = \frac{\eta_0}{\eta}\sin\alpha. \tag{B.26}$$

dx/ds is calculated using the fact that $ds = \sqrt{dx^2 + dy^2}$. The two equations are then combined and the differential equation relating x and y is

$$\frac{dx}{\sqrt{\epsilon - \epsilon_0 \sin^2\alpha}} = \frac{dy}{\sqrt{\epsilon_0}\sin\alpha}. \tag{B.27}$$

Since ϵ is a linear function of x, $\epsilon(x) = \epsilon_0 + (x - x_0)\epsilon_0'$, where $\epsilon_0' = d\epsilon/dx_{x=x_0}$, so the above equation can now be integrated to give

$$\int_{x_0}^{x} \frac{dx}{\sqrt{\epsilon_0' x + \epsilon_0' x_0 - \cos^2\alpha}} = \int_{y_0}^{y} \frac{dy}{\epsilon_0 \sin\alpha}. \tag{B.28}$$

Solving for $x(y)$ yields the trajectory

$$x = x_0 - \frac{\epsilon_0}{\epsilon_0'}\cos^2\alpha + \frac{1}{\epsilon_0'}\left(\sqrt{\epsilon_0}\cos\alpha + \frac{\epsilon_0'}{2\sqrt{\epsilon_0}\sin\alpha}(y - y_0)\right)^2. \tag{B.29}$$

At a point (x_0, y_0) on the grid where $\epsilon = \epsilon_0$, Eq. (B.29) gives the trajectory of a ray with the angle of incidence, α, with respect to the direction of the $\nabla\eta$. A vertex point, x_v, y_v for the parabola shaped path that the ray takes upon oblique incidence of a linear density ramp can be obtained

$$x_v = x_0 - \frac{\epsilon}{\epsilon_0'}\cos^2\alpha \tag{B.30}$$

$$y_v = y_0 - \frac{2\epsilon}{\epsilon_0'}\cos\alpha\sin\alpha \tag{B.31}$$

Comparing the algorithm to the analytical solution from Eq. (B.29) provides a method for verification of the numerical method. The comparisons were made with a permittivity ramp specified by $\epsilon(x) = 1.0 - 0.01x$ and the results for three different angles of incidence are provided in Fig. B.4.

B.6 Reflection

The ray is reflected if the outcome of Eq. (B.21) is a $\mathbf{r}_1$ into the overdense plasma. In this case, a new $\mathbf{r}_1, \mathbf{v}_1$ are calculated using the relations from ref. [113] which are

$$\mathbf{r}_1 = \mathbf{r}_0 + 4\epsilon L\cos\alpha(\mathbf{v}_0 + L\cos\alpha\nabla\epsilon_0), \tag{B.32}$$

$$\mathbf{v}_1 = \mathbf{v}_0 + 2\cos\alpha\nabla\epsilon_0, \tag{B.33}$$

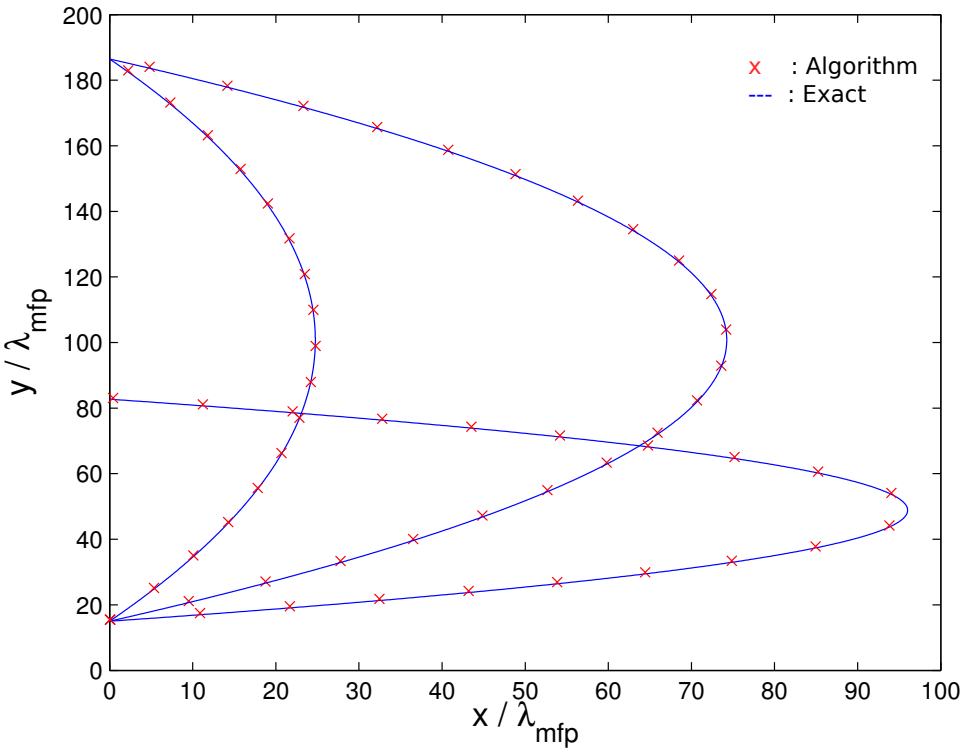

Figure B.4: The performance of the ray-tracing algorithm is compared against analytic solutions of rays incident upon linear density ramps at angles of $10°, 45°$, and $60°$

where

$$L\cos\alpha = \left(-\frac{\mathbf{v}_0 \cdot \nabla\epsilon_0}{|\nabla\epsilon_0|^2}\right). \tag{B.34}$$

B.7 Attenuation

Near the critical surface, the laser is reflected and absorbed. The absorption of the laser energy near the critical surface and the subsequent attenuation of the laser intensity is modeled by scaling the normalizing constant of intensity with an exponential function that decays as the ray travels through the plasma after reflecting or refracting in the high Z material. This

is given by

$$\frac{dI_N}{dt} = -C_{\text{att}} I_N, \tag{B.35}$$

$$I_N^{n+1} - I_N^n = -C_{\text{att}} I_N^n, \tag{B.36}$$

$$I_N^{n+1} = (1 - C_{\text{att}}) I_N^n. \tag{B.37}$$

C_{att} is set after processing an input deck and is a function of the spatial grid resolution.

B.8 Intensity Diffusion

The nature of the problem requires greater resolution than is afforded in IMPACTA. The skin depth of the laser, c/ω, is on the order of the skin depth of the plasma, c/ω_p, near the critical surface. Neither of these distances are resolved in IMPACTA. The inablity to resolve these distances results in loss of smoothness, especially near the critical surface where the energy deposition is the largest.

The angular spread helps with this in the case of refraction while the Airy function implementation helps in the reflective cases. However, despite these implementations, the relevant scales for the mitigation mechanisms are sometimes not resolved. To minimize the issues created by the lack of adequate resolution, the algorithm includes diffusion of the intensity profile.

B.9 Extras

B.9.1 Magnetic Field Influenced Cutoff Frequency

The extraordinary wave relation is used to determine the index of refraction of the ray. The plasma oscillations in response to magnetic fields may result in the indirect interaction of

the laser with magnetic fields that may be present.

$$\frac{\nabla\epsilon}{2\epsilon} = \frac{1}{4\left(n_c - n_e - \frac{\nu_{ei0}^2}{\omega_{pe0}^2}B^2\right)\left((n_c-n_e)^2 - n_c\frac{\nu_{ei0}^2}{\omega_{pe0}^2}B^2\right)} \left[-\left((n_c-n_e)^2 - \frac{\nu_{ei0}^2}{\omega_{pe0}^2}(n_c-2n_e)B^2\right)\nabla n_e + 2\frac{\nu_{ei0}^2}{\omega_{pe0}^2}n_e(n_e-n_c)B\nabla B\right] \quad \text{(B.38)}$$

For cutoff to be pushed forward, $\tilde{B}^2/n_c\frac{\nu_{ei0}^2}{\omega_{pe0}^2} \gtrsim 10\%$ and since $\frac{\nu_{ei0}^2}{\omega_{pe0}^2} \leq 0.01$, a very strong magnetic field is required. This requirement translates to means having a cyclotron frequency comparable to or greater than the plasma frequency, which is a very unlikely scenario in these plasmas.

BIBLIOGRAPHY

[1] S. Atzeni and J. Meyer-ter Vehn, *The Physics of Inertial Fusion*International series of monographs on physics ;no. 125 (Oxford University Press, 2004).

[2] J. D. Lawson, Proceedings of the Physical Society. Section B **70**, 6 (2002).

[3] J. Nuckolls, L. Wood, A. Theissen, and G. Zimmerman, Nature **239**, 139 (1972).

[4] M. Murakami and J. Meyer-ter Vehn, Nuclear Fusion **31**, 1315 (1991).

[5] J. M. Soures, R. L. McCrory, C. P. Verdon, A. Babushkin, R. E. Bahr, T. R. Boehly, R. Boni, D. K. Bradley, D. L. Brown, R. S. Craxton, J. A. Delettrez, W. R. Donaldson, R. Epstein, P. A. Jaanimagi, and S. D. Jacobs, Physics of Plasmas **3**, 2108 (1996).

[6] R. McCrory, S. Regan, S. Loucks, D. Meyerhofer, S. Skupsky, R. Betti, T. Boehly, R. Craxton, T. Collins, J. Delettrez, D. Edgell, R. Epstein, K. Fletcher, C. Freeman, J. Frenje, V. Glebov, V. Goncharov, D. Harding, I. Igumenshchev, R. Keck, J. Kilkenny, J. Knauer, C. Li, J. Marciante, J. Marozas, F. Marshall, A. Maximov, P. McKenty, J. Myatt, S. Padalino, R. Petrasso, P. Radha, T. Sangster, F. Séguin, W. Seka, V. Smalyuk, J. Soures, C. Stoeckl, B. Yaakobi, and J. Zuegel, Nuclear Fusion **45**, S283 (2005).

[7] R. S. Craxton, K. S. Anderson, T. R. Boehly, V. N. Goncharov, D. R. Harding, J. P. Knauer, R. L. McCrory, P. W. McKenty, D. D. Meyerhofer, J. F. Myatt, A. J. Schmitt, J. D. Sethian, R. W. Short, S. Skupsky, W. Theobald, W. L. Kruer, K. Tanaka, R. Betti, T. J. B. Collins, J. A. Delettrez, S. X. Hu, J. A. Marozas, A. V. Maximov, D. T. Michel, P. B. Radha, S. P. Regan, T. C. Sangster, W. Seka, A. A. Solodov, J. M. Soures, C. Stoeckl, and J. D. Zuegel, Physics of Plasmas **22**, 110501 (2015).

[8] V. N. Goncharov, T. C. Sangster, T. R. Boehly, S. X. Hu, I. V. Igumenshchev, F. J. Marshall, R. L. McCrory, D. D. Meyerhofer, P. B. Radha, W. Seka, S. Skupsky, C. Stoeckl, D. T. Casey, J. A. Frenje, and R. D. Petrasso, Physical Review Letters **104**, 165001 (2010).

[9] T. C. Sangster, V. N. Goncharov, R. Betti, P. B. Radha, T. R. Boehly, D. T. Casey, T. J. B. Collins, R. S. Craxton, J. A. Delettrez, D. H. Edgell, R. Epstein, C. J. Forrest, J. A. Frenje, D. H. Froula, M. Gatu-Johnson, Y. Y. Glebov, D. R. Harding, M. Hohenberger, S. X. Hu, I. V. Igumenshchev, R. Janezic, J. H. Kelly, T. J. Kessler,

C. Kingsley, T. Z. Kosc, J. P. Knauer, S. J. Loucks, J. A. Marozas, F. J. Marshall, A. V. Maximov, R. L. McCrory, P. W. McKenty, D. D. Meyerhofer, D. T. Michel, J. F. Myatt, R. D. Petrasso, S. P. Regan, W. Seka, W. T. Shmayda, R. W. Short, A. Shvydky, S. Skupsky, J. M. Soures, C. Stoeckl, W. Theobald, V. Versteeg, B. Yaakobi, and J. D. Zuegel, Physics of Plasmas **20**, 056317 (2013).

[10] V. N. Goncharov, T. C. Sangster, R. Betti, T. R. Boehly, M. J. Bonino, T. J. B. Collins, R. S. Craxton, J. A. Delettrez, D. H. Edgell, R. Epstein, R. K. Follett, C. J. Forrest, D. H. Froula, V. Yu. Glebov, D. R. Harding, R. J. Henchen, S. X. Hu, I. V. Igumenshchev, R. Janezic, J. H. Kelly, T. J. Kessler, T. Z. Kosc, S. J. Loucks, J. A. Marozas, F. J. Marshall, A. V. Maximov, R. L. McCrory, P. W. McKenty, D. D. Meyerhofer, D. T. Michel, J. F. Myatt, R. Nora, P. B. Radha, S. P. Regan, W. Seka, W. T. Shmayda, R. W. Short, A. Shvydky, S. Skupsky, C. Stoeckl, B. Yaakobi, J. A. Frenje, M. Gatu-Johnson, R. D. Petrasso, and D. T. Casey, Physics of Plasmas **21**, 056315 (2014).

[11] R. Nora, R. Betti, K. S. Anderson, A. Shvydky, A. Bose, K. M. Woo, A. R. Christopherson, J. A. Marozas, T. J. B. Collins, P. B. Radha, S. X. Hu, R. Epstein, F. J. Marshall, R. L. McCrory, T. C. Sangster, and D. D. Meyerhofer, Physics of Plasmas **21** (2014).

[12] S. X. Hu, G. Fiksel, V. N. Goncharov, S. Skupsky, D. D. Meyerhofer, and V. A. Smalyuk, Physical Review Letters **108**, 4 (2012).

[13] D. H. Froula, I. V. Igumenshchev, D. T. Michel, D. H. Edgell, R. Follett, V. Y. Glebov, V. N. Goncharov, J. Kwiatkowski, F. J. Marshall, P. B. Radha, W. Seka, C. Sorce, S. Stagnitto, C. Stoeckl, and T. C. Sangster, Physical Review Letters **108**, 1 (2012).

[14] J. F. Myatt, J. Zhang, R. W. Short, A. V. Maximov, W. Seka, D. H. Froula, D. H. Edgell, D. T. Michel, I. V. Igumenshchev, D. E. Hinkel, P. Michel, and J. D. Moody, Physics of Plasmas **21**, 055501 (2014).

[15] A. Bose, K. M. Woo, R. Nora, and R. Betti, Physics of Plasmas **22**, 072702 (2015).

[16] E. S. Dodd, J. F. Benage, G. A. Kyrala, D. C. Wilson, F. J. Wysocki, W. Seka, V. Y. Glebov, C. Stoeckl, and J. A. Frenje, Physics of Plasmas **19**, 042703 (2012).

[17] D. T. Michel, A. K. Davis, V. N. Goncharov, T. C. Sangster, S. X. Hu, I. V. Igumenshchev, D. D. Meyerhofer, W. Seka, and D. H. Froula, Physical Review Letters **114**, 155002 (2015).

[18] L. J. Suter, R. L. Kauffman, C. B. Darrow, A. A. Hauer, H. Kornblum, O. L. Landen, T. J. Orzechowski, D. W. Phillion, J. L. Porter, L. V. Powers, A. Richard, M. D. Rosen, A. R. Thiessen, and R. Wallace, Physics of Plasmas **3**, 2057 (1996).

[19] N. D. Delamater, T. J. Murphy, A. A. Hauer, R. L. Kauffman, A. L. Richard, E. L. Lindman, G. R. Magelssen, B. H. Wilde, L. V. Powers, S. M. Pollaine, L. J. Suter,

R. Chrien, D. B. Harris, M. B. Nelson, M. D. Cable, J. B. Moore, K. Gifford, and R. J. Wallace, Symmetry experiments in gas filled Hohlraums at Nova, in *AIP Conference Proceedings* Vol. 369, pp. 95–100, AIP, 1996.

[20] K. Schultz, J. Kaae, W. Miller, D. Steinman, and R. Stephens, Fusion Engineering and Design **44**, 441 (1999).

[21] J. D. Lindl, P. Amendt, R. L. Berger, S. G. Glendinning, S. H. Glenzer, S. W. Haan, R. L. Kauffman, O. L. Landen, and L. J. Suter, Physics of Plasmas **11**, 339 (2004).

[22] J. Lindl, O. Landen, J. Edwards, and E. Moses, Physics of Plasmas **21**, 020501 (2014).

[23] J. Lindl, Physics of Plasmas **2**, 3933 (1995).

[24] A. A. Hauer, L. Suter, N. Delamater, D. Ress, L. Powers, G. Magelssen, D. Harris, O. Landen, E. Lindmann, W. Hsing, D. Wilson, P. Amendt, R. Thiessen, R. Kopp, D. Phillion, B. Hammel, D. Baker, J. Wallace, R. Turner, M. Cray, R. Watt, J. Kilkenny, and J. Mack, Physics of Plasmas **2**, 2488 (1995).

[25] R. P. Drake, *High-Energy-Density Physics*Shock Wave and High Pressure Phenomena (Springer Berlin Heidelberg, 2006).

[26] S. H. Glenzer, B. J. MacGowan, N. B. Meezan, P. A. Adams, J. B. Alfonso, E. T. Alger, Z. Alherz, L. F. Alvarez, S. S. Alvarez, P. V. Amick, K. S. Andersson, S. D. Andrews, G. J. Antonini, P. A. Arnold, D. P. Atkinson, L. Auyang, S. G. Azevedo, B. N. M. Balaoing, J. A. Baltz, F. Barbosa, G. W. Bardsley, D. A. Barker, A. I. Barnes, A. Baron, R. G. Beeler, B. V. Beeman, L. R. Belk, J. C. Bell, P. M. Bell, R. L. Berger, M. A. Bergonia, L. J. Bernardez, L. V. Berzins, R. C. Bettenhausen, L. Bezerides, S. D. Bhandarkar, C. L. Bishop, E. J. Bond, D. R. Bopp, J. A. Borgman, J. R. Bower, G. A. Bowers, M. W. Bowers, D. T. Boyle, D. K. Bradley, J. L. Bragg, J. Braucht, D. L. Brinkerhoff, D. F. Browning, G. K. Brunton, S. C. Burkhart, S. R. Burns, K. E. Burns, B. Burr, L. M. Burrows, R. K. Butlin, N. J. Cahayag, D. A. Callahan, P. S. Cardinale, R. W. Carey, J. W. Carlson, A. D. Casey, C. Castro, J. R. Celeste, A. Y. Chakicherla, F. W. Chambers, C. Chan, H. Chandrasekaran, C. Chang, R. F. Chapman, K. Charron, Y. Chen, M. J. Christensen, A. J. Churby, T. J. Clancy, B. D. Cline, L. C. Clowdus, D. G. Cocherell, F. E. Coffield, S. J. Cohen, R. L. Costa, J. R. Cox, G. M. Curnow, M. J. Dailey, P. M. Danforth, R. Darbee, P. S. Datte, J. A. Davis, G. A. Deis, R. D. Demaret, E. L. Dewald, P. Di Nicola, J. M. Di Nicola, L. Divol, S. Dixit, D. B. Dobson, T. Doppner, J. D. Driscoll, J. Dugorepec, J. J. Duncan, P. C. Dupuy, E. G. Dzenitis, M. J. Eckart, S. L. Edson, G. J. Edwards, M. J. Edwards, O. D. Edwards, P. W. Edwards, J. C. Ellefson, C. H. Ellerbee, G. V. Erbert, C. M. Estes, W. J. Fabyan, R. N. Fallejo, M. Fedorov, B. Felker, J. T. Fink, M. D. Finney, L. F. Finnie, M. J. Fischer, J. M. Fisher, B. T. Fishler, J. W. Florio, A. Forsman, C. B. Foxworthy, R. M. Franks, T. Frazier, G. Frieder, T. Fung, G. N. Gawinski, C. R. Gibson, E. Giraldez, S. M. Glenn, B. P. Golick, H. Gonzales, S. A. Gonzales, M. J. Gonzalez, K. L. Griffin, J. Grippen, S. M. Gross, P. H. Gschweng,

G. Gururangan, K. Gu, S. W. Haan, S. R. Hahn, B. J. Haid, J. E. Hamblen, B. A. Hammel, A. V. Hamza, D. L. Hardy, D. R. Hart, R. G. Hartley, C. A. Haynam, G. M. Heestand, M. R. Hermann, G. L. Hermes, D. S. Hey, R. L. Hibbard, D. G. Hicks, D. E. Hinkel, D. L. Hipple, J. D. Hitchcock, D. L. Hodtwalker, J. P. Holder, J. D. Hollis, G. M. Holtmeier, S. R. Huber, A. W. Huey, D. N. Hulsey, S. L. Hunter, T. R. Huppler, M. S. Hutton, N. Izumi, J. L. Jackson, M. A. Jackson, K. S. Jancaitis, D. R. Jedlovec, B. Johnson, M. C. Johnson, T. Johnson, M. P. Johnston, O. S. Jones, D. H. Kalantar, J. H. Kamperschroer, R. L. Kauffman, G. A. Keating, L. M. Kegelmeyer, S. L. Kenitzer, J. R. Kimbrough, K. King, R. K. Kirkwood, J. L. Klingmann, K. M. Knittel, T. R. Kohut, K. G. Koka, S. W. Kramer, J. E. Krammen, K. G. Krauter, G. W. Krauter, E. K. Krieger, J. J. Kroll, K. N. La Fortune, L. J. Lagin, V. K. Lakamsani, O. L. Landen, S. W. Lane, A. B. Langdon, S. H. Langer, N. Lao, D. W. Larson, D. Latray, G. T. Lau, S. Le Pape, B. L. Lechleiter, Y. Lee, T. L. Lee, J. Li, J. A. Liebman, J. D. Lindl, S. F. Locke, H. K. Loey, R. A. London, F. J. Lopez, D. M. Lord, R. R. Lowe-Webb, J. G. Lown, A. P. Ludwigsen, N. W. Lum, R. R. Lyons, T. Ma, A. J. MacKinnon, M. D. Magat, D. T. Maloy, T. N. Malsbury, G. Markham, R. M. Marquez, A. A. Marsh, C. D. Marshall, S. R. Marshall, I. L. Maslennikov, D. G. Mathisen, G. J. Mauger, M. Y. Mauvais, J. A. McBride, T. McCarville, J. B. McCloud, A. McGrew, B. McHale, A. G. MacPhee, J. F. Meeker, J. S. Merill, E. P. Mertens, P. A. Michel, M. G. Miller, T. Mills, J. L. Milovich, R. Miramontes, R. C. Montesanti, M. M. Montoya, J. Moody, J. D. Moody, K. A. Moreno, J. Morris, K. M. Morriston, J. R. Nelson, M. Neto, J. D. Neumann, E. Ng, Q. M. Ngo, B. L. Olejniczak, R. E. Olson, N. L. Orsi, M. W. Owens, E. H. Padilla, T. M. Pannell, T. G. Parham, R. W. Patterson, G. Pavel, R. R. Prasad, D. Pendlton, F. A. Penko, B. L. Pepmeier, D. E. Petersen, T. W. Phillips, D. Pigg, K. W. Piston, K. D. Pletcher, C. L. Powell, H. B. Radousky, B. S. Raimondi, J. E. Ralph, R. L. Rampke, R. K. Reed, W. A. Reid, V. V. Rekow, J. L. Reynolds, J. J. Rhodes, M. J. Richardson, R. J. Rinnert, B. P. Riordan, A. S. Rivenes, A. T. Rivera, C. J. Roberts, J. A. Robinson, R. B. Robinson, S. R. Robison, O. R. Rodriguez, S. P. Rogers, M. D. Rosen, G. F. Ross, M. Runkel, A. S. Runtal, R. A. Sacks, S. F. Sailors, J. T. Salmon, J. D. Salmonson, R. L. Saunders, J. R. Schaffer, T. M. Schindler, M. J. Schmitt, M. B. Schneider, K. S. Segraves, M. J. Shaw, M. E. Sheldrick, R. T. Shelton, M. K. Shiflett, S. J. Shiromizu, M. Shor, L. L. Silva, S. A. Silva, K. M. Skulina, D. A. Smauley, B. E. Smith, L. K. Smith, A. L. Solomon, S. Sommer, J. G. Soto, N. I. Spafford, D. E. Speck, P. T. Springer, M. Stadermann, F. Stanley, T. G. Stone, E. A. Stout, P. L. Stratton, R. J. Strausser, L. J. Suter, W. Sweet, M. F. Swisher, J. D. Tappero, J. B. Tassano, J. S. Taylor, E. A. Tekle, C. Thai, C. A. Thomas, A. Thomas, A. L. Throop, G. L. Tietbohl, J. M. Tillman, R. P. J. Town, S. L. Townsend, K. L. Tribbey, D. Trummer, J. Truong, J. Vaher, M. Valadez, P. Van Arsdall, A. J. Van Prooyen, E. O. Vergel de Dios, M. D. Vergino, S. P. Vernon, J. L. Vickers, G. T. Villanueva, M. A. Vitalich, S. A. Vonhof, F. E. Wade, R. J. Wallace, C. T. Warren, A. L. Warrick, J. Watkins, S. Weaver, P. J. Wegner, M. A. Weingart, J. Wen, K. S. White, P. K. Whitman, K. Widmann, C. C. Widmayer, K. Wilhelmsen, E. A. Williams, W. H. Williams, L. Willis, E. F. Wilson, B. A. Wilson, M. C. Witte, K. Work, P. S. Yang, B. K. Young, K. P. Youngblood, R. A. Zacharias, T. Zaleski, P. G. Zapata, H. Zhang,

J. S. Zielinski, J. L. Kline, G. A. Kyrala, C. Niemann, J. D. Kilkenny, A. Nikroo, B. M. Van Wonterghem, L. J. Atherton, and E. I. Moses, Physical Review Letters **106**, 085004 (2011).

[27] M. B. Schneider, S. A. MacLaren, K. Widmann, N. B. Meezan, J. H. Hammer, B. E. Yoxall, P. M. Bell, L. R. Benedetti, D. K. Bradley, D. A. Callahan, E. L. Dewald, T. Döppner, D. C. Eder, M. J. Edwards, T. M. Guymer, D. E. Hinkel, M. Hohenberger, W. W. Hsing, M. L. Kervin, J. D. Kilkenny, O. L. Landen, J. D. Lindl, M. J. May, P. Michel, J. L. Milovich, J. D. Moody, A. S. Moore, J. E. Ralph, S. P. Regan, C. A. Thomas, and A. S. Wan, Physics of Plasmas **22**, 122705 (2015).

[28] A. R. Bell, R. G. Evans, and D. J. Nicholas, Physical Review Letters **46**, 243 (1981).

[29] J. P. Matte, T. W. Johnston, J. Delettrez, and R. L. McCrory, Physical Review Letters **53**, 1461 (1984).

[30] D. Montgomery, O. Landen, R. Drake, K. Estabrook, H. Baldis, S. Batha, K. Bradley, and R. Procassini, Physical Review Letters **73**, 2055 (1994).

[31] S. H. Glenzer, C. A. Back, L. J. Suter, M. A. Blain, O. L. Landen, J. D. Lindl, B. J. MacGowan, G. F. Stone, R. E. Turner, and B. H. Wilde, Physical Review Letters **79**, 1277 (1997).

[32] D. R. Gray, J. D. Kilkenny, M. S. White, P. Blyth, and D. Hull, Physical Review Letters **39**, 1270 (1977).

[33] J. Hawreliak, D. M. Chambers, S. H. Glenzer, A. Gouveia, R. J. Kingham, R. S. Marjoribanks, P. a. Pinto, O. Renner, P. Soundhauss, S. Topping, E. Wolfrum, P. E. Young, and J. S. Wark, Journal of Physics B: Atomic, Molecular and Optical Physics **37**, 1541 (2004).

[34] D. H. Froula, J. S. Ross, L. Divol, N. Meezan, A. J. MacKinnon, R. Wallace, and S. H. Glenzer, Physics of Plasmas **13**, 052704 (2006).

[35] G. P. Schurtz, P. D. Nicolai, and M. Busquet, Physics of Plasmas **7**, 4238 (2000).

[36] P. D. Nicolai, J.-L. A. Feugeas, and G. P. Schurtz, Physics of Plasmas **13**, 032701 (2006).

[37] G. Schurtz, S. Gary, S. Hulin, C. Chenais-Popovics, J.-C. Gauthier, F. Thais, J. Breil, F. Durut, J.-L. Feugeas, P.-H. Maire, P. Nicolaï, O. Peyrusse, C. Reverdin, G. Soullié, V. Tikhonchuk, B. Villette, and C. Fourment, Physical Review Letters **98**, 095002 (2007).

[38] M. Rosen, H. Scott, D. Hinkel, E. Williams, D. Callahan, R. Town, L. Divol, P. Michel, W. Kruer, L. Suter, R. London, J. Harte, and G. Zimmerman, High Energy Density Physics **7**, 180 (2011).

[39] J. L. Kline, S. H. Glenzer, R. E. Olson, L. J. Suter, K. Widmann, D. A. Callahan, S. N. Dixit, C. A. Thomas, D. E. Hinkel, E. A. Williams, A. S. Moore, J. Celeste, E. Dewald, W. W. Hsing, A. Warrick, J. Atherton, S. Azevedo, R. Beeler, R. Berger, A. Conder, L. Divol, C. A. Haynam, D. H. Kalantar, R. Kauffman, G. A. Kyrala, J. Kilkenny, J. Liebman, S. Le Pape, D. Larson, N. B. Meezan, P. Michel, J. Moody, M. D. Rosen, M. B. Schneider, B. Van Wonterghem, R. J. Wallace, B. K. Young, O. L. Landen, and B. J. MacGowan, Physical Review Letters **106**, 085003 (2011).

[40] R. E. Olson, L. J. Suter, J. L. Kline, D. A. Callahan, M. D. Rosen, S. N. Dixit, O. L. Landen, N. B. Meezan, J. D. Moody, C. A. Thomas, A. Warrick, K. Widmann, E. A. Williams, and S. H. Glenzer, Physics of Plasmas **19**, 053301 (2012).

[41] S. H. Glenzer, W. E. Alley, K. G. Estabrook, J. S. De Groot, M. G. Haines, J. H. Hammer, J.-P. Jadaud, B. J. MacGowan, J. D. Moody, W. Rozmus, L. J. Suter, T. L. Weiland, and E. a. Williams, Physics of Plasmas **6**, 2117 (1999).

[42] S. H. Glenzer, K. B. Fournier, B. G. Wilson, R. W. Lee, and L. J. Suter, Physical Review Letters **87**, 045002 (2001).

[43] J. Stamper, K. Papadopoulos, R. Sudan, S. Dean, E. McLean, and J. Dawson, Physical Review Letters **26**, 1012 (1971).

[44] S. I. Braginskii, Reviews of Plasma Physics **1**, 205 (1965).

[45] D. H. Froula, J. S. Ross, B. B. Pollock, P. Davis, A. N. James, L. Divol, M. J. Edwards, A. A. Offenberger, D. Price, R. P. J. Town, G. R. Tynan, and S. H. Glenzer, Physical Review Letters **98**, 1 (2007).

[46] L. A. Gizzi, A. Mackinnon, D. Riley, S. Viana, and O. Willi, Laser and Particle Beams **13**, 511 (1995).

[47] C. K. Li, F. H. Séguin, J. A. Frenje, J. R. Rygg, R. D. Petrasso, R. P. J. Town, P. A. Amendt, S. P. Hatchett, O. L. Landen, A. J. Mackinnon, P. K. Patel, M. Tabak, J. P. Knauer, T. C. Sangster, and V. A. Smalyuk, Physical Review Letters **99**, 015001 (2007).

[48] C. K. Li, F. Séguin, J. Frenje, N. Sinenian, M. Rosenberg, M.-E. Manuel, H. Rinderknecht, A. Zylstra, R. Petrasso, P. Amendt, O. Landen, A. Mackinnon, R. Town, S. Wilks, R. Betti, D. Meyerhofer, J. Soures, J. Hund, J. Kilkenny, and A. Nikroo, Nuclear Fusion **53**, 073022 (2013).

[49] C. K. Li, F. H. Seguin, J. R. Rygg, J. A. Frenje, M. Manuel, R. D. Petrasso, R. Betti, J. Delettrez, J. P. Knauer, F. Marshall, D. D. Meyerhofer, D. Shvarts, V. A. Smalyuk, C. Stoeckl, O. L. Landen, R. P. J. Town, C. A. Back, and J. D. Kilkenny, Physical Review Letters **100**, 225001 (2008).

[50] C. K. Li, F. H. Séguin, J. A. Frenje, R. D. Petrasso, P. A. Amendt, R. P. J. Town, O. L. Landen, J. R. Rygg, R. Betti, J. P. Knauer, D. D. Meyerhofer, J. M. Soures, C. A. Back, J. D. Kilkenny, and A. Nikroo, Physical Review Letters **102**, 1 (2009).

[51] C. K. Li, a. B. Zylstra, J. a. Frenje, F. H. Séguin, N. Sinenian, R. D. Petrasso, P. a. Amendt, R. Bionta, S. Friedrich, G. W. Collins, E. Dewald, T. Döppner, S. H. Glenzer, D. G. Hicks, O. L. Landen, J. D. Kilkenny, a. J. Mackinnon, N. Meezan, J. Ralph, J. R. Rygg, J. Kline, and G. Kyrala, New Journal of Physics **15**, 025040 (2013).

[52] P. M. Nilson, L. Willingale, M. C. Kaluza, C. Kamperidis, S. Minardi, M. S. Wei, P. Fernandes, M. Notley, S. Bandyopadhyay, M. Sherlock, R. J. Kingham, M. Tatarakis, Z. Najmudin, W. Rozmus, R. G. Evans, M. G. Haines, A. E. Dangor, and K. Krushelnick, Physical Review Letters **97**, 255001 (2006).

[53] L. Willingale, P. M. Nilson, M. C. Kaluza, A. E. Dangor, R. G. Evans, P. Fernandes, M. G. Haines, C. Kamperidis, R. J. Kingham, C. P. Ridgers, M. Sherlock, A. G. R. Thomas, M. S. Wei, Z. Najmudin, K. Krushelnick, S. Bandyopadhyay, M. Notley, S. Minardi, M. Tatarakis, and W. Rozmus, Physics of Plasmas **17**, 043104 (2010).

[54] M. Rosenberg, C. Li, W. Fox, A. Zylstra, C. Stoeckl, F. Séguin, J. Frenje, and R. Petrasso, Physical Review Letters **114**, 1 (2015).

[55] M. Yamada, R. Kulsrud, and H. Ji, Reviews of Modern Physics **82**, 603 (2010).

[56] W. Fox, A. Bhattacharjee, and K. Germaschewski, Physical Review Letters **106**, 215003 (2011).

[57] W. Fox, A. Bhattacharjee, and K. Germaschewski, Physics of Plasmas **19**, 056309 (2012).

[58] S. Atzeni, Laser and Particle Beams **8**, 227 (1990).

[59] G. Bekefi, *Radiation processes in plasmas*Wiley series in plasma physics (Wiley, 1966).

[60] S. Glasstone and R. H. Lovberg, *Controlled thermonuclear reactions: an introduction to theory and experiment* (van Nostrand, 1960).

[61] W. L. Kruer, Physics of Fluids B: Plasma Physics **3**, 2356 (1991).

[62] B. MacGowan, B. Afeyan, C. Back, R. Berger, G. Bonnaud, M. Casanova, B. Cohen, D. Desenne, D. DuBois, A. Dulieu, and Others, Physics of Plasmas **3**, 2029 (1996).

[63] W. L. Kruer, Physics of Plasmas **7**, 2270 (2000).

[64] I. P. Shkarofsky*The Particle Kinetics of Plasmas* Vol. 35 (Addison-Wesley Pub. Co., 1967).

[65] C. P. Ridgers, A. G. R. Thomas, R. J. Kingham, and A. P. L. Robinson, Physics of Plasmas **15**, 092311 (2008).

[66] F. F. Chen, *Introduction to Plasma Physics and Controlled Fusion* (Springer US, Boston, MA, 1984).

[67] A. G. R. Thomas, M. Tzoufras, A. Robinson, R. Kingham, C. Ridgers, M. Sherlock, and A. Bell, Journal of Computational Physics **231**, 1051 (2012).

[68] M. S. Murillo, Physics of Plasmas **11**, 2964 (2004).

[69] M. N. Rosenbluth, W. M. MacDonald, and D. L. Judd, Physical Review **107**, 1 (1957).

[70] E. M. Epperlein and M. G. Haines, Physics of Fluids **29**, 1029 (1986).

[71] T. W. Johnston, Physical Review **120**, 1103 (1960).

[72] I. P. Shkarofsky, Canadian Journal of Physics **41**, 1753 (1963).

[73] L. Spitzer and R. Härm, Physical Review **89**, 977 (1953).

[74] A. B. Langdon, Physical Review Letters **44**, 575 (1980).

[75] J. M. Liu, J. S. De Groot, J. P. Matte, T. W. Johnston, and R. P. Drake, Physical Review Letters **72**, 2717 (1994).

[76] J. M. Liu, J. S. De Groot, J. P. Matte, T. W. Johnston, and R. P. Drake, Physics of Plasmas **1**, 3570 (1994).

[77] W. Y. Huo and Q. Zeng, Physics of Plasmas **22**, 094503 (2015).

[78] J. J. Bissell, C. P. Ridgers, and R. J. Kingham, New Journal of Physics **15**, 025017 (2013).

[79] W. Yi Huo, K. Lan, P. Jun Gu, H. Yong, and Q. Hong Zeng, Physics of Plasmas **19**, 012313 (2012).

[80] P. Mora and H. Yahi, Physical Review A **26**, 2259 (1982).

[81] J. R. Albritton, Physical Review Letters **50**, 2078 (1983).

[82] J. R. Albritton, E. A. Williams, I. B. Bernstein, and K. P. Swartz, Physical Review Letters **57**, 1887 (1986).

[83] D. Shvarts, J. Delettrez, R. McCrory, and C. Verdon, Physical Review Letters **47**, 247 (1981).

[84] P. Mora and J. Luciani, Laser and Particle Beams **12**, 387 (1994).

[85] W. Manheimer, D. Colombant, and A. J. Schmitt, Physics of Plasmas **19**, 056317 (2012).

[86] J. Luciani, P. Mora, and J. Virmont, Physical Review Letters **5**, 2 (1983).

[87] L. Lancia, B. Albertazzi, C. Boniface, A. Grisollet, R. Riquier, F. Chaland, K.-C. Le Thanh, P. Mellor, P. Antici, S. Buffechoux, S. N. Chen, D. Doria, M. Nakatsutsumi, C. Peth, M. Swantusch, M. Stardubtsev, L. Palumbo, M. Borghesi, O. Willi, H. Pépin, and J. Fuchs, Physical Review Letters **113**, 235001 (2014).

[88] A. Schlüter and L. Biermann, Zeitschrift für Naturforschung A **5**, 237 (1950).

[89] J. Meinecke, H. W. Doyle, F. Miniati, A. R. Bell, R. Bingham, R. Crowston, R. P. Drake, M. Fatenejad, M. Koenig, Y. Kuramitsu, C. C. Kuranz, D. Q. Lamb, D. Lee, M. J. MacDonald, C. D. Murphy, H.-S. Park, A. Pelka, A. Ravasio, Y. Sakawa, A. A. Schekochihin, A. Scopatz, P. Tzeferacos, W. C. Wan, N. C. Woolsey, R. Yurchak, B. Reville, and G. Gregori, Nature Physics **10**, 520 (2014).

[90] R. J. Kingham and A. R. Bell, Physical Review Letters **88**, 045004 (2002).

[91] E. G. Zweibel and M. Yamada, Annual Review of Astronomy and Astrophysics **47**, 291 (2009).

[92] A. G. R. Thomas, R. J. Kingham, and C. P. Ridgers, New Journal of Physics **11**, 033001 (2009).

[93] J. Birn, J. F. Drake, M. A. Shay, B. N. Rogers, R. E. Denton, M. Hesse, M. Kuznetsova, Z. W. Ma, A. Bhattacharjee, A. Otto, and P. L. Pritchett, Journal of Geophysical Research **106**, 3715 (2001).

[94] M. M. Kuznetsova, M. Hesse, and D. Winske, Journal of Geophysical Research **105**, 7601 (2000).

[95] P. L. Pritchett, Journal of Geophysical Research **106**, 3783 (2001).

[96] M. M. Kuznetsova, M. Hesse, and D. Winske, Journal of Geophysical Research **106**, 3799 (2001).

[97] M. G. Haines, Plasma Physics and Controlled Fusion **28**, 1705 (2000).

[98] A. Nishiguchi, T. Yabe, M. G. Haines, M. Psimopoulos, and H. Takewaki, Physical Review Letters **53**, 262 (1984).

[99] A. Nishiguchi, T. Yabe, and M. G. Haines, Physics of Fluids **28**, 3683 (1985).

[100] T. H. Kho and M. G. Haines, Physical Review Letters **55**, 825 (1985).

[101] C. P. Ridgers, R. J. Kingham, and A. G. R. Thomas, Physical Review Letters **100**, 075003 (2008).

[102] L. Willingale, A. G. R. Thomas, P. M. Nilson, M. C. Kaluza, S. Bandyopadhyay, A. E. Dangor, R. G. Evans, P. Fernandes, M. G. Haines, C. Kamperidis, R. J. Kingham, S. Minardi, M. Notley, C. P. Ridgers, W. Rozmus, M. Sherlock, M. Tatarakis, M. S. Wei, Z. Najmudin, and K. Krushelnick, Physical Review Letters **105**, 1 (2010).

[103] I. V. Igumenshchev, A. B. Zylstra, C. K. Li, P. M. Nilson, V. N. Goncharov, and R. D. Petrasso, Physics of Plasmas **21**, 062707 (2014).

[104] A. L. Velikovich, J. L. Giuliani, and S. T. Zalesak, Physics of Plasmas **22**, 042702 (2015).

[105] J. U. Brackbill and S. R. Goldman, Communications on Pure and Applied Mathematics **36**, 415 (1983).

[106] A. S. Joglekar, A. G. R. Thomas, W. Fox, and A. Bhattacharjee, Physical Review Letters **112**, 105004 (2014).

[107] S. Balay, W. D. Gropp, L. C. McInnes, and B. F. Smith, Efficient Management of Parallelism in Object Oriented Numerical Software Libraries, in *Modern Software Tools in Scientific Computing*, edited by E. Arge, A. M. Bruaset, and H. P. Langtangen, pp. 163–202, Birkh{ä}user Press, 1997.

[108] S. Balay, S. Abhyankar, M. Adams, J. Brown, P. Brune, K. Buschelman, L. Dalcin, V. Eijkhout, W. Gropp, D. Kaushik, M. Knepley, L. C. McInnes, K. Rupp, B. Smith, S. Zampini, and H. Zhang, PETSc Web page, 2015.

[109] S. Balay, S. Abhyankar, M. Adams, J. Brown, P. Brune, K. Buschelman, L. Dalcin, V. Eijkhout, W. Gropp, D. Kaushik, M. Knepley, L. C. McInnes, K. Rupp, B. Smith, S. Zampini, and H. Zhang, Argonne National Laboratory Report No. ANL-95/11 - Revision 3.6, 2015 (unpublished).

[110] R. J. Kingham and A. R. Bell, Journal of Computational Physics **194**, 1 (2004).

[111] E. M. Epperlein and R. W. Short, Physics of Fluids B: Plasma Physics **4**, 2211 (1992).

[112] C. P. Ridgers, *Magnetic Fields and Non-Local Transport in Laser Plasmas*, PhD thesis, Imperial College, 2008.

[113] L. Benkevitch, I. Sokolov, D. Oberoi, and T. Zurbuchen, Arxiv: Astro-ph , 14 (2010), arXiv:1006.5635.

[114] M. J. Edwards, P. K. Patel, J. D. Lindl, L. J. Atherton, S. H. Glenzer, S. W. Haan, J. D. Kilkenny, O. L. Landen, E. I. Moses, A. Nikroo, R. Petrasso, T. C. Sangster, P. T. Springer, S. Batha, R. Benedetti, L. Bernstein, R. Betti, D. L. Bleuel, T. R. Boehly, D. K. Bradley, J. A. Caggiano, D. A. Callahan, P. M. Celliers, C. J. Cerjan, K. C. Chen, D. S. Clark, G. W. Collins, E. L. Dewald, L. Divol, S. Dixit, T. Doeppner, D. H. Edgell, J. E. Fair, M. Farrell, R. J. Fortner, J. Frenje, M. G. Gatu Johnson, E. Giraldez, V. Y. Glebov, G. Grim, B. A. Hammel, A. V. Hamza, D. R. Harding, S. P. Hatchett, N. Hein, H. W. Herrmann, D. Hicks, D. E. Hinkel, M. Hoppe, W. W. Hsing, N. Izumi, B. Jacoby, O. S. Jones, D. Kalantar, R. Kauffman, J. L. Kline, J. P. Knauer, J. A. Koch, B. J. Kozioziemski, G. Kyrala, K. N. LaFortune, S. L. Pape, R. J. Leeper, R. Lerche, T. Ma, B. J. MacGowan, A. J. MacKinnon, A. Macphee, E. R.

Mapoles, M. M. Marinak, M. Mauldin, P. W. McKenty, M. Meezan, P. A. Michel, J. Milovich, J. D. Moody, M. Moran, D. H. Munro, C. L. Olson, K. Opachich, A. E. Pak, T. Parham, H.-S. Park, J. E. Ralph, S. P. Regan, B. Remington, H. Rinderknecht, H. F. Robey, M. Rosen, S. Ross, J. D. Salmonson, J. Sater, D. H. Schneider, F. H. Séguin, S. M. Sepke, D. A. Shaughnessy, V. A. Smalyuk, B. K. Spears, C. Stoeckl, W. Stoeffl, L. Suter, C. A. Thomas, R. Tommasini, R. P. Town, S. V. Weber, P. J. Wegner, K. Widman, M. Wilke, D. C. Wilson, C. B. Yeamans, and A. Zylstra, Physics of Plasmas **20**, 070501 (2013).

[115] L. Willingale, A. G. R. Thomas, P. M. Nilson, M. C. Kaluza, S. Bandyopadhyay, A. E. Dangor, R. G. Evans, P. Fernandes, M. G. Haines, C. Kamperidis, R. J. Kingham, S. Minardi, M. Notley, C. P. Ridgers, W. Rozmus, M. Sherlock, M. Tatarakis, M. S. Wei, Z. Najmudin, and K. Krushelnick, Plasma Physics and Controlled Fusion **53**, 124026 (2011).

[116] E. Fourkal, V. Y. Bychenkov, W. Rozmus, R. Sydora, C. Kirkby, C. E. Capjack, S. H. Glenzer, and H. A. Baldis, Physics of Plasmas **8**, 550 (2001).

[117] P. Y. Chang, G. Fiksel, M. Hohenberger, J. P. Knauer, R. Betti, F. J. Marshall, D. D. Meyerhofer, F. H. Séguin, and R. D. Petrasso, Physical Review Letters **107**, 035006 (2011).

[118] M. Hohenberger, P. Y. Chang, G. Fiksel, J. P. Knauer, R. Betti, F. J. Marshall, D. D. Meyerhofer, F. H. Séguin, and R. D. Petrasso, Physics of Plasmas **19**, 056306 (2012).

[119] D. S. Montgomery, B. J. Albright, D. H. Barnak, P. Y. Chang, J. R. Davies, G. Fiksel, D. H. Froula, J. L. Kline, M. J. Macdonald, A. B. Sefkow, L. Yin, and R. Betti, Physics of Plasmas **22**, 010703 (2015).

[120] J. F. Drake, P. K. Kaw, Y. C. Lee, G. Schmid, C. S. Liu, and M. N. Rosenbluth, Physics of Fluids **17**, 778 (1974).

[121] S. P. Regan, N. B. Meezan, L. J. Suter, D. J. Strozzi, W. L. Kruer, D. Meeker, S. H. Glenzer, W. Seka, C. Stoeckl, V. Y. Glebov, T. C. Sangster, D. D. Meyerhofer, R. L. McCrory, E. A. Williams, O. S. Jones, D. A. Callahan, M. D. Rosen, O. L. Landen, C. Sorce, and B. J. MacGowan, Physics of Plasmas **17**, 020703 (2010).

[122] D. J. Strozzi, L. J. Perkins, M. M. Marinak, D. J. Larson, J. M. Koning, and B. G. Logan, Journal of Plasma Physics **81**, 475810603 (2015), arXiv:1508.00803.

[123] E. N. Parker, The Astrophysical Journal **174**, 499 (1972).

[124] R. M. Green and P. A. Sweet, The Astrophysical Journal **147**, 1153 (1967).

[125] H. Ji, M. Yamada, S. Hsu, and R. Kulsrud, Physical Review Letters **80**, 3256 (1998).

[126] H. Ji, Y. Ren, M. Yamada, S. Dorfman, W. Daughton, and S. P. Gerhardt, Geophysical Research Letters **35**, 1 (2008), arXiv:1001.0082.

[127] E. Priest and T. Forbes, *Magnetic Reconnection* (Cambridge University Press, Cambridge, 2000).

[128] J. A. Miller, P. J. Cargill, A. G. Emslie, G. D. Holman, B. R. Dennis, T. N. LaRosa, R. M. Winglee, S. G. Benka, and S. Tsuneta, Journal of Geophysical Research **102**, 14631 (1997).

[129] M. Øieroset, R. P. Lin, T. D. Phan, D. E. Larson, and S. D. Bale, Physical Review Letters **1**, 1 (2002).

[130] W. Daughton, V. Roytershteyn, B. J. Albright, H. Karimabadi, L. Yin, and K. J. Bowers, Physics of Plasmas **16**, 072117 (2009).

[131] S. H. Glenzer, W. Rozmus, B. J. MacGowan, K. G. Estabrook, J. D. de Groot, G. B. Zimmerman, H. a. Baldis, J. a. Harte, R. W. Lee, E. a. Williams, and B. G. Wilson, Physical Review Letters **82**, 97 (1999).

[132] L. J. Perkins, B. G. Logan, G. B. Zimmerman, and C. J. Werner, Physics of Plasmas **20**, 072708 (2013).

[133] M. Keskinen and A. Schmitt, Laser and Particle Beams **25**, 333 (2007).

[134] E. M. Epperlein, Physics of Plasmas **1**, 109 (1994).

[135] W. L. Kruer, *Laser-Plasma Interactions and Applications* (Springer International Publishing, Heidelberg, 2013).